BAW-1273
Ca-7

SPECTRAL SHIFT CONTROL REACTOR BASIC PHYSICS PROGRAM

Measurement and Analysis of Uniform Lattices of Slightly Enriched UO_2 Moderated by D_2O-H_2O Mixtures

November 1963

AEC Contract No. AT(30-1)-2602
B&W Contract No. 59-3082

THE BABCOCK & WILCOX COMPANY

NUCLEAR DEVELOPMENT CENTER

DISCLAIMER

Printed in U. S. A. PRICE $2.75 Available from the

OFFICE OF TECHNICAL SERVICES
U. S. DEPARTMENT OF COMMERCE
WASHINGTON 25, D. C.

BAW-1273, Ca-7
AEC R&D Report
TID-4500, 23rd Ed.
UC-80

SPECTRAL SHIFT CONTROL REACTOR BASIC PHYSICS PROGRAM

Measurement and Analysis of Uniform Lattices of Slightly Enriched UO_2 Moderated by D_2O-H_2O Mixtures

November 1963

By

T. C. Engelder, R. H. Clark, M. N. Baldwin,
E. J. DeRoche, G. T. Fairburn, and J. W. Hallam

Nuclear Development Center
Research & Development Division

and

D. H. Roy, N. Vutz, and T. M. Schuler

Engineering Department
Atomic Energy Division

Submitted to
THE UNITED STATES ATOMIC ENERGY COMMISSION
by
THE BABCOCK & WILCOX COMPANY
Lynchburg, Virginia

THIS PAGE
WAS INTENTIONALLY
LEFT BLANK

The Babcock & Wilcox Company
Nuclear Development Center
Report BAW-1273

ABSTRACT

This report summarizes the experimental results and theoretical interpretation of a series of twenty uniform lattice critical experiments in which the neutron spectrum is varied over a fairly broad range. Two types of fuel rods were studied: 4.02%-enriched UO_2 in stainless steel tubes and 2.46%-enriched UO_2 in aluminum tubes. Lattice nonmoderator-to-moderator volume ratios ranged from 0.65 to 1.2. The moderators were mixtures of light and heavy water ranging in composition from zero to 77% D_2O, with and without boric acid. Measurements include critical size and composition, $\partial\rho/\partial h$, buckling and reflector savings, thermal disadvantage factor, and cadmium ratios of U^{235} and U^{238}. Theoretical methods used to analyze the data are given, and results are compared.

THIS PAGE
WAS THIS PAGE ALLY
WAS INTENTIONALLY
LEFT BLANK

Summary of Experimental Data

Core no.	Fuel enrich., wt% U^{235}	M/W ratio	Moderator composition: D_2O, mole %	Moderator composition: Boron, gm B/ℓ	Number of fuel rods	Radial parameters, cm: Core radius	Radial parameters, cm: Reflector thickness	Radial parameters, cm: Reflector savings	Axial parameters, cm: Moderator height	Axial parameters, cm: Reflector thickness	Axial parameters, cm: Reflector savings	Buckling, $\times 10^{-4}$ cm^{-2}: Radial	Buckling, $\times 10^{-4}$ cm^{-2}: Axial	Buckling, $\times 10^{-4}$ cm^{-2}: Total	$(1/k^2)(\delta k/\delta B^2)$, $\times 10^5$ ¢-cm^2	$\bar{\phi}_m/\bar{\phi}_f$	δ_{25}	ρ_{28}
I	4.02	1.006	0.0	0	484	18.75	∞	7.4	154.0	15.6	11.6	84.4	3.60	88.0	4.19	1.25	0.253	4.12
II	4.02	1.006	0.0	3.39	4904	59.71	∞	6.2	146.7	22.9	13.1	13.3	3.87	17.2	- -	1.25	- -	- -
III	4.02	1.006	76.5	0	5284	61.98	14.22	25.7	152.9	16.7	21.6	7.53	3.24	10.77	7.98	1.17	0.855	15.4
III-22	4.02	1.006	73.8	0	5284	61.98	14.22	20.3	110.8	58.8	22.6	8.54	5.55	14.09	8.21	- -	- -	- -
IV	4.02	1.006	69.7	0	2252	40.46	35.74	21.4	151.0	18.6	17.6	15.13	3.47	18.60	7.90	1.16	0.699	11.5
V	4.02	1.006	69.7	0.422	5284	61.98	(14.22)	11.6	145.0	24.6	22.0	10.68	3.55	14.23	7.77	1.13	0.758	- -
VI	4.02	1.006	49.6	1.79	5284	61.98	14.22	6.7	147.6	22.0	19.7	12.25	3.53	15.78	6.04	1.19	0.535	- -
VII-B	4.02	1.006	81.2	0	- -	68.04	8.16	- -	141.3	28.3	19.5	- -	3.82	- -	- -	1.13	1.064	- -
IX	4.02	1.006	49.7	0	952	26.31	49.89	11.5	150.6	19.0	15.2	40.4	3.59	44.0	6.13	1.17	0.478	8.13
X	4.02	1.195	0.0	0	608	20.18	56.02	7.6	146.1	23.5	12.1	75.0	3.95	79.0	4.72	1.239	0.307	5.08
XI	4.02	1.195	70.1	0	5320	59.68	16.52	21.4	146.1	23.5	21.0	8.88	3.52	12.40	7.73	1.179	0.893	14.9
XII	4.02	1.195	49.7	0	1390	30.51	45.69	12.8	146.1	23.5	16.5	30.9	3.73	34.6	6.63	1.195	0.575	9.80
XIII	2.46	1.001	0.0	0	596	20.62	55.38	8.8	141.1	12.3	14.6	66.0	4.07	70.1	5.00	1.191	0.151	2.28
XIV	2.46	1.001	70.0	0	2852	45.47	30.73	20.7	134.9	18.5	16.9	13.18	4.29	17.47	9.02	1.147	0.392	5.95
XV	2.46	1.001	49.8	0	1140	28.79	47.41	11.9	134.5	18.9	14.0	34.9	4.48	39.4	7.01	1.156	0.264	4.00
XVI	2.46	0.651	85.5	0	5124	68.73	7.47	13.3	134.2	19.2	19.1	8.59	4.20	12.79	11.0	1.143	0.398	6.29
XVII	2.46	0.651	70.0	0	872	28.35	47.85	16.0	134.7	18.7	13.7	29.4	4.48	33.7	9.06	1.170	0.253	3.95
XVIII	2.46	1.001	72.1	0	5137	61.11	15.09	20.1	107.9	45.5	20.4	8.76	5.99	14.75	(10.1)	- -	- -	- -
XIX	2.46	1.001	50.0	0.778	5137	61.11	15.09	8.9	97.7	55.7	20.1	11.79	7.12	18.91	(7.7)	- -	- -	- -
XX	2.46	1.001	0.0	1.675	5137	61.11	15.09	7.2	93.2	60.2	19.2	12.4	7.82	20.2	(5.1)	- -	- -	- -

THIS PAGE
WAS INTENTIONALLY
LEFT BLANK

CONTENTS

CONTENTS (Cont'd)

List of Tables

List of Figures

1. INTRODUCTION

1.1. SSCR Basic Physics Program

In July 1960, the Babcock & Wilcox Company (under AEC contract) initiated a study of the basic physics underlying the Spectral Shift Control Reactor (SSCR) concept. In application, the reactor core is a rod lattice of slightly enriched uranium oxide, moderated and cooled by a variable mixture of light and heavy water. Initially, the moderator is rich in heavy water, so the neutron spectrum is epithermal, and a relatively large fraction of the excess neutrons are absorbed in the fertile material. As fuel is consumed, the moderator is diluted with light water, thereby shifting the spectrum toward thermal energy and providing the necessary increase in core reactivity.

The objective of the SSCR Basic Physics Program is to study the nuclear properties of rod lattices moderated by D_2O-H_2O mixtures in the range of application to the SSCR concept. Primary emphasis is given to the uranium cycle having U^{235} enrichments from 2.5 to 4%. Moderator compositions extend from 0% D_2O (light water) to about 90% D_2O, and nonmoderator-to-moderator volume ratios (M/W) cover the range of 0.7 to 1.2. The experimental program includes uniform and nonuniform lattice critical experiments, exponential experiments at room and elevated temperatures, and neutron age measurements. The theoretical program includes the development of analytical methods applicable to SSCR type lattices and the analysis and correlation of the experimental results.

This report summarizes the experimental results and the analysis of all slightly enriched UO_2 uniform lattice experiments. Critical experiments performed in the first phase of the program and reported earlier[1-3] are also included, since the experimental data have been reanalyzed (with minor changes noted here). The exponential and age measurements have already been reported[4-6], and the results and

analysis of the nonuniform critical experiments are being issued in a separate report[7]. Additional details on all phases of the program are available in the series of SSCR Basic Physics Program Quarterly Technical Reports[8-17].

1.2. Uniform Lattice Studies

During the past two and one-half years, twenty major critical assemblies and five exponential assemblies were studied. The assemblies differed in fuel enrichment, nonmoderator-to-moderator volume ratio, and moderator composition. Two fuel enrichments were used: 4.02%-enriched UO_2 swaged in 0.475-inch OD stainless steel tubes, and 2.46%-enriched UO_2 pellets in 0.475-inch OD aluminum tubes. Some data on thorium-cycle lattices were also obtained in one critical and three exponential experiments with 93%-enriched UO_2-ThO_2 (N_{Th}/N_{25} = 15) fuel. The results[3,4] and analysis[1] of the thorium cores have already been reported and will not be repeated here.

The lattice nonmoderator-to-moderator volume ratios (M/W) were selected to cover a fairly broad range and include the range of interest for practical SSCR designs. Experiments were performed at three M/W ratios: approximately 1.2, 1.0, and 0.65. The moderator compositions in the critical experiments varied from 0% D_2O (light water) to a maximum of about 85% D_2O in H_2O. The upper limit was set by the quantity of fuel available and the lattice reactivity. Since this limit was 76.5% for the 4.02%-enriched fuel at M/W = 1.0, the range was extended to about 90% by including several exponential experiments[4,5]. Boric acid was added to the moderator in several of the critical assemblies to permit some separation of k_∞ and leakage-dependent properties.

The following measurements were made in each critical assembly: critical size and composition, $\partial\rho/\partial h$, radial and axial bucklings and reflector savings, thermal disadvantage factor, cadmium ratio of U^{235}, and cadmium ratio of U^{238}. The first critical experiment with a light water moderator was performed in the fall of 1960. Initial criticality with heavy water in the moderator was achieved in February, 1961, and the experiments continued through May, 1963.

Theoretical studies were performed in parallel with the experimental program. Analytical procedures appropriate for D_2O-H_2O

Figures (Cont'd)

moderated lattices were developed and tested using comparisons with experimental data. The basic theoretical model used in the initial phase of the program has been fully reported[1,2]. Modifications and improvements to the initial methods are described in the latter sections of the report, where the final analysis of all of the experimental data appears.

2. DESCRIPTION OF ASSEMBLIES

2.1. Facility

The critical experiments were performed in Bay No. 2 of The Babcock & Wilcox Company Critical Experiment Laboratory using a conventional tank-type facility modified for heavy water use. Full details are given in Reference 3 and in the facility hazards reports[18,19].

The critical assemblies were erected in a 5-foot diameter by 6.5-foot high aluminum core tank mounted inside an existing 9-foot diameter tank as shown in Figure 2-1. (The external paraffin reflector was used only in Core III.) The smaller tank, which minimized heavy water inventory, was hermetically sealed to control moderator degradation by light water vapor in the atmosphere. All components of the moderator system were either aluminum or stainless steel except the Amercoated carbon steel dump tank. The system was mounted in a waterproofed retention basin, and leak detectors were provided at appropriate locations.

Moderator mixtures were prepared in a 900-gallon aluminum mix tank by mixing weighed amounts of demineralized light water and heavy water (99.75% D_2O), and then pumped to the critical experiment dump tank. A 1 ft^3 mixed-bed (Amberlite XE-150) demineralizer and cellulose filter were used to clean the moderator at approximately 6-month intervals. The moderator composition was checked daily with a calibrated hydrometer (±2%); the procedure for more accurate D_2O analyses is given in Section 3.1.1. D_2O losses during the program were minimal. To minimize moderator degradation, the core tank was opened only when necessary, and residual moderator was removed and recovered in a small dehumidifier before major loading changes.

The critical assemblies were provided with at least four 6- to 8-inch wide safety blades. In most cases, the blades were cadmium sheets backed with stainless steel, but Boral was used in some of the more epithermal lattices. The blades were thin enough to pass between rows of fuel rods so that the uniformity of lattice spacing could be maintained.

Normally, all blades were fully withdrawn from the core to avoid perturbations, and criticality was achieved by adjusting the moderator level, the moderator composition, or the core diameter. The safety blades were driven by standard drum-and-cable drive mechanisms.

Details concerning the instrumentation and control system, the startup source, other auxiliary equipment, and operating procedures are given in References 18 and 19.

2.2. Fuel Rods

The physical properties of the fuel rods are summarized in Table 2-1. The uncertainties are standard deviations of the mean obtained from vendor quality control data and check measurements on 50 to 100 randomly selected samples. The impurities are given as the summation of $N_i\sigma_i$, where N_i is the concentration of each impurity per cubic centimeter of the oxide fuel and σ_i is its microscopic absorption cross section. Additional details are given in the referenced reports.

The fuel diameter for the swaged 4.02%-enriched rods was obtained by measuring the OD and wall thickness, since there was no gap between the fuel and cladding. Although the OD was constant, the wall thickness measured by a conductivity method[3] was found to be appreciably larger near the ends. The average clad thickness between 40 and 140 cm was 15.9 ± 0.5 mils, but the average between 10 and 170 cm was 16.6 ± 0.6 mils. The value listed in the table is the $\cos^2$ weighed average between 10 and 170 cm.

The end caps of the 4.02%-enriched rods were approximately 2.35 inches long and consisted of inverted stainless steel thimbles filled with aluminum or stainless steel plugs. The end caps of the 2.46%-enriched rods were 1/8-inch thick aluminum plugs and had a 1-inch long dead space (filled with Kaowool) at the top. The end caps of the UO_2-ThO_2 rods were 3/4-inch thick aluminum plugs and had a 1/2-inch dead space at the top.

Table 2-1. Physical Properties of Fuel Rods

Property	4.02%-UO_2[3]	2.46%-UO_2[14]	UO_2-ThO_2[20]
Outer diameter, in.	0.4755 ± 0.0015	0.4748 ± 0.0006	0.308 ± 0.001
Wall thickness, in.	0.0160 ± 0.0005	0.032 ± 0.001	0.014 ± 0.001
Wall material	#304 Steel	#6061 Aluminum	#1100 Aluminum
Fuel (pellet) diameter, in.	0.444 ± 0.002	0.4054 ± 0.0005	0.260 ± 0.002
Total length, in.	≈71.5	61.59 ± 0.16	62.0 ± 0.2
Active (fuel) length, in.	66.7 ± 0.3	60.37 ± 0.35	60.0 ± 0.1
Weight of fuel, gm/rod	1600 ± 2	1306 ± 1	434.6 ± 0.2
Wt U/wt UO_2, %	88.01 ± 0.02	88.13 ± 0.01	- -
Weight of ThO_2, gm/rod	- -	- -	405.0 ± 0.2
Weight of U^{235}, gm/rod	56.61 ± 0.10	28.42 ± 0.02	24.04 ± 0.02
Enrichment, wt 25/wt U, %	4.020 ± 0.005	2.459 ± 0.002	- -
Atoms Th ÷ atoms U^{235}	- -	- -	15.00 ± 0.05
Bulk fuel density, gm/cm^3	9.46 ± 0.10	10.24 ± 0.04	8.33 ± 0.14
Σ_a (impurity), cm^2/cm^3 oxide	$<5 \times 10^{-4}$	$<4 \times 10^{-4}$	$<6 \times 10^{-3}$

2.3. Core Descriptions

The fuel rods were aligned in a uniform lattice by top, midplane, and bottom grid plates. In all cores except Core I, the top and bottom grid plates were the "egg-crate" type consisting of 1-inch wide slotted aluminum strips interlocked to form a square matrix; in Core I, the end grid plates were 1/2-inch thick drilled stainless steel plates. The midplane grid plates were 1/16-inch thick drilled aluminum sheets except in Cores I and II, where a 1/4-inch thick drilled lucite sheet was used. In Cores XVIII-XX, two midplane grids were used, spaced 49 and 82 cm above the reference plane.

The vertical dimensions of the major cores are shown in Figure 2-2, where the reference plane is at the bottom of the active fuel. The fuel rods rested on a 2-inch thick aluminum base plate on the bottom of the core tank, but the bottom grid plate was elevated by 1/8-inch thick aluminum spacers.

With the exception of the zone-loaded Core VII, the fuel rods were regularly spaced at intervals of the appropriate lattice pitch and were loaded to approximate cylindrical geometry within limits imposed by the finite lattice pitch. A circular cross section was fairly well approximated, even in the smallest cores. The lattice pitches and M/W ratios are listed in Table 2-2, where the uncertainty in the average lattice pitch is less than 0.001 inch. The M/W ratio is defined as the nonmoderator-to-moderator volume ratio, where the fuel and the cladding are both included in the nonmoderator volume.

Table 2-2. Lattice Pitch and M/W Ratio

Lattice pitch		M/W ratio		
In.	Cm	4.02%	2.46%	UO_2-ThO_2
0.670	1.702	- -	0.651	- -
0.595	1.511	1.006	1.001	- -
0.571	1.450	1.195	- -	- -
0.387	0.983	- -	- -	0.990

The zone-loaded assembly (Core VII) is included in this report because some lattice parameter measurements were made in the asymptotic region of the outer UO_2 zone. Elevation and plan views of Core VII are given in Figures 2-3 and 2-4. The inner zone (A) was a 20.124-inch square matrix of 52 by 52 UO_2-ThO_2 fuel rods on a pitch of 0.387 inch surrounded by an outer zone (B) of 4.02%-enriched UO_2 fuel rods on a 0.595-inch pitch. Since the inner zone occupied a square hole formed by the removal of 34 by 34 (20.230 in. square) outer zone rods, an extra 0.053-inch wide moderator channel existed between the two zones.

Representative cores are shown in Figures 2-5 and 2-6. Core XI, fueled with 4.02-enriched UO_2 and moderated by 70% D_2O, was one of the largest cores, and Core XIII, fueled with 2.46%-enriched UO_2 and moderated by light water, was one of the smallest.

Figure 2-1. External View of 5-Foct Diameter Core Tank

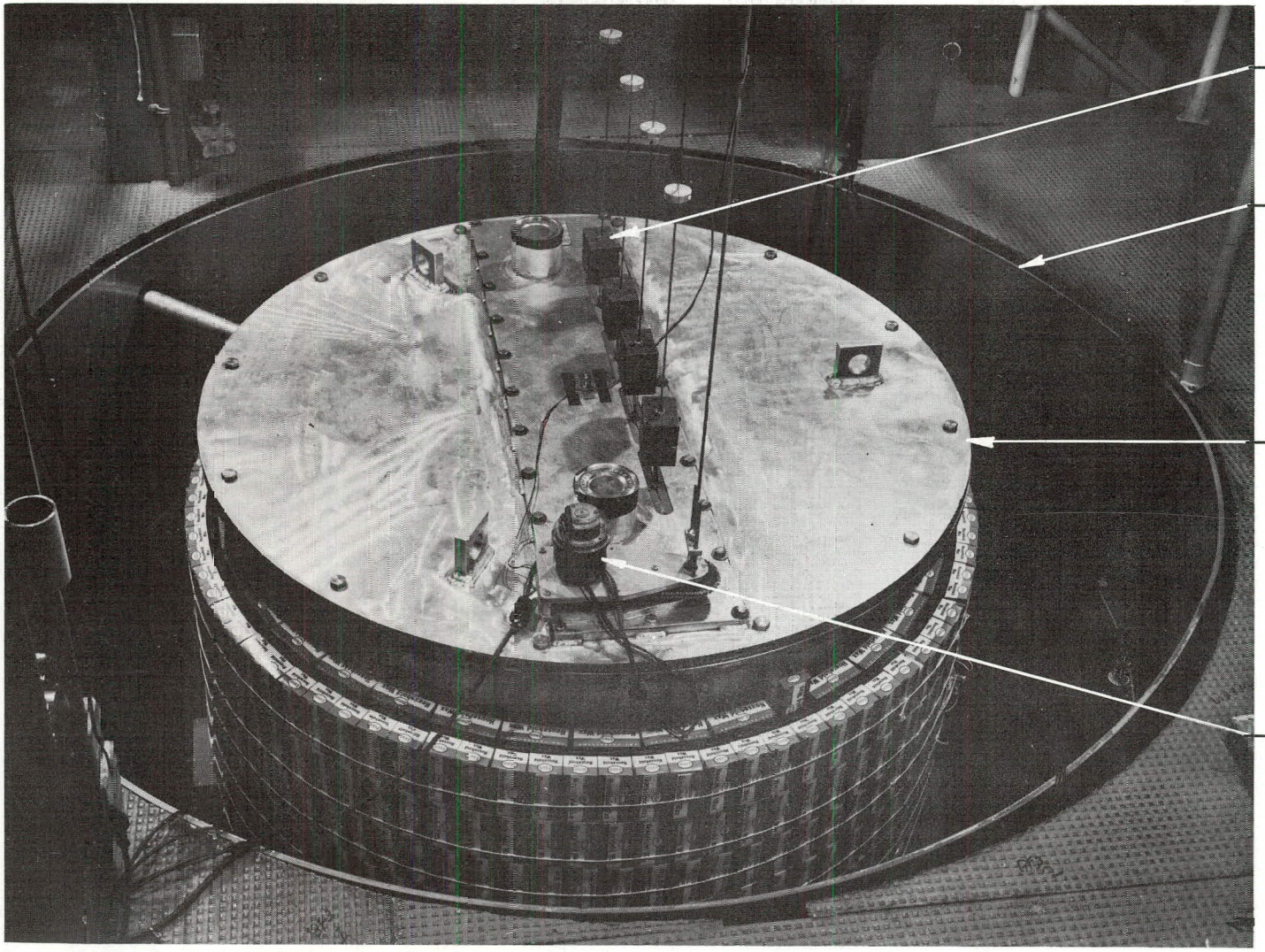

Figure 2-2. Vertical Dimensions of Uniform Lattices

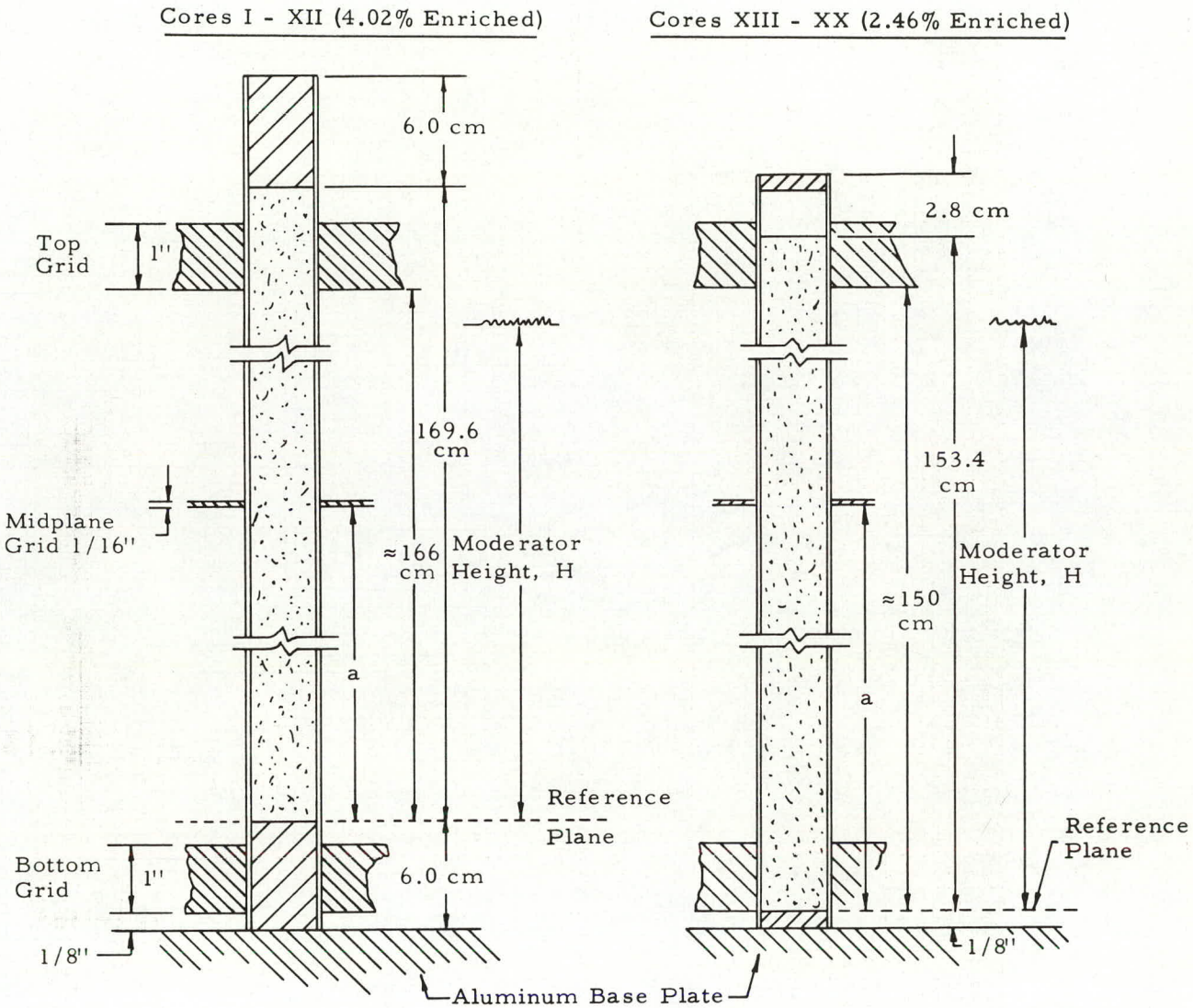

Core	a, cm
I	86
II	65
III-IX	74
X-XII	90
XIII-XV	52
XVI-XVII	60

Figure 2-3. Vertical Dimensions of Zone-Loaded Core VII

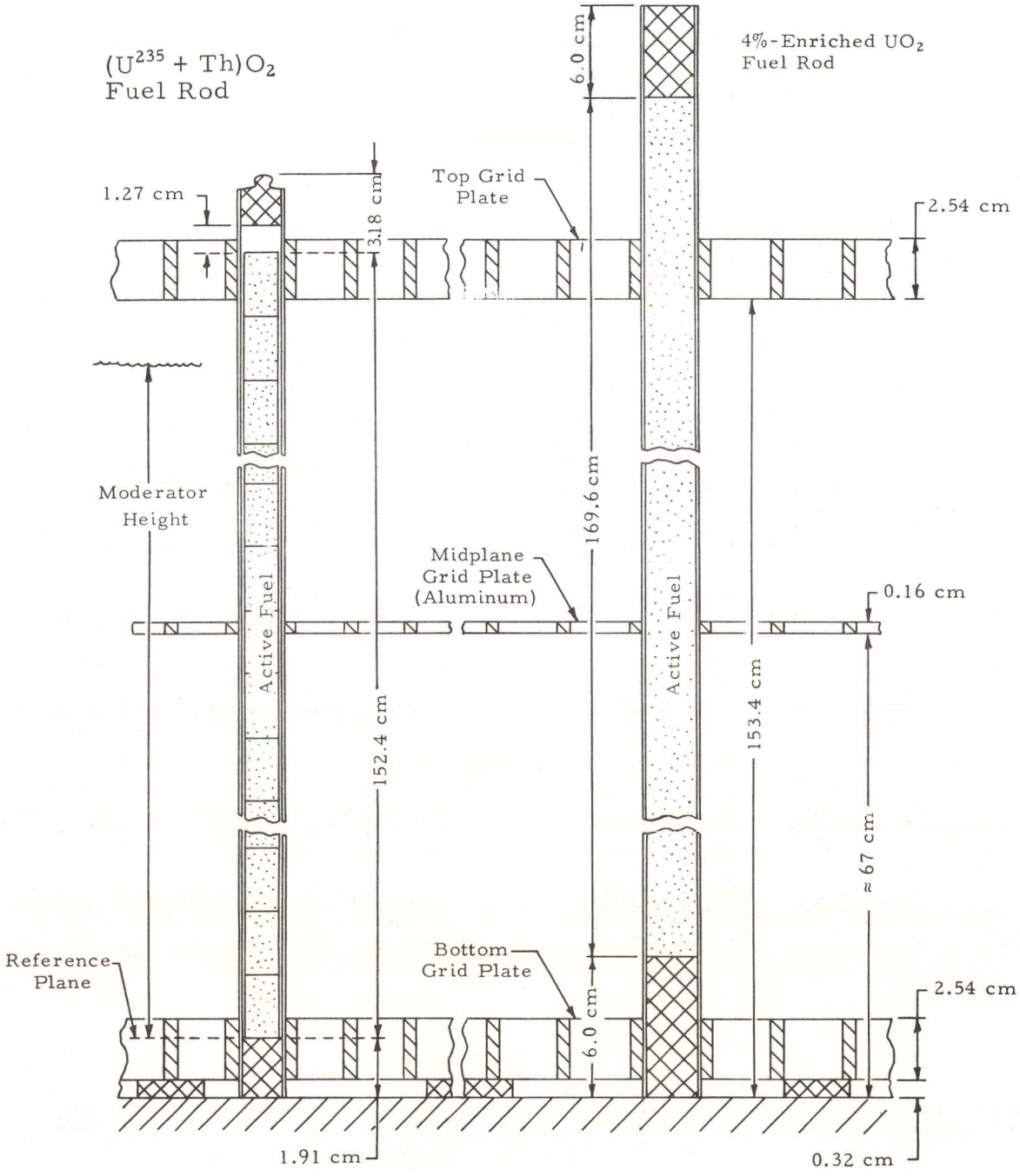

Figure 2-4. Loading Diagram of Core VII

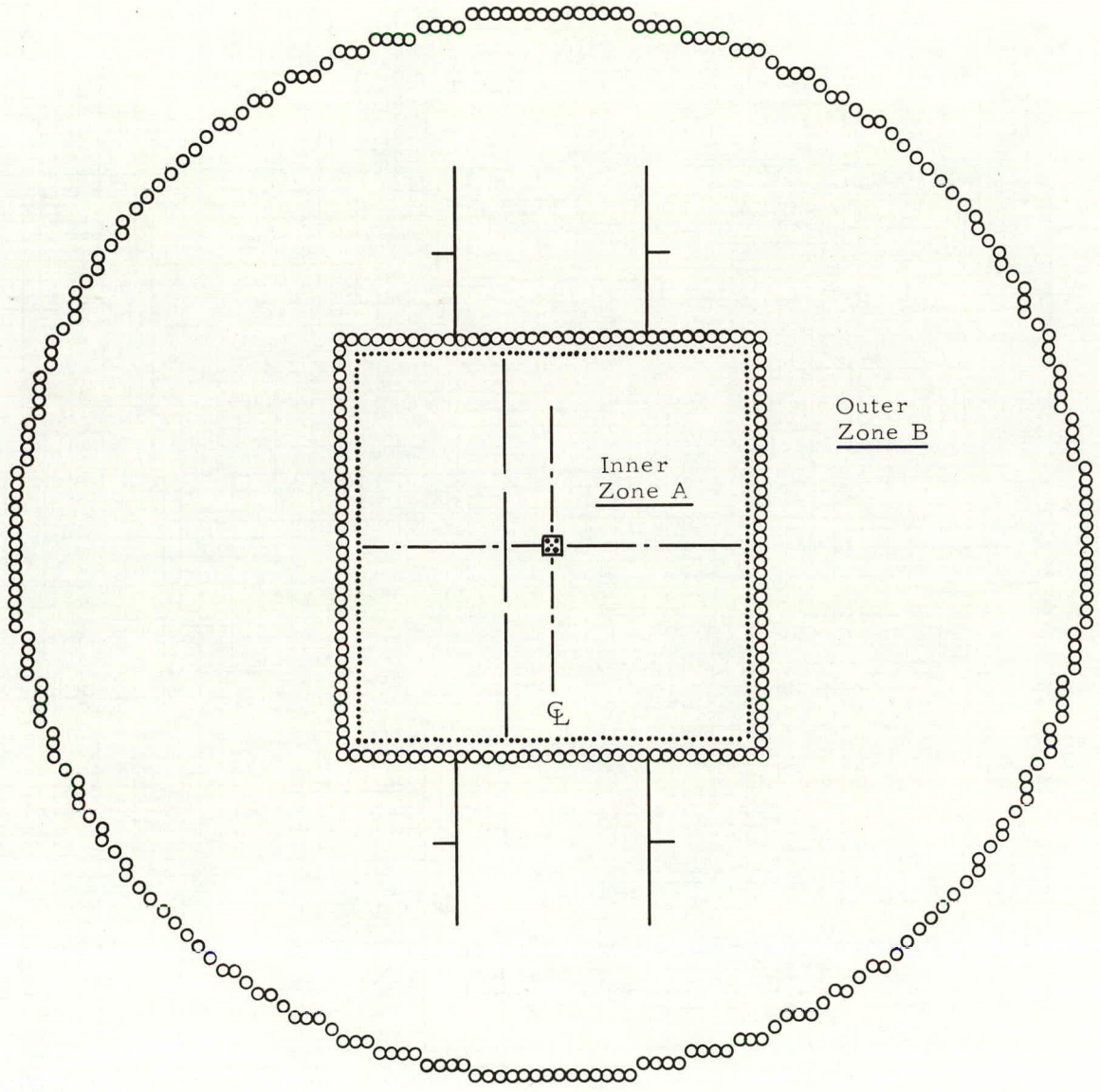

Figure 2-5. View of Core XI

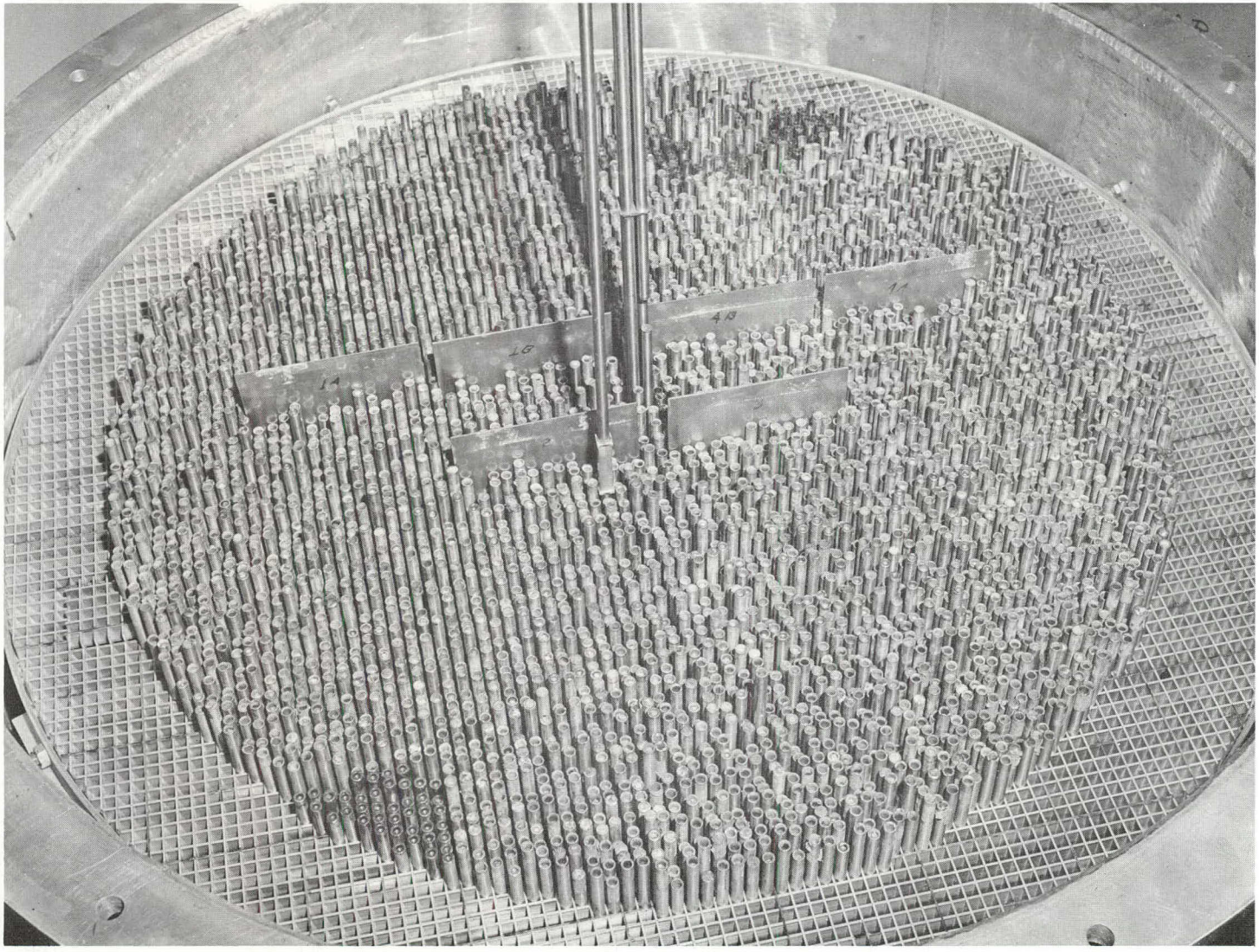

Figure 2-6. View of Core XIII

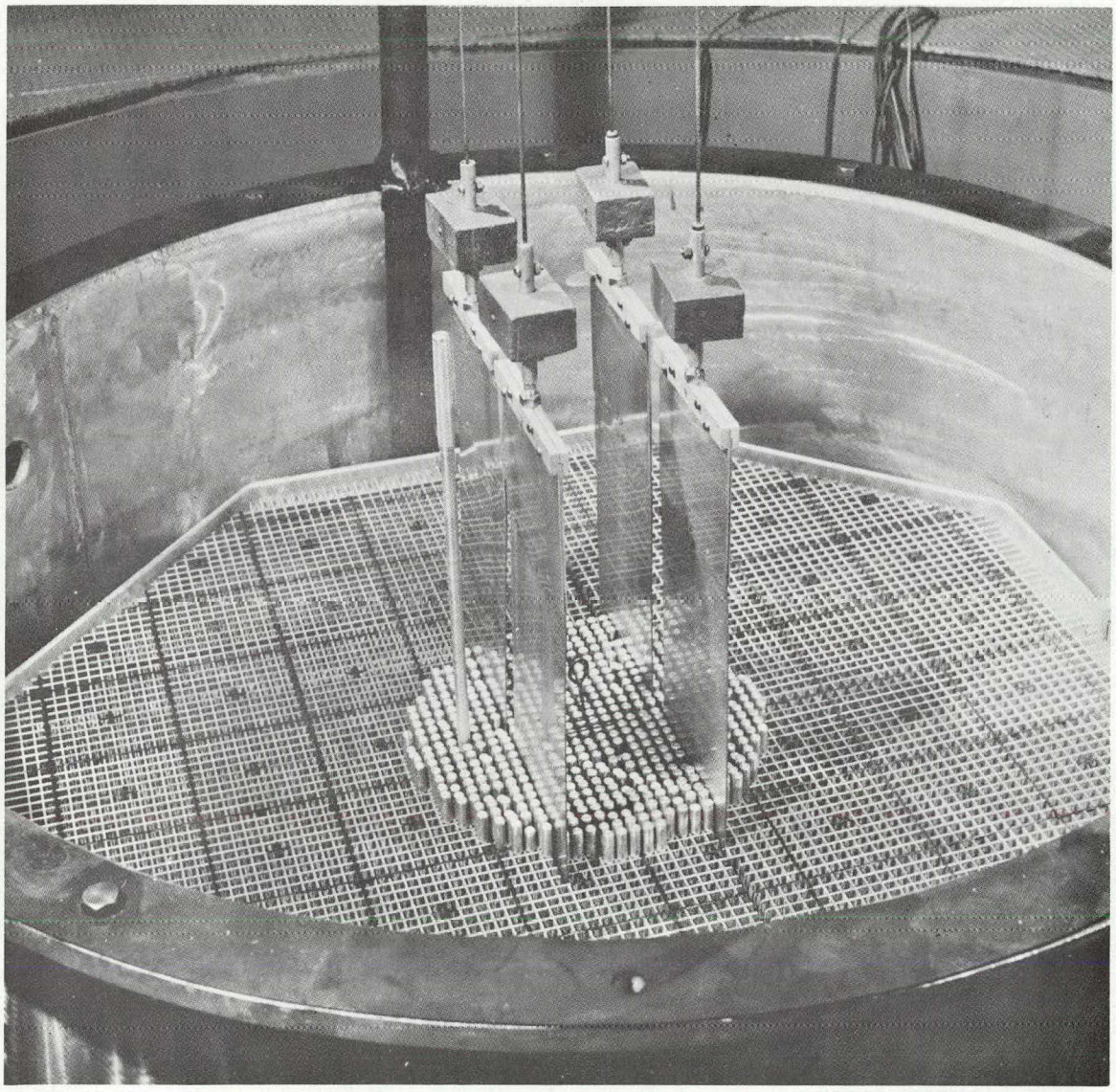

3. CRITICALITY AND REACTIVITY MEASUREMENTS

3.1. Techniques

3.1.1. Moderator Composition

The concentration of D_2O in the moderator was derived from precise density measurements in calibrated pycnometers[3]. The measurements were capable of a precision of about ±0.03%, and the absolute accuracy is conservatively estimated to be ±0.1% in D_2O concentration. Some evidence of moderator degradation at the highest D_2O concentrations was observed by comparing analyses before and after each set of experiments, but the total change was always within the limits quoted. The D_2O concentrations listed in the tables do not include the hydrogen in the boric acid. In some of the cores, boric acid (H_3BO_3) was dissolved in the moderator. The boron concentration, given as grams of natural boron per liter of moderator (gm B/ℓ), was determined by KOH titration[3] to an absolute accuracy of about ±0.5%.

3.1.2. Core Radius

The core radius was computed from the relation,

$$\pi R^2 = (\text{Number of Rods})(\text{Pitch})^2.$$

Since the cores were not perfectly circular in cross section, the validity of the "equal area" assumption was checked in Core I, which had the smallest radius and was most sensitive to irregularities in the core periphery. Another loading of Core I, having the same number of fuel rods arrayed in slightly less circular geometry, was found to be only 7¢ more reactive. The radial bucklings of the two loadings also differed by less than 0.5%.

3.1.3. Reflector Thickness

With the exception of Cores I and II, which were loaded in a 9-foot diameter tank, all cores were assembled in the 60.00 ± 0.25-inch ID by 0.5-inch wall aluminum core tank. Therefore, the radial reflectors

were not infinite, particularly at high D_2O concentrations. The reflector thickness is given as the difference between the inner radius of the core tank and the core radius. Core III was additionally reflected by a 5-inch thick layer of paraffin (0.83 gm/cm^3 effective density) stacked against the outside of the 5-foot diameter core tank. In the axial direction, the cores were reflected by the fuel, the end caps, and the grid plate above the moderator level and by the grid structure, the end caps, and the base plate at the bottom.

3.1.4. Moderator Height

The critical moderator height was measured by a calibrated manometer and by a conductivity-type probe to an absolute accuracy of about ±0.1 cm and a relative accuracy of about ±0.05 cm. Moderator heights were measured relative to a reference plane at the bottom of the fuel (see Figures 2-2 and 2-3) and are given for the condition of all control blades fully withdrawn from the core.

3.1.5. Temperature

The temperature of the moderator in the dump tank was measured each day with a mercury thermometer, accurate to ±0.5 C.

3.2. Critical Size and Composition

The critical parameters of the major cores are summarized in Table 3-1. The two-region, zone-loaded Core VII (see Figure 2-4) is included for completeness; the symbols A and B refer to the inner and outer zones, respectively. In the transitions between major cores, a number of intermediate loadings were assembled, but no attempt was made to shim these loadings to a common critical moderator height. Tables 3-2 and 3-3 summarize the intermediate loadings with and without boric acid in the moderator. In Table 3-3, the results are normalized to a common critical moderator height using $\partial\rho/\partial h$ and $\partial\rho/\partial c$ data from the next section. The last column is the D_2O concentration that would make all intermediate loadings critical at a moderator height of 150.0 cm without the paraffin reflector in Core III.

Table 3-1. Critical Parameters of Major Cores

Core no.	Fuel, wt% U^{235}	M/W ratio	Moderator composition		Number of fuel rods	Core radius, cm	Reflector thickness, cm	Moderator height, cm	Temperature, C
			D_2O, mole %	Boron, gm B/ℓ					
I	4.02	1.006	0.0	0	484	18.75	∞	154.0	15
II	4.02	1.006	0.0	3.39	4904	59.71	∞	146.7	14
III	4.02	1.006	76.5	0	5284	61.98	14.22[a]	152.9	19
IV	4.02	1.006	69.7	0	2252	40.46	35.74	151.0	19
V	4.02	1.006	69.7	0.422	5284	61.98	14.22	145.0	21
VI	4.02	1.006	49.6	1.79	5284	61.98	14.22	147.6	21
VII-A	U-Th	0.990	81.2	0	2704	68.04	8.16	141.3	20
VII-B	4.02	1.006	81.2	0	5212	68.04	8.16	141.3	20
IX	4.02	1.006	49.7	0	952	26.31	49.89	150.6	18
X	4.02	1.195	0.0	0	608	20.18	56.02	146.1	22
XI	4.02	1.195	70.1	0	5320	59.68	16.52	146.1	21
XII	4.02	1.195	49.7	0	1390	30.51	45.69	146.1	21
XIII	2.46	1.001	0.0	0	596	20.82	55.38	141.1	22
XIV	2.46	1.001	70.0	0	2852	45.47	30.73	134.9	20
XV	2.46	1.001	49.8	0	1140	28.79	47.41	134.5	19
VXI	2.46	0.651	85.5	0	5124	68.73	7.47	134.2	21
XVII	2.46	0.651	70.0	0	872	28.35	47.85	134.7	20
XVIII	2.46	1.001	72.1	0	5137	61.11	15.09	107.9	20
XIX	2.46	1.001	50.0	0.778	5137	61.11	15.09	97.7	21
XX	2.46	1.001	0.0	1.675	5137	61.11	15.09	93.2	23

(a) Plus 5 inches of paraffin.

Figure 3-1 shows the dependency of core radius on moderator composition (unborated cases) and illustrates the spectral shift principle. The variation in core radius with boron concentration in the moderator, for a constant D_2O concentration, is seen in Figure 3-2. Figure 3-3 gives the relationship between D_2O and boron concentration in the moderator for constant core diameter and height. These correlations are not exact since comparable cores differed slightly in core diameter, critical height, or temperature. For accurate comparisons, the exact parameters given in the tables should be used in the calculations.

The basis for an estimate of the reproducibility of these criticality measurements is given in Section 3.4. The uncertainty quoted for the moderator composition appears to be adequate and can introduce an error of about 10 cents. Although temperature coefficients were not measured, errors in temperature and in moderator height cannot affect reactivity by more than a few cents. Reactivity effects of midplane grid plates and lack of perfect cylindrical geometry also contribute small errors of this order of magnitude. However, the limiting source of error is probably due to small differences in the composition of the fuel rods, which can introduce an uncertainty of about 20 cents.

3.3. $\partial\rho/\partial h$ and $\partial\rho/\partial c$

Measurements of $\partial\rho/\partial h$ were made by raising the moderator level to h', a few centimeters above the critical moderator height h_c, by determining the stable reactor period over several decades, and by converting the period to reactivity using an inhour relation computed for the particular core. Errors due to deuterium photoneutrons were minimized by making only one measurement per run, separating runs by several hours, and disregarding period data during the first few decades. Changes in moderator level were measured with a remotely operated conductivity probe, accurate to ± 0.05 cm.

In many of the cores, the critical moderator level was changed in small increments by adding or removing peripheral fuel rods, and $\partial\rho/\partial h$ was measured at a number of moderator heights. The usual formulation

$$\frac{\partial\rho}{\partial h} = \frac{-2\pi^2}{(\bar{h} + \delta_z)^3}\left[\frac{1}{k^2}\frac{\partial k}{\partial B^2}\right]$$

was used to correlate the data, where δ_z is the axial reflector savings and $\overline{h}$ is the average value of h_c and h'. As shown in Figures 3-4 and 3-5, which are typical examples for the 4.02%- and 2.46%-enriched fuels, the relationship appears to be linear to 15 to 20 cm below the top of the fuel. Therefore, the function $(1/k^2)(\partial k/\partial B^2)$, which is derived from the linear part of the curve, can be used to test theoretical models of neutron slowing down and leakage.

The results, summarized in Table 3-4, can be converted to absolute units using the values of β_{eff} computed for each core. The standard deviations of the results are in the range of 3 to 5%, but larger systematic errors may be present if the $\partial\rho/\partial h$ data are not on the linear part of the $\partial\rho/\partial h$ vs $(h + \delta_z)^3$ curve. The results marked with an asterisk in Table 3-4 are for cases where the curve is not sufficiently well defined to ensure the quoted accuracy. The data for Cores XVIII through XX are much more limited and are accurate to about 5 to 10%. These results are shown in parentheses in Table 3-4.

Table 3-2. Critical Parameters of Intermediate Loadings With Boron

Core and loading numbers	Fuel, wt% U^{235}	M/W ratio	Moderator composition		Number of fuel rods	Core radius, cm	Reflector thickness, cm	Moderator height, cm	Temperature, C
			D_2O, mole %	Boron, gm B/ℓ					
I-7	4.02	1.006	0.0	0.000	484	18.75	∞	154.0	13
II-2	4.02	1.006	0.0	0.242	576	20.46	∞	150.5	10
II-3	4.02	1.006	0.0	0.460	724	22.94	∞	96.8	11
II-4	4.02	1.006	0.0	0.686	764	23.57	∞	135.5	11
II-5	4.02	1.006	0.0	1.152	936	26.09	∞	167.5	12
II-6	4.02	1.006	0.0	1.658	1280	30.51	∞	142.5	12
II-8	4.02	1.006	0.0	2.342	2024	38.36	∞	125.1	13
II-10	4.02	1.006	0.0	3.163	3792	52.51	∞	157.2	14
II-11	4.02	1.006	0.0	3.257	4904	59.71	∞	~120.0	14
II-12	4.02	1.006	0.0	3.389	4904	59.71	∞	146.7	14
IV-2	4.02	1.006	69.7	0.000	2252	40.46	35.74	151.0	19
V-1	4.02	1.006	69.7	0.180	5284	61.98	14.22	~ 94.5	21
V-2	4.02	1.006	69.7	0.361	5284	61.98	14.22	127.0	21
V-3	4.02	1.006	69.7	~0.376	5284	61.98	14.22	131.0	21
V-4	4.02	1.006	69.7	0.401	5284	61.98	14.22	139.3	21
V-5	4.02	1.006	69.7	0.422	5284	61.98	14.22	145.0	21
V-5	4.02	1.006	69.7	0.422	5284	61.98	14.22	145.0	21
VI-1	4.02	1.006	62.1	0.701	5284	61.98	14.22	92.5	22
VI-2	4.02	1.006	55.6	1.22	5284	61.98	14.22	102.0	22
VI-3	4.02	1.006	49.6	1.66	5284	61.98	14.22	113.0	23
VI-4	4.02	1.006	49.6	1.73	5284	61.98	14.22	132.2	22
VI-5	4.02	1.006	49.6	1.79	5284	61.98	14.22	147.6	21

Table 3-3. Critical Parameters of Intermediate Loadings Without Boron

Core and loading numbers	Fuel, wt% U^{235}	M/W ratio	D_2O, mole %	Number of fuel rods	Core radius, cm	Reflector thickness, cm	Moderator height, cm	Temperature, C	D_2O, mole % (for h = 150 cm)
III-11	4.02	1.006	76.41	5284	61.98	14.22[a]	169.8	19	--
III-12	4.02	1.006	76.32	5284	61.98	14.22[a]	148.3	19	75.89[b]
III-13	4.02	1.006	76.50	5284	61.98	14.22[a]	152.9	19	75.90[b]
III-17	4.02	1.006	76.50	4780	58.95	17.25[a]	164.6	19	75.58[b]
III-18	4.02	1.006	75.50	4780	58.95	17.25	148.0	19	75.57
III-19	4.02	1.006	75.50	4300	55.91	20.29	157.5	19	75.25
III-20	4.02	1.006	73.77	4296	55.89	20.31	122.6	19	75.15
III-21	4.02	1.006	73.77	3544	50.76	25.44	139.0	19	74.22
III-22	4.02	1.006	73.77	5284	61.98	14.22	110.8	19	75.96
III-23	4.02	1.006	73.77	3204	48.26	27.94	158.0	19	73.52
III-24	4.02	1.006	71.33	2536	42.94	33.26	156.0	19	71.12
III-25	4.02	1.006	69.70	2380	41.60	34.61	137.2	19	70.26
IV-1	4.02	1.006	69.70	2292	40.82	35.38	146.0	19	69.86
IV-2	4.02	1.006	69.70	2252	40.46	35.74	151.0	19	69.66
XI-6	4.02	1.195	70.07	5320	59.68	16.52	146.1	21	--
XI-7	4.02	1.195	69.07	5320	59.68	16.52	126.0	21	--
XI-8	4.02	1.195	68.07	5320	59.68	16.52	113.2	21	--

(a) Plus 5 inches of paraffin.

(b) Without paraffin.

Table 3-4. Summary of $\partial\rho/\partial h$ Data

Core no.	Fuel, wt% U^{235}	M/W ratio	Moderator composition		$(1/k^2)(\partial k/\partial B^2)$, $\times 10^5$ cents-cm^2	β_{eff}
			D_2O, mole %	Boron, gm B/ℓ		
I	4.02	1.006	0.0	0	4.19 ± 0.23*	0.00770
II	4.02	1.006	0.0	3.39	--	0.00696
III	4.02	1.006	76.5	0	7.98 ± 0.30*	0.00703
III-21, 22	4.02	1.006	73.8	0	8.21 ± 0.36	--
IV	4.02	1.006	69.7	0	7.90 ± 0.35*	0.00712
V	4.02	1.006	69.7	0.422	7.77 ± 0.17	0.00706
VI	4.02	1.006	49.6	1.79	6.04 ± 0.18	0.00704
IX	4.02	1.006	49.7	0	6.13 ± 0.18*	0.00737
X	4.02	1.195	0.0	0	4.72 ± 0.42	0.00766
XI	4.02	1.195	70.1	0	7.73 ± 0.20	0.00707
XII	4.02	1.195	49.7	0	6.63 ± 0.29	0.00730
XIII	2.46	1.001	0.0	0	5.00 ± 0.27*	0.00762
XIV	2.46	1.001	70.0	0	9.02 ± 0.32	0.00714
XV	2.46	1.001	49.8	0	7.01 ± 0.16	0.00737
XVI	2.46	0.651	85.5	0	11.0 ± 0.22	0.00704
XVII	2.46	0.651	70.0	0	9.06 ± 0.23	0.00725
XVIII	2.46	1.001	72.1	0	(10.1)	0.00709
XIX	2.46	1.001	50.0	0.778	(7.7)	0.00698
XX	2.46	1.001	0.0	1.675	(5.1)	0.00688

In several of the cores approximate values of $\partial\rho/\partial c$, the change in reactivity per unit percent change in D_2O concentration (i. e., c_1-c_2), were obtained incidental to other measurements. The results are listed in Table 3-5, where the accuracy is about ±10%.

Table 3-5. Summary of $\partial\rho/\partial c$ Data

Core no.	Fuel, wt% U^{235}	M/W ratio	D_2O, mole %	$\partial\rho/\partial c$, ¢/% D_2O
III	4.02	1.006	76.5	87
XI	4.02	1.195	70.1	77
XII	4.02	1.195	49.7	48
XVI	2.46	0.651	85.5	163
XVIII	2.46	1.001	72.1	98

3. 4. Miscellaneous Reactivity Measurements

The reactivity worth of peripheral fuel rods, including both fuel addition and resultant moderator displacement, was measured to be 3.7, 3.7, 1.0, 3.6, and 1.8¢/rod for Cores I, X, XII, XIII, and XVII, respectively.

The reactivity change upon removing fuel rods from the center of the core was positive because these lattices were undermoderated. The reactivity increase, in ¢/rod, was 3.7 and 4.0 for the removal of 4 and 16 rods, respectively, in Core XI and 5.2 for the removal of four rods in Core XIII.

The reactivity worth of the paraffin reflector used in Core III was measured to be 42 ± 2 cents.

The reactivity worth of the thin aluminum midplane grid plates (see Section 2.3) was measured at two moderator compositions. Including both neutron absorptions and moderator displacement, the reactivity worth of the midplane grid plate was less than 6.5 cents in Core III and approximately 3 cents in Core XV. Since these effects were negligible in comparison with other sources of reactivity error discussed below, no further measurements were made.

Some information on the reproducibility of criticality measurements was obtained during the program. The first loading of Core II (unborated) was 15 cents more reactive than Core I, and a repeat loading of Core XIV differed by 18 cents. The discrepancy for Core I (H_2O) can be attributed to minor differences in the grid plates used in Cores I and II, and the change in Core XIV (70% D_2O) can be explained by moderator differences within analytical errors. However, a repeat loading of Core IV differed from its original value by about 40 cents. At most, only half of this discrepancy can be assigned to differences in moderator composition, since analytical errors larger than $\pm 0.1\%$ were shown to be improbable. A more plausible explanation is that the reproducibility of these experiments is limited to approximately 20 cents due to minor differences in the composition of the fuel rods. These differences are exhibited when the fuel rods are unloaded and reloaded in regions of different importance.

Figure 3-1. Core Radius Vs D_2O Concentration

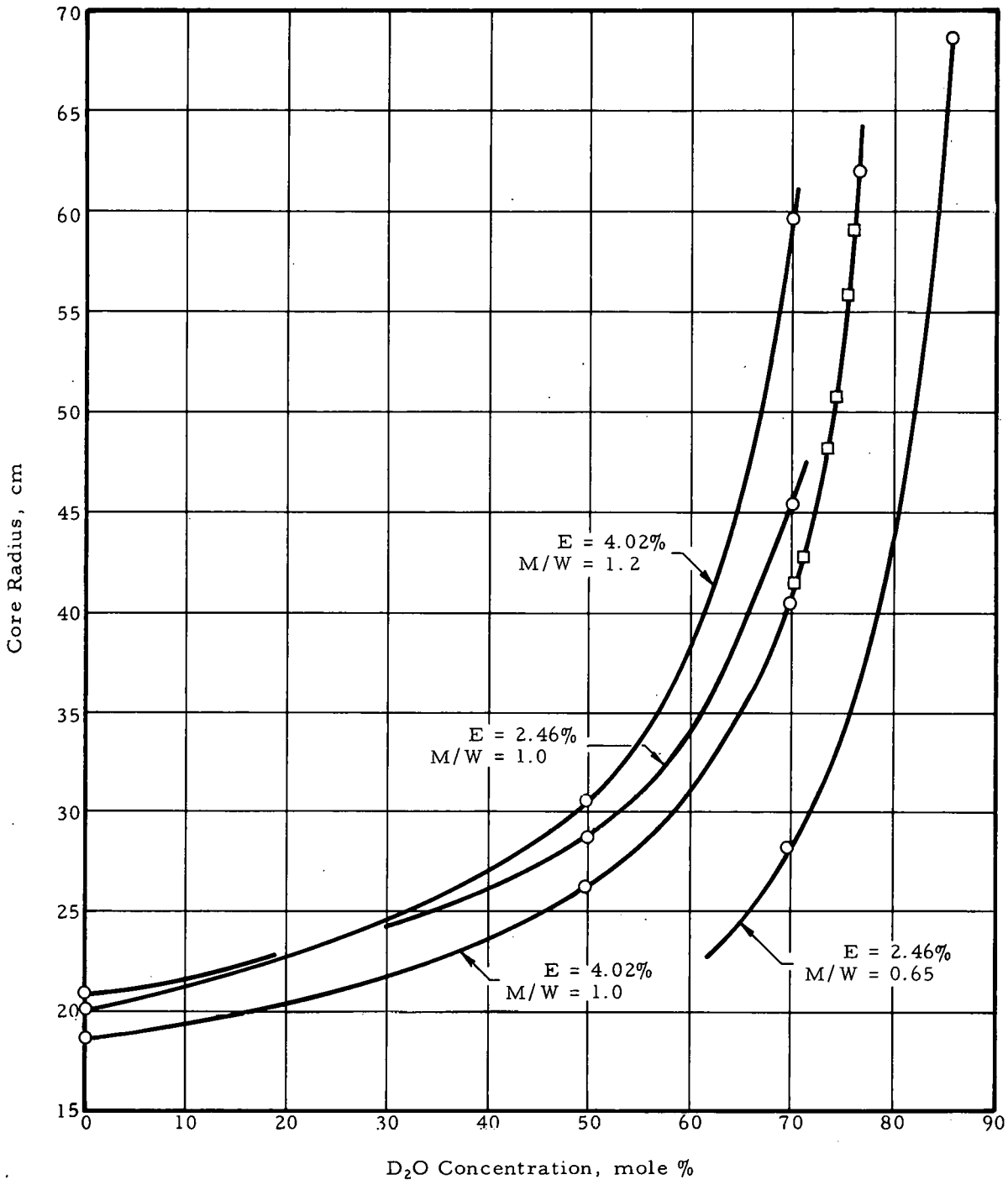

Figure 3-2. Core Radius Vs Boron Concentration

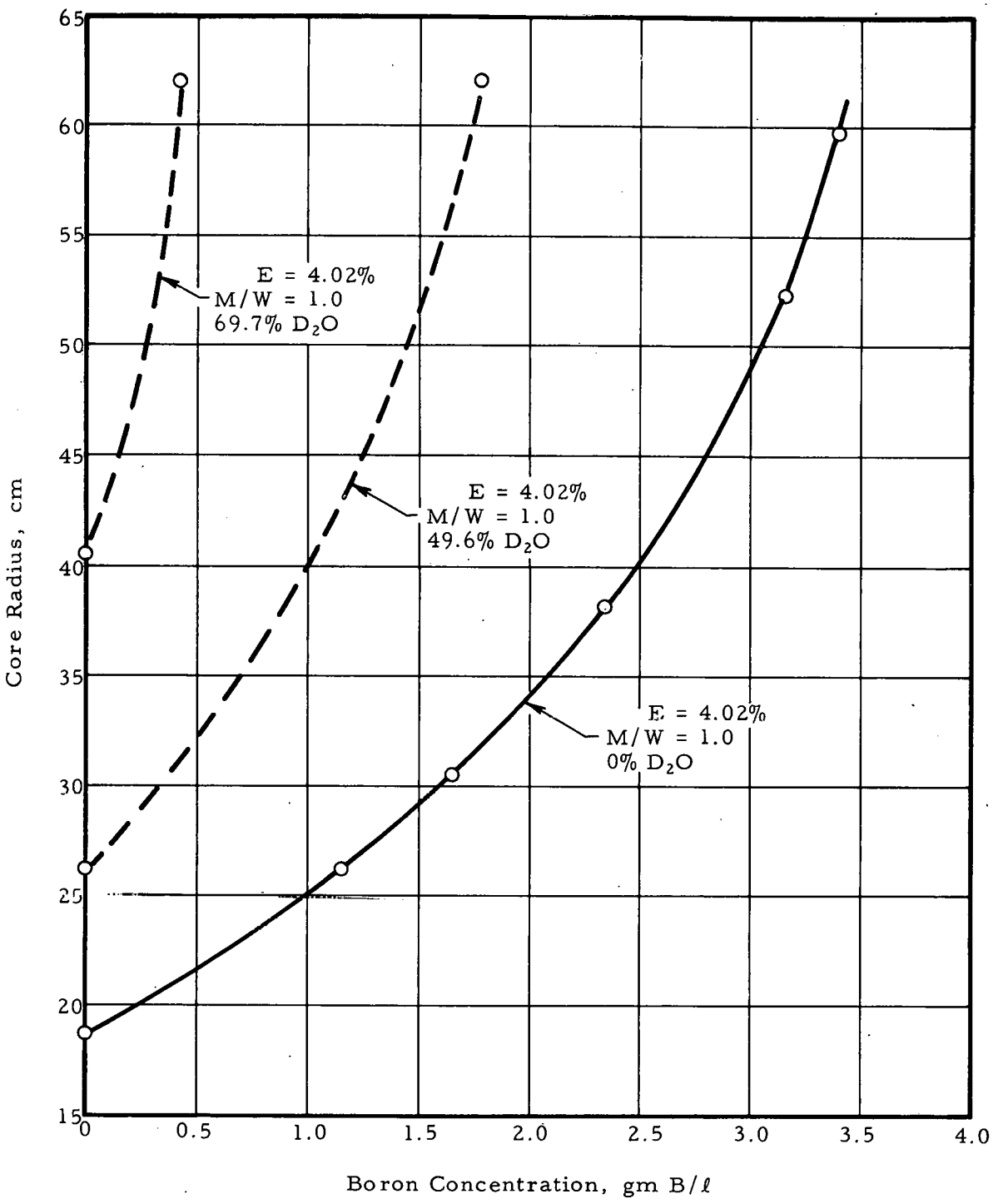

Figure 3-3. D_2O Vs Boron Concentration for Constant Core Size

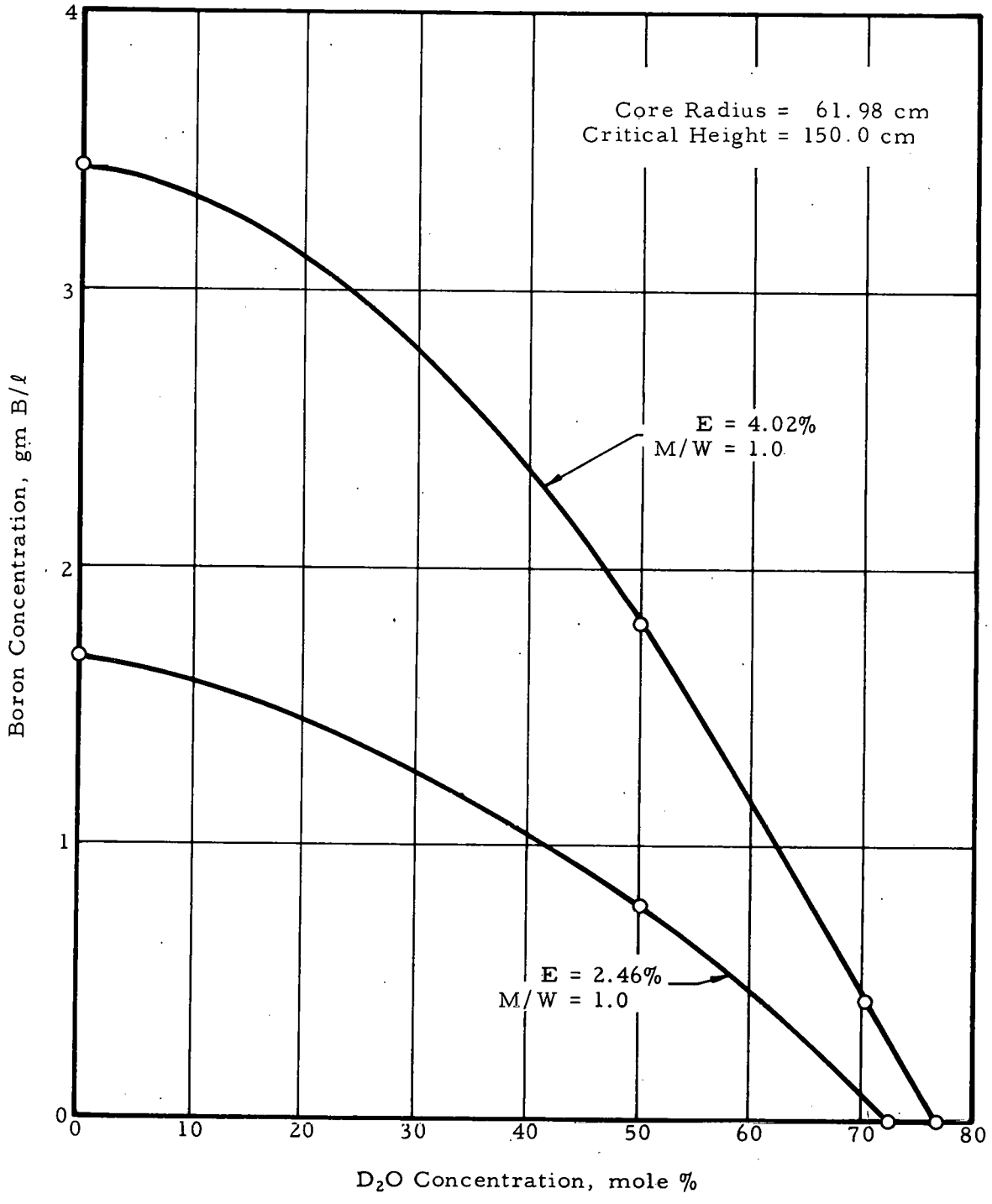

Figure 3-4. $(\partial\rho/\partial h)^{-1/3}$ Vs h_c (Cores III, IV)

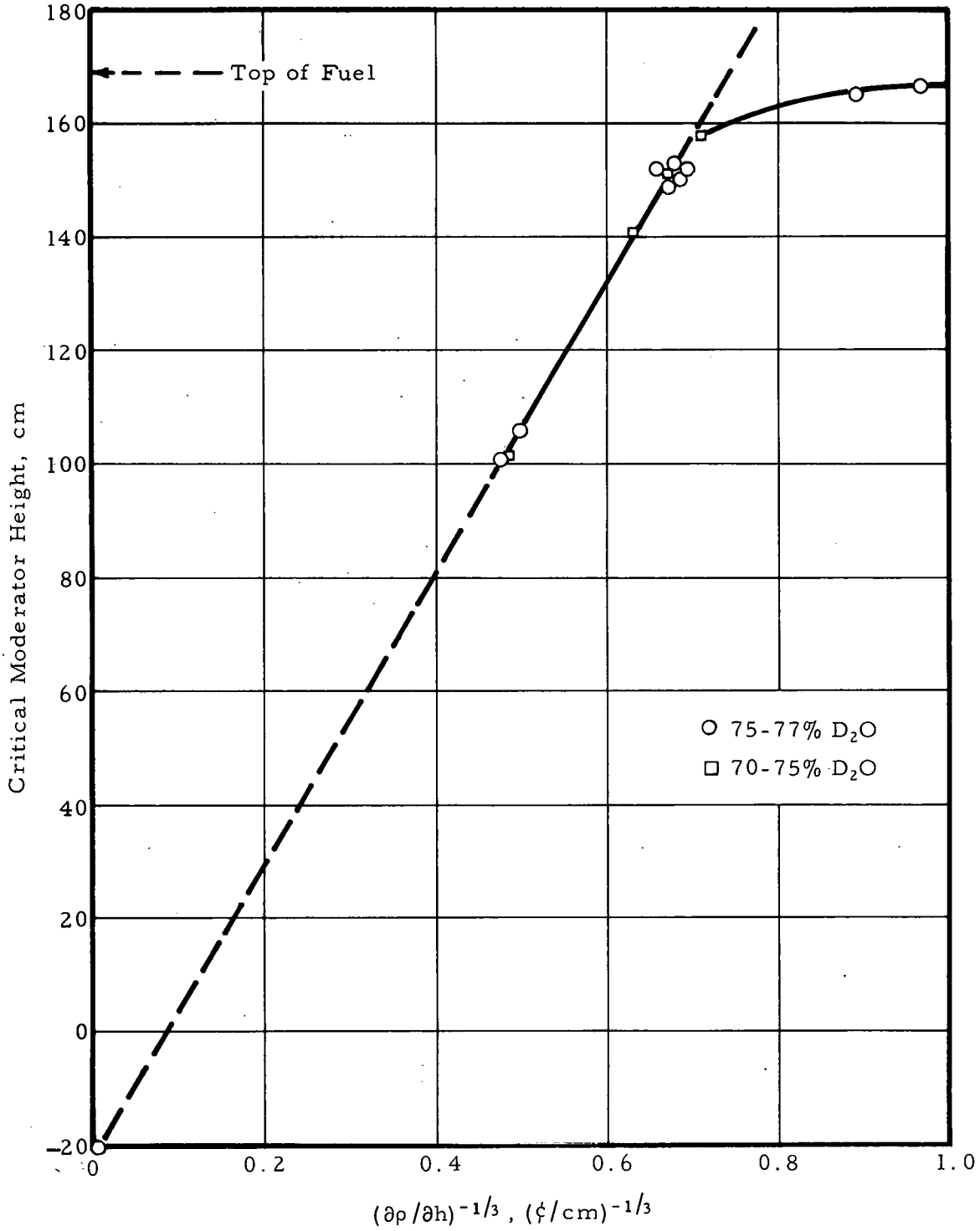

Figure 3-5. $(\partial\rho/\partial h)^{-1/3}$ Vs $\bar{h}$ (Core XIII)

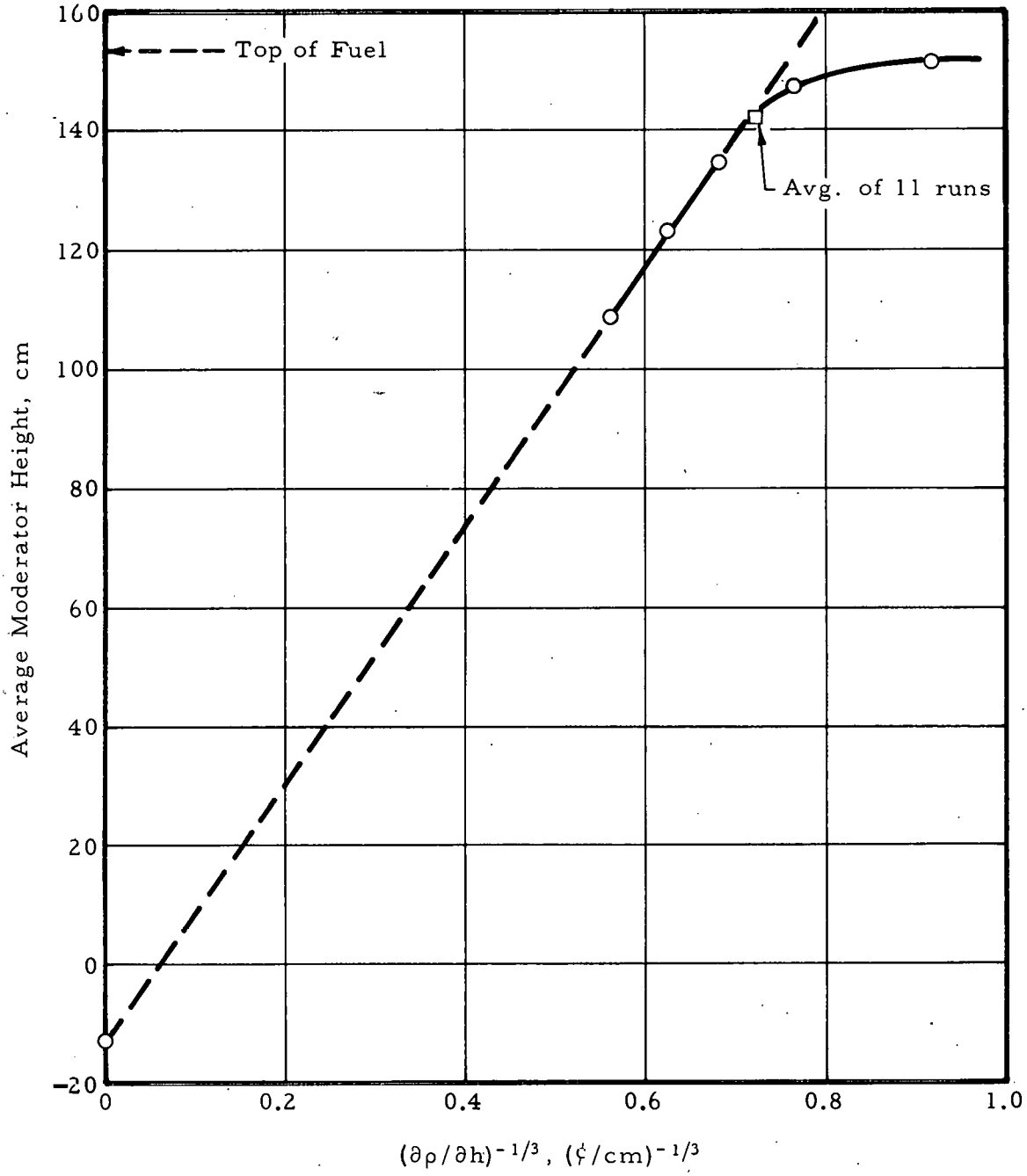

4. BUCKLING AND REFLECTOR SAVINGS

4.1. Critical Buckling

4.1.1. Experimental Techniques

Radial and axial bucklings were derived from least-square fits in the asymptotic region of radial and axial flux traverses to the functions,

$$A(r) = A_r J_o [B_r(r - r_o)]$$

$$A(z) = A_z \cos [B_z(z - z_o)]$$

Flux distributions were measured with 0.259-inch diameter by 0.005-inch thick gold foils, covered either with 0.017-inch thick aluminum (bare) or 0.020 inch thick cadmium. Except in the light water cores and in Cores IV, V, VI, and IX, thin spring-steel tapes, 0.005-inch thick by 1/2 or 3/4 inch wide, were used as foil holders. In the excepted cores, the foil holders were 1/16-inch thick by 1-inch wide lucite stringers. Comparative measurements in Cores I, III, and X showed that neither foil holder perturbed the flux distribution significantly.

The foil holders for radial measurements were inserted between fuel rods and in a plane within several inches of the core midplane; axial measurements were made in the central moderator channel. In the radial traverses, bare foils were spaced at intervals of a single lattice pitch and cadmium-covered foils were spaced at double-pitch intervals. The spacing in the axial direction was always 5 cm.

The foils were irradiated with all control blades withdrawn for 20 minutes at a power level of several hundred watts and then counted once on each side in each of three end-window gas-flow proportional counters. Count rates were at least 10,000 counts/min and usually much higher. Saturated activities were obtained by averaging the data, correcting for background, and applying standard irradiation, decay, and counting

time corrections. Bare and cadmium-covered runs were normalized by at least three gold monitor foils, and gold cadmium ratios ranged from 1.2 to 2.0. Usually at least one bare and one cadmium-covered traverse of each type was made in each core.

Three criteria were used to determine the extent of the asymptotic region in each core:

1. Constant gold cadmium ratio.
2. Constant buckling as the range of the fit was changed.
3. Agreement between bucklings obtained from bare and cadmium-covered data.

Occasionally it was necessary to make a small correction to the axial buckling when the moderator height during the flux run differed from the unperturbed critical moderator height due to perturbations by the foils, cadmium covers, and foil holders. The correction

$$\Delta B_z = \frac{-B_z^2}{\pi} \Delta h$$

was usually less than 3%.

4.1.2. Results and Discussion

The buckling measurements in the major cores are summarized in Table 4-1 and compared in Figures 4-1 and 4-2. To complete the correlation at higher D_2O concentrations, the results of related exponential experiments[4] are included here.

Fuel, wt% U^{235}	M/W ratio	D_2O, mole %	Material buckling, $\times 10^{4}$ cm^{-2}
4.02	1.006	89.1	$-(4.68 \pm 0.06)$
4.02	1.006	80.6	$+(6.53 \pm 0.07)$

Table 4-1. Critical Buckling of Major Cores

Core no.	Fuel, wt% U^{235}	M/W ratio	Moderator composition		Buckling, $\times 10^{-4}$ cm^{-2}		
			D_2O, mole %	Boron, gm B/ℓ	Radial	Axial	Critical
I	4.02	1.006	0.0	0	84.4 ± 0.4	3.60 ± 0.02	88.0 ± 0.4
II	4.02	1.006	0.0	3.39	13.3 ± 0.2	3.87 ± 0.01	17.2 ± 0.2
III	4.02	1.006	76.5	0	7.53 ± 0.10	3.24 ± 0.04	10.77 ± 0.10
III-21	4.02	1.006	73.8	0	10.40 ± 0.08	3.93 ± 0.04	14.33 ± 0.09
III-22	4.02	1.006	73.8	0	8.54 ± 0.08	5.55 ± 0.05	14.09 ± 0.09
IV	4.02	1.006	69.7	0	15.13 ± 0.10	3.47 ± 0.02	18.60 ± 0.10
V	4.02	1.006	69.7	0.422	10.68 ± 0.10	3.55 ± 0.02	14.23 ± 0.10
VI	4.02	1.006	49.6	1.79	12.25 ± 0.08	3.53 ± 0.02	15.78 ± 0.08
VII-A	U-Th	0.990	81.2	0	--	3.88 ± 0.03	--
VII-B	4.02	1.006	81.2	0	--	3.82 ± 0.06	--
IX	4.02	1.006	49.7	0	40.4 ± 0.5	3.59 ± 0.02	44.0 ± 0.5
X	4.02	1.195	0.0	0	75.0 ± 1.0	3.95 ± 0.04	79.0 ± 1.0
XI	4.02	1.195	70.1	0	8.88 ± 0.04	3.52 ± 0.05	12.40 ± 0.07
XII	4.02	1.195	49.7	0	30.9 ± 0.3	3.73 ± 0.02	34.6 ± 0.3
XIII	2.46	1.001	0.0	0	66.0 ± 0.7	4.07 ± 0.06	70.1 ± 0.7
XIV	2.46	1.001	70.0	0	13.18 ± 0.10	4.29 ± 0.03	17.47 ± 0.10
XV	2.46	1.001	49.8	0	34.9 ± 0.5	4.48 ± 0.02	39.4 ± 0.5
XVI	2.46	0.651	85.5	0	8.59 ± 0.06	4.20 ± 0.04	12.79 ± 0.07
XVII	2.46	0.651	70.0	0	29.4 ± 0.5	4.48 ± 0.04	33.7 ± 0.3
XVIII	2.46	1.001	72.1	0	8.76 ± 0.06	5.99 ± 0.05	14.75 ± 0.08
XIX	2.46	1.001	50.0	0.778	11.79 ± 0.14	7.12 ± 0.03	18.91 ± 0.14
XX	2.46	1.001	0.0	1.675	12.4 ± 0.3	7.82 ± 0.04	20.2 ± 0.3

The standard deviations of the results listed in Table 4-1 are of the order of ±1% or better based on statistical combinations of the least-square fits in the asymptotic region to all the bare and cadmium-covered flux traverses in each core. Several potential sources of systematic error were investigated. Foil interactions for the cadmium-covered traverses on double-pitch intervals were shown to be small by repeating some of the traverses on single-pitch intervals and obtaining the same buckling within combined standard deviations. Perturbations by the lucite and steel foil holders were found to be negligible by comparing the results with bucklings derived from bare, unsupported gold wire irradiations at the lowest (Cores I and X) and highest (Core III) D_2O concentrations.

The extent of the asymptotic region in each core was carefully examined by comparing bare and cadmium-covered traverses. With very few exceptions, the bucklings agreed within combined standard deviations, and no systematic difference was evident upon re-evaluation of all the data. The error in the approximation of cylindrical geometry was checked in the smallest core (Core I) by measuring the buckling in another loading having less circular cross section. The two radial bucklings agreed within ±0.5%.

Anisotropy was investigated in two loadings of Core III (21 and 22) having the same composition but differing substantially in height-to-diameter ratio. Although the total bucklings differed by slightly more than their combined standard deviations, the disagreement was small and may have been statistical. Other evidence that anisotropic effects in these cores are small is given by the agreement between critical and exponential bucklings.

4.2. Reflector Savings

Reflector savings were derived from the measured radial and axial bucklings using the standard relations

$$\delta_r = (2.4048/B_r) - R$$

$$\delta_z = (3.1416/B_z) - H$$

where δ_r and δ_z are the radial and axial reflector savings, R is the critical core radius, and H is the critical moderator height. The results for the

major cores are summarized in Table 4-2, and some intermediate loadings are described in Table 4-3. In Tables 4-2 and 4-3, reflector savings are accurate to ±0.4 cm, or better, in the radial direction and to ±1 cm in the axial direction. The radial reflector thickness is given as the inner radius of the core tank (76.20 cm) less the core radius. Additional radial reflection may be obtained from the 0.5-inch thick aluminum core tank wall and, in the cases noted, the external 5-inch thick paraffin reflector. The axial reflector thickness is arbitrarily stated as the difference between the active fuel length (see Figures 2-2 and 2-3) and the critical moderator height. The end plugs on the fuel rods and the grid plates, of course, complicate the analysis.

4.2.1. Reflector Savings Vs Reflector Thickness

Although the data are too limited to permit an accurate correlation, the relationship between reflector savings and reflector thickness can be seen in Figure 4-3. The radial reflector savings decrease as the D_2O concentration is reduced and saturate at a smaller reflector thickness. The different reflecting properties of hydrogen alter the shape of the curve with the additional paraffin reflector. The figure also summarizes one series of measurements where the axial reflector savings can be correlated against axial reflector thickness (or critical height). The axial reflector savings become constant for a thickness slightly greater than 20 cm, which agrees with $\partial\rho/\partial h$ vs h data.

Table 4-2. Reflector Savings of Major Cores

Core and loading numbers	Radial dimensions, cm			Axial dimensions, cm		
	Core radius	Reflector thickness	Reflector savings	Critical height	Reflector thickness	Reflector savings
I	18.75	∞	7.4	154.0	15.6	11.6
II	59.71	∞	6.2	146.7	22.9	13.1
III	61.98	14.22[a]	25.7	152.9	16.7	21.6
III-21	50.76	25.44	23.8	≈139.0	≈30.6	≈19.5
III-22	61.98	14.22	20.3	110.8	58.8	22.6
IV	40.46	35.74	21.4	151.0	18.6	17.6
V	61.98	14.22	11.6	145.0	24.6	22.0
VI	61.98	14.22	6.7	147.6	22.0	19.7
VII-A	--	--	--	141.3	11.1	18.2
VII-B	--	--	--	141.3	28.3	19.5
IX	26.31	49.89	11.5	150.6	19.0	15.2
X	20.18	56.02	7.6	146.1	23.5	12.1
XI	59.68	16.52	21.4	146.1	23.5	21.0
XII	30.51	45.69	12.8	146.1	23.5	16.5
XIII	20.82	55.38	8.8	141.1	12.3	14.6
XIV	45.47	30.73	20.7	134.9	18.5	16.9
XV	28.79	47.41	11.9	134.5	18.9	14.0
XVI	68.73	7.47	13.3	134.2	19.2	19.1
XVII	28.35	47.85	16.0	134.7	18.7	13.7
XVIII	61.11	15.09	20.1	107.9	45.5	20.4
XIX	61.11	15.09	8.9	97.7	55.7	20.1
XX	61.11	15.09	7.2	93.2	60.2	19.1

[a] Plus 5 inches of paraffin.

Table 4-3. Reflector Savings of Intermediate Loadings

Core and loading numbers	D_2O, mole %	Buckling, $\times 10^{-4}$ cm^{-2}			Radial parameters, cm			Axial parameters, cm		
		Radial	Axial	Total	Core radius	Reflector thickness	Reflector savings	Critical height	Reflector thickness	Reflector savings
III-17	76.51	7.92	2.85	10.77	58.95	17.25[a]	26.5	164.6	5.0	21.5
III-18	75.51	≈8.57	≈3.47	≈12.04	58.95	17.25	23.2	≈148.0	≈21.6	≈20.6
III-19	75.51	8.93	3.11	12.04	55.91	20.29	24.6	157.5	12.1	20.6
III-20	73.77	9.43	4.78	14.21	55.89	20.31	22.4	122.6	47.0	21.1
III-21	73.77	10.40	3.93	14.33	50.76	25.44	23.8	≈139.0	≈30.6	≈19.5
III-22	73.77	8.54	5.55	14.09	61.98	14.22	20.3	110.8	58.8	22.6
III-23	73.77	11.06	≈3.15	≈14.21	48.26	27.94	24.1	≈158.0	≈11.6	≈19.0
III-24	69.68	14.53	4.07	18.60	41.60	34.61	21.5	137.2	32.4	18.5
IV-1	69.68	14.91	≈3.69	≈18.60	40.82	35.38	21.5	≈146.0	≈23.6	17.5
XVIII-A	72.1	8.76	5.99	14.75	61.11	15.09	20.1	107.9	45.5	20.4
XVIII-B	72.1	--	3.85	--	61.11	--	--	143.5	9.9	16.7
XVIII-C	72.1	--	6.61	--	61.11	--	--	101.9	51.5	20.3
XVIII-E	72.1	--	4.47	--	61.11	--	--	128.2	25.2	20.5
XVIII-F	72.1	--	3.76	--	61.11	--	--	144.6	8.8	17.5
XVIII-G	72.1	--	3.79	--	61.11	--	--	145.0	8.4	16.6

(a) Plus 5 inches of paraffin.

4.2.2. Reflector Savings Vs D_2O Concentration

From the preceding data, cases where the radial reflector thickness is essentially infinite, i.e., D_2O concentrations below about 70%, can be selected for comparison. Figure 4-4 shows the dependence of radial reflector savings on D_2O concentration for "infinite" reflector thickness. The data are not extensive enough to permit a similar comparison in the axial direction.

4.3. Flux in Reflector

Although most of the flux measurements were made only in the asymptotic region, some traverses extended into the radial reflector to provide additional data on D_2O-H_2O reflector effects. The flux measurements were made with bare and cadmium-covered gold foils, by the procedures described in Section 4.1.1, and the thermal component was obtained from the difference between the two normalized distributions. The results are shown in Figures 4-5 through 4-7, where the relative thermal flux is plotted against the core radius (in units of lattice pitches).

Figure 4-1. Buckling Vs D_2O Concentration (4.02%-Enriched UO_2)

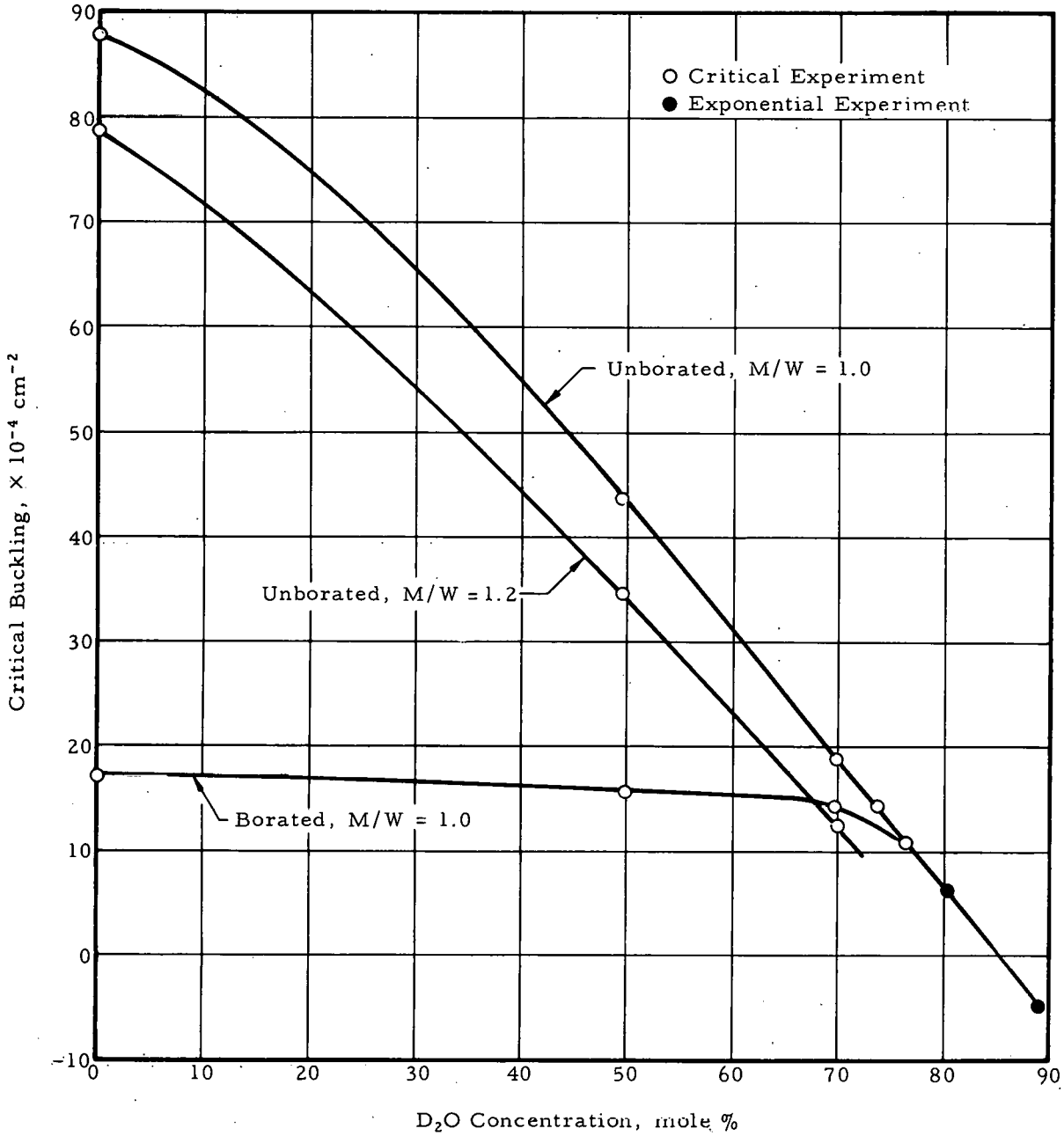

Figure 4-2. Buckling Vs D_2O Concentration (2.46%-Enriched UO_2)

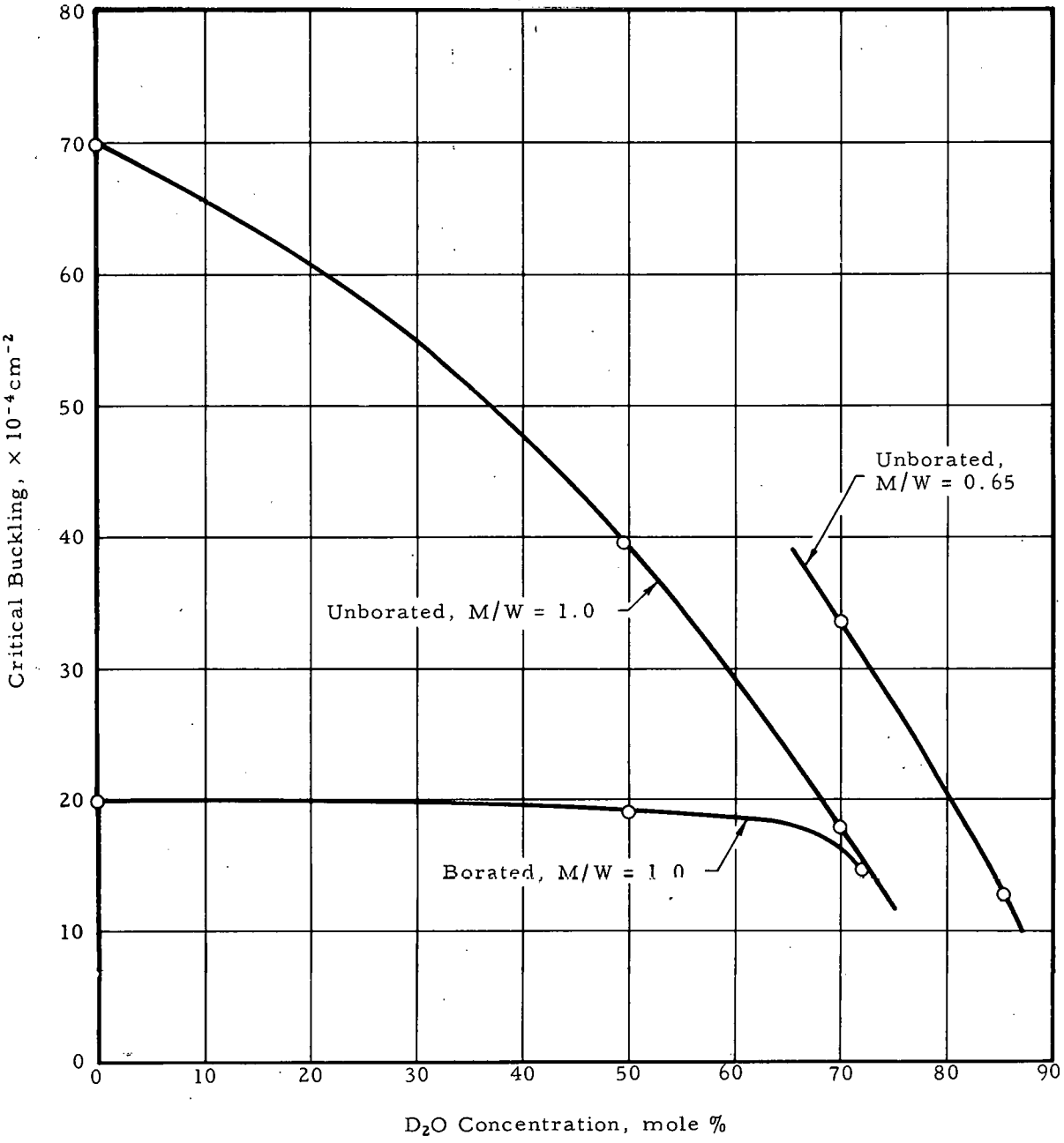

Figure 4-3. Reflector Savings Vs Reflector Thickness

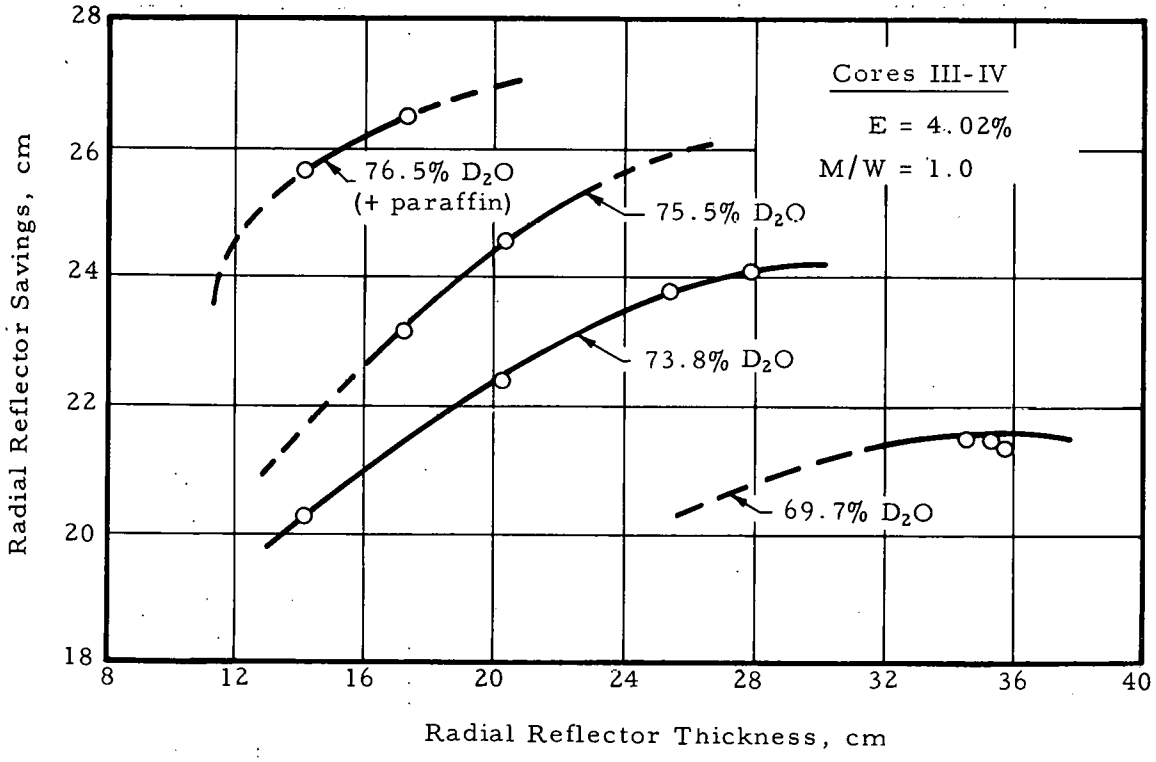

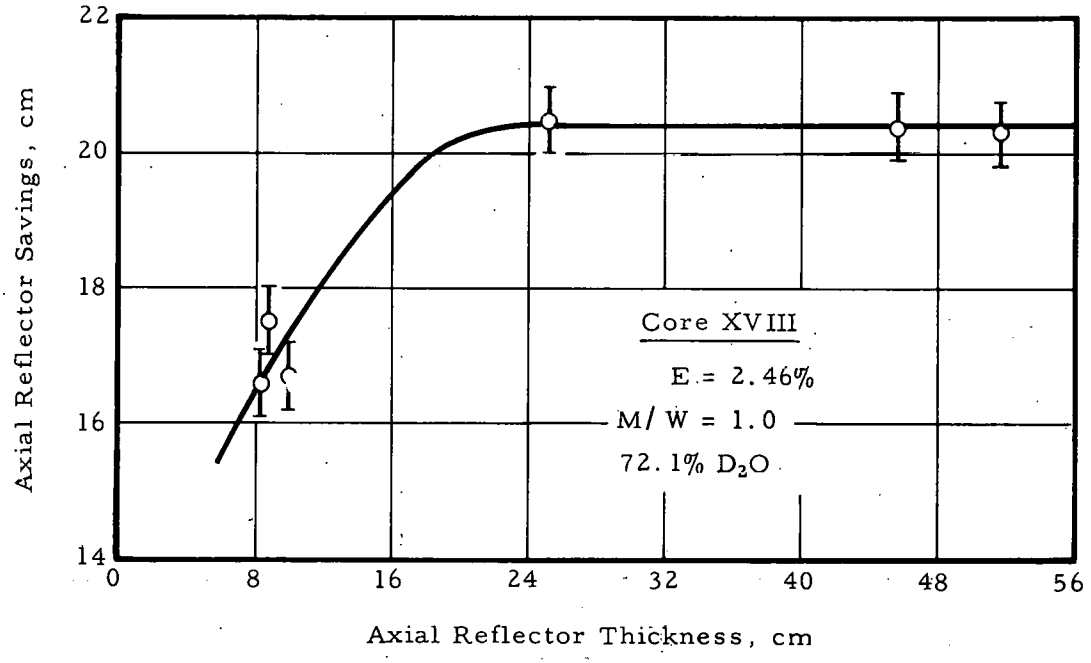

Figure 4-4. Reflector Savings Vs D_2O Concentration

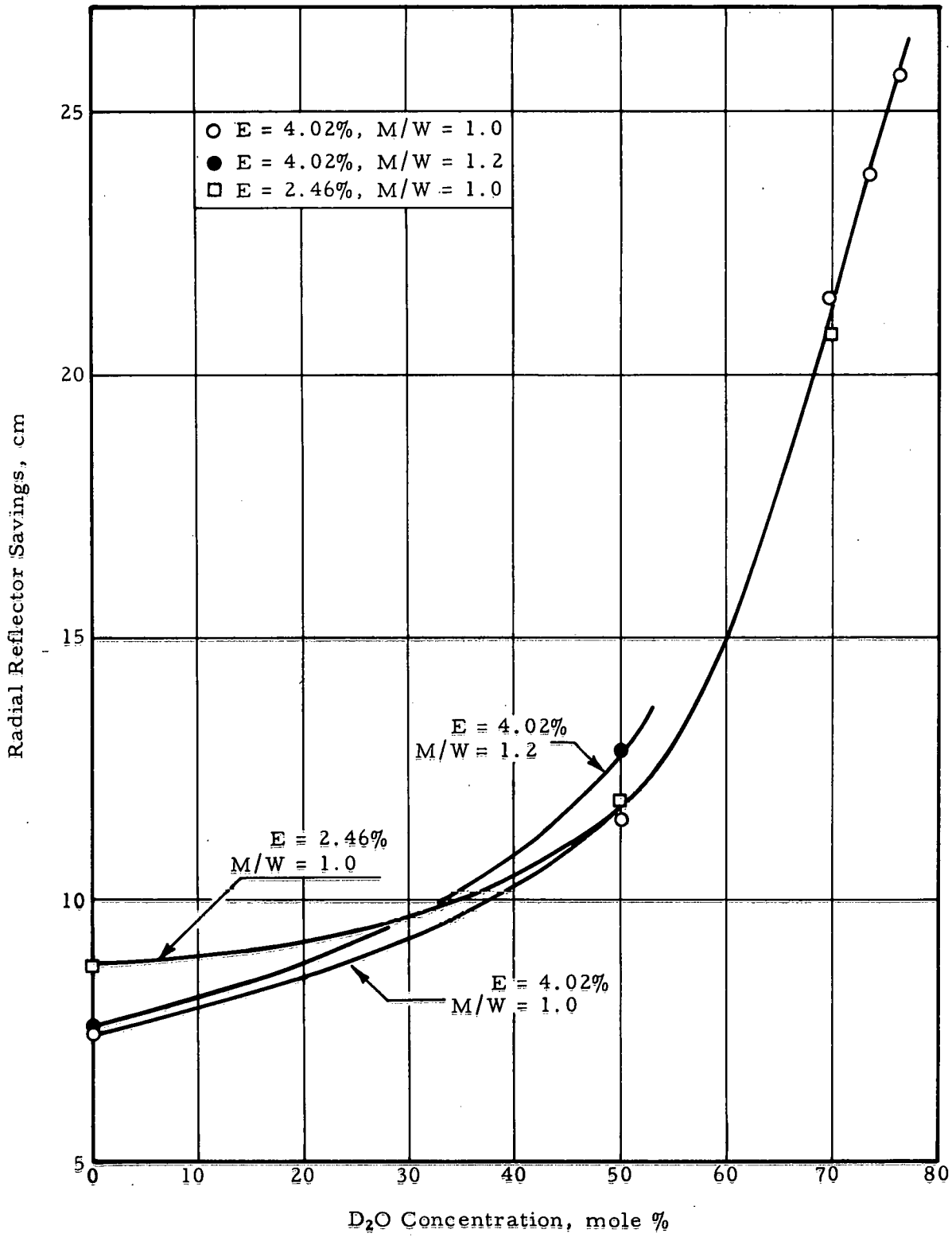

Figure 4-5. Thermal Flux in Reflector (Cores X-XII)

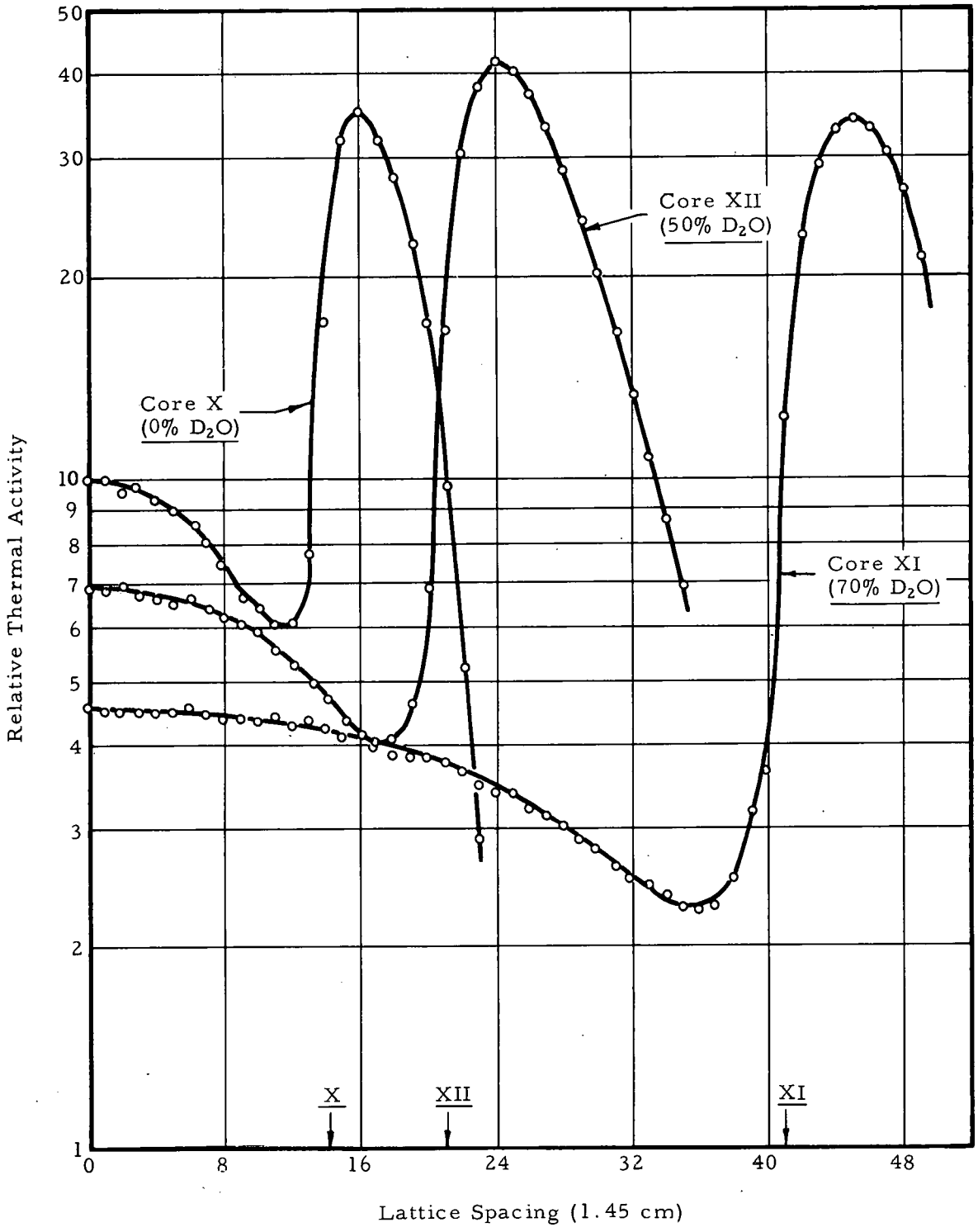

Figure 4-6. Thermal Flux in Reflector (Cores XIII-XV)

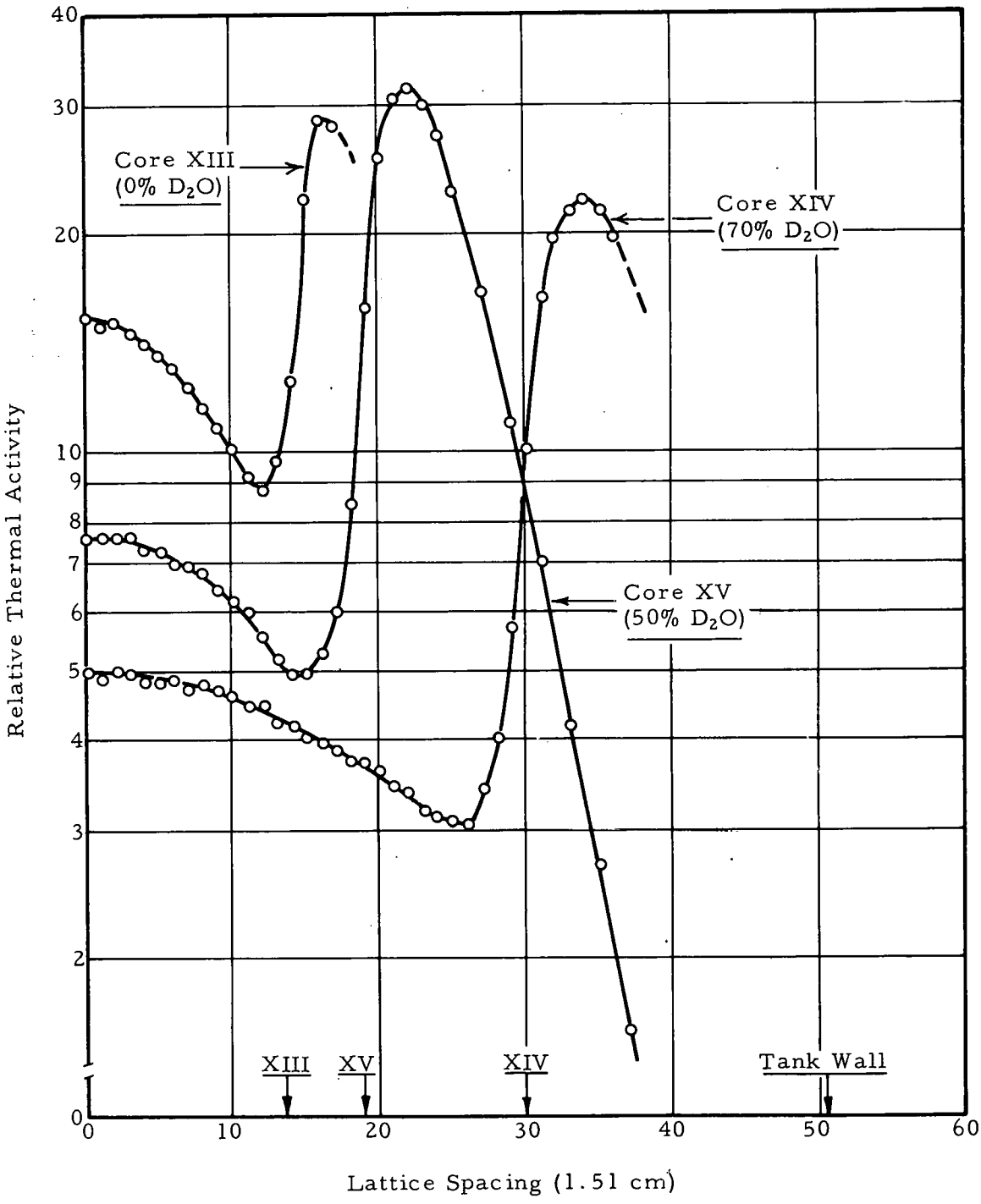

Figure 4-7. Thermal Flux in Reflector (Cores XVI, XVII)

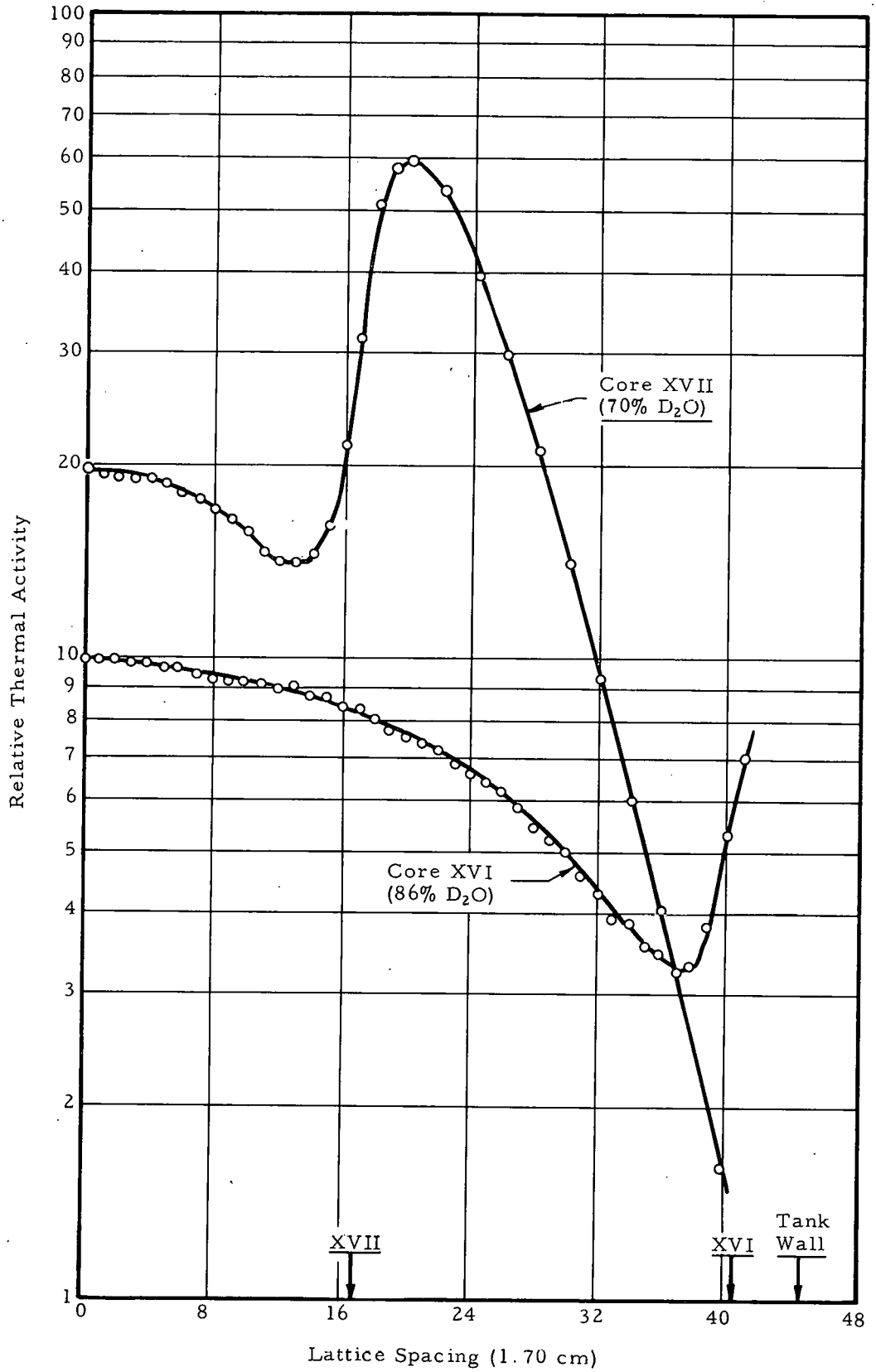

5. THERMAL DISADVANTAGE FACTOR

5.1. Techniques

The thermal disadvantage factor ($\overline{\phi}_m/\overline{\phi}_f$), defined as the ratio of the average thermal neutron flux in the moderator to that in the fuel in a unit cell, was measured with 0.007-inch thick sector foils of Dy-Al alloy (≈5 wt% Dy). Dysprosium was selected because it responds primarily to thermal neutrons, i.e., its cadmium ratio is high in these lattices. Therefore, the correction to the bare sector foil activity ratio for the difference in epithermal activity between the fuel and the moderator is small.

As shown in the plan view of Figure 5-1, the flux in the fuel was sampled with round (R) foils having the same diameter as the UO_2 in the fuel rod (d_f), and the flux in the moderator was sampled with scalloped (S) foils having a width p (one lattice pitch) across the flats. Note that the sector foils do not sample the flux in the cladding or in the thin gap (omitted from the figure for clarity) between the fuel pellets and the cladding (Methods B and C). The sector foils were located in the central lattice cell near the fuel midplane.

Three S-foils, supported on thin cotton thread laced around the fuel rods and separated axially by 5 cm, were simultaneously irradiated in each run. Three methods of loading the R-foils in the fuel were used during the program, as shown in Figure 5-1. In Method A, which was used in Cores I-IV, VI, and X-XII, a single R-foil was held between halves of a swaged 4.02%-enriched UO_2 fuel rod. The exposed ends were carefully faced in a lathe and sealed with 0.002-inch thick brass foils. The fuel rod diameter was reduced from 0.475 inch to 0.461 inch for a distance of 1/8 inch from each cut end, so that the fuel and Dy-Al foil could be accurately aligned within a 1/4-inch long, 0.475-inch OD, 0.007-inch wall stainless steel sleeve.

In Method B, which was used in Cores III-IX to improve the alignment between fuel and foil and to increase the amount of data per run,

three R-foils were sandwiched in a stack of eight 1/8-inch thick UO_2 wafers having the same enrichment, density, and diameter as the 4.02%-enriched fuel in the swaged fuel rods. The Dy-Al foils were covered on each side with 0.0005-inch thick aluminum foils and were separated by two wafers. The wafers were loaded inside a 1-inch long section of a fuel rod from which the UO_2 had been removed. Method C was used for all 2.46%-enriched cores. Since this fuel was pelletized, R-foils (covered with 0.0005-inch thick aluminum) were simply loaded in a standard fuel rod and separated by single UO_2 pellets.

Corrections for epithermal activity in the bare sector foils were obtained by measuring Dy-Al cadmium ratios in the fuel and moderator. Cadmium-covered activities were measured in the moderator by activating R-foils in 0.020-inch wall cadmium pillboxes aligned parallel to the fuel rods and in the fuel by activating R-foils covered with 0.020-inch thick cadmium as shown in Figures 6-1 and 6-2 in the next section. The bare and cadmium-covered runs were normalized by at least three gold or Dy-Al monitor foils.

The R and S sector foils were simultaneously activated for 20 minutes at power levels in the range of 2 to 50 watts with all control blades withdrawn. After a delay of at least one hour for the short-lived aluminum activity to decay, the foils were counted in a 4π gas-flow proportional counter. In Cores V-VII, an end-window gas-flow proportional counter was used, but comparative 2π and 4π counts in other cores showed no significant difference after the appropriate foil calibration factors were applied. Count rates varied from 10,000 to 50,000 counts/min, and each foil was counted enough times to accumulate at least 100,000 counts.

Since the dysprosium content of the Dy-Al foils varied, foil calibration factors were obtained by irradiating sets of foils on a wheel rotating in a region of constant flux and by counting them in the same 4π (or 2π) counters.

5.2. Results

The results of the thermal disadvantage factor measurements are summarized in Table 5-1 and compared in Figure 5-2. $\overline{A}_m/\overline{A}_f$ is the ratio of bare foil saturated activities, corrected for variations in dysprosium content and the axial position of the S-foils. Each value is the

unweighted average of at least six measurements (except four in Core II). The uncertainty is the larger of the internal and external standard deviations of the mean; systematic errors are discussed in the next section.

The thermal disadvantage factor was obtained by multiplying the bare foil activity ratio by an epithermal correction factor, as shown below.

$$\frac{\overline{\phi}_m}{\overline{\phi}_f} = \frac{\overline{A}_m}{\overline{A}_f} \left(\frac{C_m - 1}{C_m}\right) \left(\frac{C_f}{C_f - 1}\right)$$

In this expression, C_m and C_f are the cadmium ratios of Dy-Al in the moderator and in the fuel. As shown in the lower curves of Figure 5-2, the epithermal correction factor is close to unity and increases monotonically with lattice epithermality. Some of the early[3] cadmium-covered measurements (E = 4.02%, M/W = 1.0) appeared to be in error, so the correction factors for these cases were taken from the smooth curve.

5.3. Discussion

Several potential sources of systematic error were considered. Although 4π counting was used in most of the cores, the foils were 2π counted in several cases. Comparative measurements by both 4π and 2π counting gave equivalent results providing the foil factors were measured in the same counting geometry. Methods A and B were compared in three cores and were found to agree within combined standard deviations.

Measurements of the Dy-Al cadmium ratios in the moderator and fuel may be subject to fairly large errors due to cadmium effects. The cadmium ratio in the moderator was obtained by comparing the bare activity of an S-foil to the cadmium-covered activity of an R-foil. Since the R-foil does not sample the entire moderator region (and is oriented perpendicular to the S-foil), the validity of this measurement rests on the assumption that the epithermal flux is relatively flat across the moderator. The cadmium-covered measurement in the fuel by Method B may also be in error due to neutron thermalization in the oxide (see Section 6.3.1). Fortunately, the cadmium ratios are large enough to make the epithermal correction factors close to unity, and appreciable errors in C_m and C_f can be tolerated.

The primary advantage of dysprosium for thermal disadvantage factor measurements is that it responds primarily to thermal neutrons, i.e., its cadmium ratio is so high that errors in the epithermal correction are almost negligible. However, the activation cross section of dysprosium is not exactly 1/v. To check for gross errors due to non-1/v behavior, comparative measurements were made in Core VIII[3] with Dy-Al, gold, and 93%-enriched U-Al alloy (18 wt% U) sector foils. All three results agreed within combined standard deviations, although the test is not conclusive because of the relatively large uncertainty in the epithermal correction for gold and U-Al. This occurs because the cadmium ratios of these materials are much smaller than for Dy-Al.

Table 5-1. Thermal Disadvantage Factor

Core no.	Fuel, wt% U^{235}	M/W ratio	Moderator composition		$\bar{A}_m/\bar{A}_f$	C_m	C_f	Epithermal correction factor	$\bar{\phi}_m/\bar{\phi}_f$
			D_2O, mole %	Boron, gm B/ℓ					
I	4.02	1.006	0.0	0	1.24 ± 0.02	--	--	(1.006)	1.25 ± 0.02
II	4.02	1.006	0.0	3.39	1.24 ± 0.03	--	--	(1.006)	1.25 ± 0.03
III	4.02	1.006	76.5	0	1.15 ± 0.02	7.70	6.92	1.017	1.17 ± 0.02
IV	4.02	1.006	69.7	0	1.15 ± 0.02	8.94	8.23	1.011	1.16 ± 0.02
V	4.02	1.006	69.7	0.422	1.12 ± 0.02	--	--	(1.011)	1.13 ± 0.02
VI	4.02	1.006	49.6	1.79	1.18 ± 0.02	--	--	(1.012)	1.19 ± 0.02
VII-B	4.02	1.006	81.2	0	1.11 ± 0.02	--	--	(1.015)	1.13 ± 0.02
IX	4.02	1.006	49.7	0	1.16 ± 0.01	--	--	(1.012)	1.17 ± 0.02
X	4.02	1.195	0.0	0	1.227 ± 0.007	17.2	14.8	1.010	1.239 ± 0.007
XI	4.02	1.195	70.1	0	1.156 ± 0.006	7.20	6.41	1.020	1.179 ± 0.009
XII	4.02	1.195	49.7	0	1.177 ± 0.006	10.4	9.11	1.015	1.195 ± 0.007
XIII	2.46	1.001	0.0	0	1.186 ± 0.007	32.3	28.7	1.004	1.191 ± 0.007
XIV	2.46	1.001	70.0	0	1.138 ± 0.005	14.0	12.6	1.008	1.147 ± 0.005
XV	2.46	1.001	49.8	0	1.148 ± 0.005	20.1	18.0	1.007	1.156 ± 0.005
XVI	2.46	0.651	85.5	0	1.137 ± 0.004	15.1	14.1	1.005	1.143 ± 0.005
XVII	2.46	0.651	70.0	0	1.164 ± 0.004	20.3	18.6	1.005	1.170 ± 0.005

Figure 5-1. Disadvantage Factor Loading Arrangement

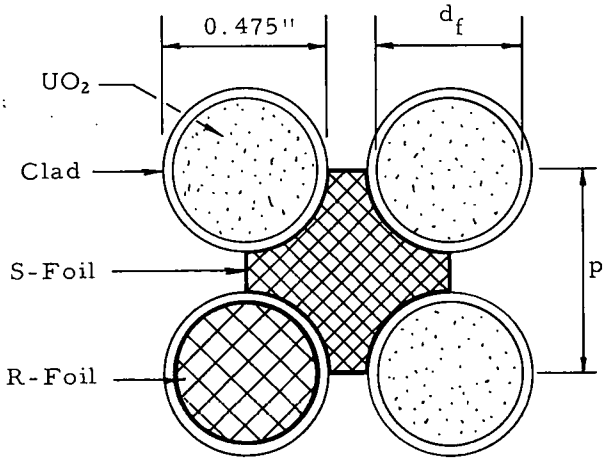

Plan View

Core numbers	p, in.	d_f, in.
I - IX	0.595	0.444
X - XII	0.571	0.444
XIII - XV	0.595	0.406
XVI - XVII	0.670	0.406

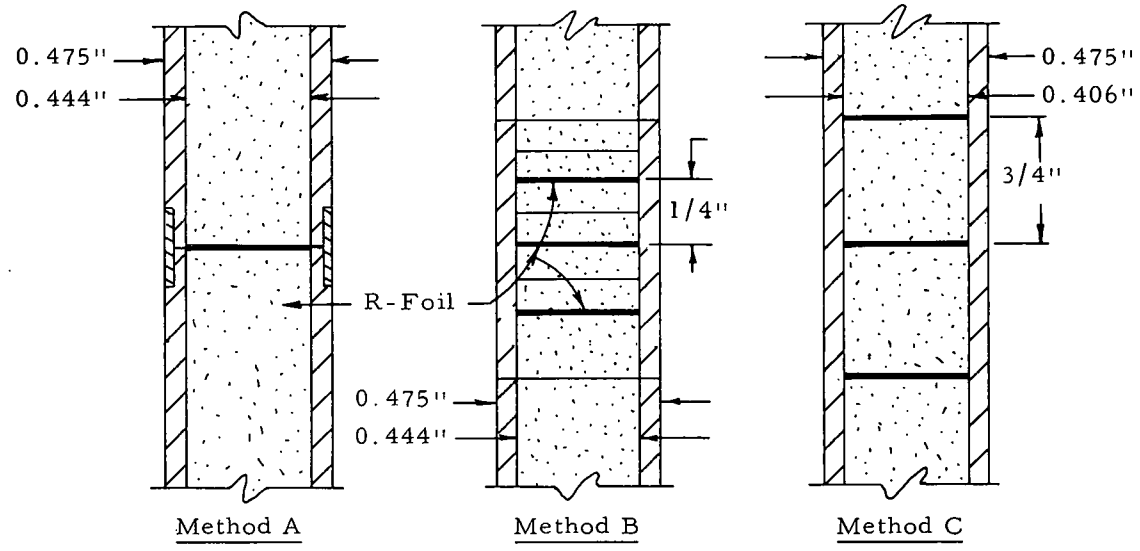

Elevation View

Figure 5-2. Thermal Disadvantage Factor

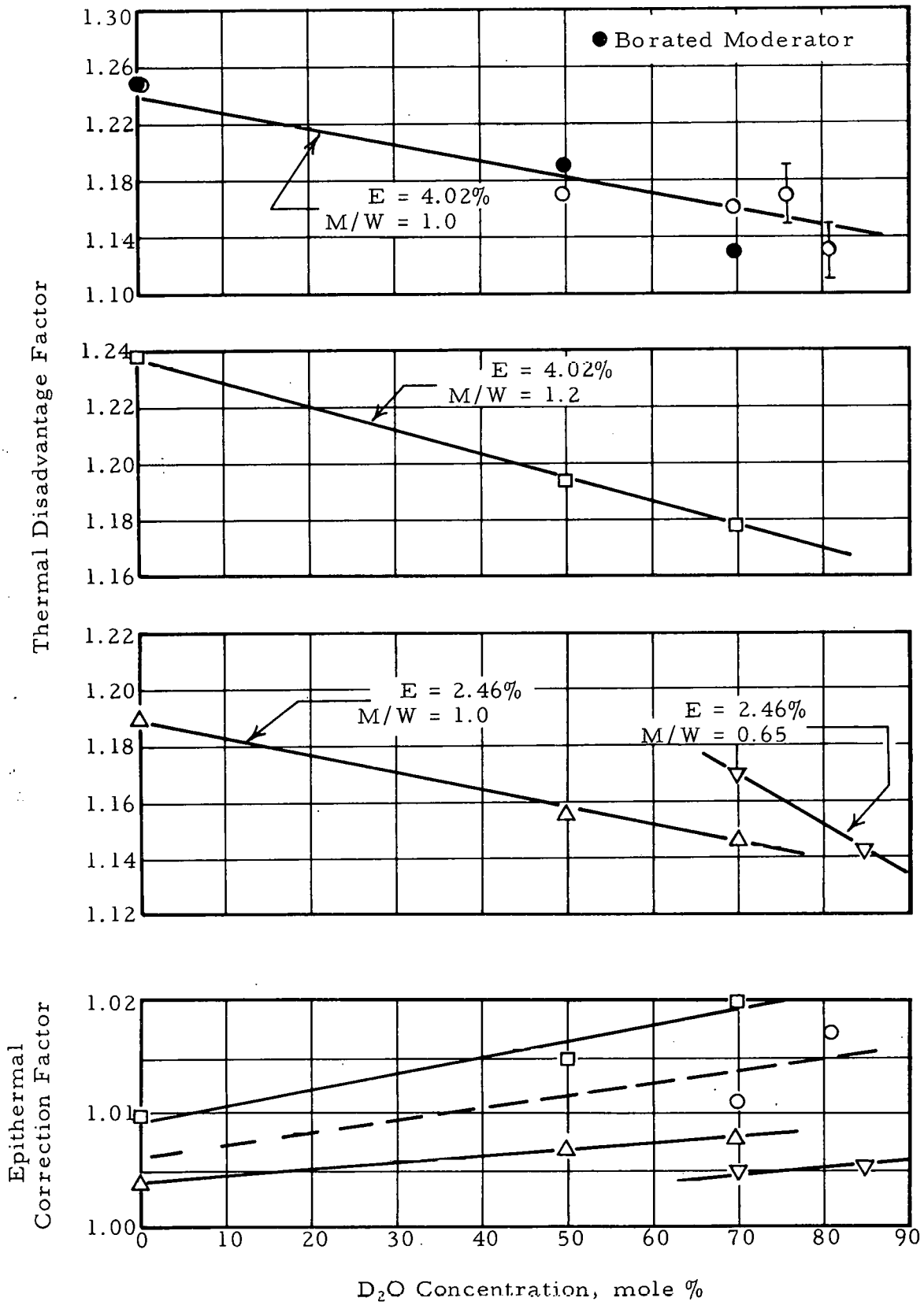

6. CADMIUM RATIO OF U^{235}

6.1. Techniques

The fission cadmium ratio of U^{235} was measured in each of the major cores with bare and cadmium-covered foils of 93%-enriched U-Al alloy containing about 18 wt% uranium. The foils were covered on each side with 0.0005-inch thick aluminum, removed before counting, to prevent fission recoil contamination. Usually the U-Al foils were 0.010 inch thick, although comparative measurements were made in some of the cores with 0.002-inch thick foils to show that self-shielding effects were negligible. The foil diameter was equal to the fuel diameter, 0.444 inch for the 4.02%-enriched UO_2 and 0.406 inch for the 2.46%-enriched UO_2.

The measurements were made in the central fuel rod, approximately 5 cm below the fuel midplane, where the spectrum was asymptotic. The foil loading arrangement changed during the program, as techniques were refined, and varied with the type of fuel as shown in Figures 6-1 and 6-2. The thin gap between the pellets and cladding in Method D of Figure 6-2 is omitted for clarity. In Method A, a standard swaged 4.02%-enriched UO_2 fuel rod was carefully cut in half, and the exposed ends were faced in a lathe and sealed with 0.002-inch thick brass foils. The fuel rod diameter was reduced from 0.475 inch to 0.461 inch for a distance of 1/8 inch from each cut end so that the fuel and U-Al foil could be aligned within a 1/4-inch long, 0.475-inch OD, 0.007-inch wall stainless steel sleeve. In the corresponding cadmium-covered runs, the U-Al foil was covered by two 0.444-inch diameter by 0.020-inch thick cadmium discs, and the stainless steel sleeve was replaced by a 1/8-inch long, 0.484-inch OD, 0.020-inch wall cadmium sleeve. The cadmium sleeve was machined on the inside to reduce the wall thickness to 0.011 inch except for a 0.050-inch long section in the center.

In Method B, three U-Al foils were placed between 0.25-inch long sections cut from a standard 4.02%-enriched UO_2 fuel rod. The cut sections were faced in a lathe and coated with a thin layer of Krylon. In the bare runs, the sections were aligned and sealed by wrapping two layers of 0.003-inch thick polyester film tape around them. In the cadmium-covered runs, the fuel sections and U-Al foils were completely enclosed in a 0.020-inch wall cadmium cylinder formed by a 5/8-inch long by 0.475-inch ID sleeve with 0.444-inch diameter discs at the ends.

In Method C, three U-Al foils were sandwiched in a stack of eight 1/8-inch thick UO_2 wafers having the same enrichment, diameter, and density as the 4.02%-enriched fuel in the standard swaged fuel rods. The U-Al foils were separated by one (Cores III-V) or two (Cores VI-IX) wafers. In the cadmium-covered runs, the wafers were stacked in a 1-inch long by 0.020-inch wall cadmium sleeve having the same ID as the fuel and covered at the ends by 0.444-inch diameter by 0.020-inch thick cadmium discs.

Method D was used for the 2.46%-enriched cores. Since this fuel was pelletized, the U-Al foils were placed between 3/4-inch long UO_2 pellets and loaded in a standard fuel rod. In the cadmium-covered runs, each U-Al foil was covered with 0.020-inch thick cadmium discs and a 0.055-inch long, 0.020-inch wall, 0.406-inch ID cadmium sleeve. The cadmium sleeves were held in position by short lengths of aluminum sleeves that fitted in a recess machined on the inside of the aluminum clad. All joints were wrapped with several layers of 0.004-inch thick Mylar tape to keep them waterproof.

The foils were irradiated for 20 minutes at power levels between 10 and 100 watts with all control blades withdrawn. Bare and cadmium-covered runs were normalized by simultaneously irradiating at least three bare U-Al monitor foils located in reproducible positions in the lattice. After a downtime of at least 30 minutes, the data and monitor foils were gamma counted in a sodium iodide scintillation spectrometer biased to count photons above 200 kev. The foils in comparable bare and cadmium-covered runs were counted in the same sequence and after the same delay times. Normally, five 1-minute counts were taken on each foil, and count rates were never less than about 20,000 counts/min. To eliminate calibration errors, the same U-Al foils were used in pairs

of bare and cadmium-covered runs. Foil backgrounds were counted prior to irradiation and were usually about 2000 counts/min.

The ratio of bare to cadmium-covered data foil activity was computed at each counting time, and the ratios were averaged. The same procedure was followed for each U-Al monitor foil. These ratios did not appear to vary systematically with time. The cadmium ratio was then obtained by dividing the average data foil activity ratio by the average monitor activity foil ratio.

6.2. Results

The results of the measurements are summarized in Table 6-1 and in Figure 6-3. The ratio of epithermal to thermal fissions δ_{25} is derived from the fission cadmium ratio C_{25} using the usual expression, $\delta_{25} = (C_{25} - 1)^{-1}$. The results of exponential experiments at higher D_2O concentrations[4] are also listed for comparison. Each value is the unweighted average of at least six separate determinations obtained from three or more pairs of runs. The uncertainty is the larger of the internal and external standard deviations of the mean. Systematic errors are discussed in the next section.

The method listed in Table 6-1 refers to the alternate loading arrangements of U-Al foils illustrated in Figures 6-1 and 6-2. As discussed in the next section, the results by Method C are subject to a small neutron thermalization error, so the values listed in the table have been corrected for this effect. The results for Core I, which were obtained by surrounding the cut fuel rod with a 2-inch long cadmium sleeve, have been corrected in the same manner.

6.3. Discussion

During the course of the program, the precision of the U^{235} cadmium ratio measurements was improved to the point where systematic errors of the order of 1% could be investigated. Only one systematic error of this magnitude could be found in these measurements—neutron thermalization. The results listed in Table 6-1 have been corrected for this effect where appropriate, and the uncertainties have been increased accordingly. Other systematic errors in the data are probably less than 1% based on the measurements described in the following section.

Table 6-1. Cadmium Ratio of U^{235}

Core no.	Fuel, wt% U^{235}	M/W ratio	Moderator composition		Cadmium ratio of U^{235}	δ_{25}	Method
			D_2O, mole %	Boron, gm B/ℓ			
I	4.02	1.006	0.0	0	4.95 ± 0.10	0.253 ± 0.006	--
III	4.02	1.006	76.5	0	2.17 ± 0.03	0.855 ± 0.022	C
IV	4.02	1.006	69.7	0	2.43 ± 0.02	0.699 ± 0.010	A
V	4.02	1.006	69.7	0.422	2.32 ± 0.02	0.758 ± 0.012	C
VI	4.02	1.006	49.6	1.79	2.87 ± 0.03	0.535 ± 0.009	C
VII-B	4.02	1.006	81.2	0	1.94 ± 0.02	1.064 ± 0.023	C
IX	4.02	1.006	49.7	0	3.09 ± 0.03	0.478 ± 0.007	C
X	4.02	1.195	0.0	0	4.26 ± 0.02	0.307 ± 0.002	A & B
XI	4.02	1.195	70.1	0	2.12 ± 0.01	0.893 ± 0.008	A & B
XII	4.02	1.195	49.7	0	2.74 ± 0.02	0.575 ± 0.007	A & B
XIII	2.46	1.001	0.0	0	7.63 ± 0.03	0.151 ± 0.001	D
XIV	2.46	1.001	70.0	0	3.55 ± 0.02	0.392 ± 0.003	D
XV	2.46	1.001	49.8	0	4.79 ± 0.02	0.264 ± 0.001	D
XVI	2.46	0.651	85.5	0	3.51 ± 0.04	0.398 ± 0.006	D
XVII	2.46	0.651	70.0	0	4.95 ± 0.02	0.253 ± 0.001	D
--[a]	4.02	1.006	89.1	0	1.65 ± 0.02	1.54 ± 0.05	C
--[a]	4.02	1.006	80.7	0	2.00 ± 0.02	1.00 ± 0.02	C

[a] Exponential experiment.

6.3.1. Neutron Thermalization

The U^{235} cadmium ratio is defined as the ratio of total fissions (in U^{235}) to fissions produced by neutrons above the cadmium cutoff energy ($\approx$ 0.4 ev). If an appreciable quantity of fuel (UO_2) exists between the cadmium and the U-Al foil, neutrons entering the fuel sample above 0.4 ev can, by elastic collisions with oxygen, be degraded to lower energies. Thus, the cadmium-covered activity would include both epicadmium fissions and a small component of fissions at lower energies, and the measured cadmium ratio would be too low.

Thermalization was studied in Cores X through XII by comparing cadmium ratio measurements by Methods A and B. The cadmium ratio C_1 obtained by the single foil technique (Method A) should be free from thermalization since there was no oxide between the cadmium and the U-Al foil. C_2 and C_3 are the cadmium ratios obtained from the multiple foil technique (Method B). However, the central foil value C_3 should be subject to neutron thermalization, and C_2, the average of the top and bottom foils, should be affected by thermalized neutrons on one side. The measured cadmium ratios are defined as

$$C_1 = \frac{Th + T + E}{E}$$

$$C_3 = \frac{Th + T + E}{T + E}$$

where E is the epicadmium activity, Th + T is the subcadmium activity, and T is the activity from neutrons which enter the fuel above 0.4 ev but produce fissions at a lower energy. The equations are solved to yield

$$\frac{T}{E} = \frac{C_1}{C_3} - 1$$

$$\frac{T}{Th} = \left(\frac{C_1 - 1}{C_1}\right)\left(\frac{C_3}{C_3 - 1}\right) - 1$$

The experimental results are given in Table 6-2 and Figure 6-4. If thermalization is responsible for the difference between C_1 and C_3, then the ratio T/Th should remain approximately constant as

the D_2O concentration changes. This assumes that T is proportional to the slowing-down density in the lattice just above the cadmium cutoff, and because most of the thermal absorptions are in fuel, Th is also proportional to the slowing-down density. Within their accuracy, the data support the hypothesis.

Table 6-2. Effect of Neutron Thermalization

Symbol	Method	Core X 0% D_2O	Core XII 49.7% D_2O	Core XI 70.1% D_2O
C_1	A—Single foil	4.26 ± 0.02	2.74 ± 0.02	2.12 ± 0.01
C_2	B—End foils	4.18	2.72	2.11
C_3	B—Middle foil	4.07	2.68	2.10
T/E		0.047	0.022	0.010
T/Th		0.014 ± 0.003	0.013 ± 0.005	0.009 ± 0.005

Since the results by Method A should be free from thermalization and are reasonably consistent with Method B when thermalization is taken into account, the Method A values are retained in Table 6-1 without correction. Likewise, the measurements by Method D require no thermalization correction. However, a small correction is required in the early measurement by Method C (and in Core I). Since the parameter T/Th should be fairly constant in all of these cores, the cadmium ratios by Method C have been corrected in Table 6-1 on the assumption that T/Th = 0.010 ± 0.005. This value is consistent with the data of Table 6-2 and with the result (≈ 0.015) of a similar comparison in another light water lattice[21].

6.3.2. Other Systematic Errors

Self-shielding effects in the 0.010-inch thick U-Al foils were estimated in Cores III and IV by repeating measurements with 0.002-inch thick foils. The change in apparent cadmium ratio was less than 1%. In some of the loading arrangements, particularly in Method B, the cadmium displaced a slight amount of moderator around the fuel rod. The effect on Dancoff shielding was studied in Core IV by comparing

cadmium ratios by Method C (negligible displacement) and an alternate of Method C, in which the cadmium sleeve displaced more moderator. In the alternate loading the diameter of the cadmium sleeve was enlarged to fit around the stainless steel clad. No difference was observed within the accuracy of the measurements, ± 1%.

Neutron streaming through the 0.020-inch thick cadmium discs adjacent to the U-Al foils was investigated[15] in Cores XIII and XV by placing 0.020-inch thick aluminum or lead discs between the cadmium and the U-Al foil. The cadmium-covered activity was increased by slightly less than 1%, but no correction was applied because of the difficulty of extrapolating the results to streaming in cadmium alone. The upper limit is, however, within the range of the errors quoted in the measurements.

Other small systematic errors having upper limits in the range of 0.5 to 1% were found during the program. They include non-uniformities in the density (and perhaps enrichment) of the UO_2, mismatch between fuel and U-Al foil diameters, and compositional and dimensional differences in the U-Al foils.

Figure 6-1. C_{25} Loading Arrangement (Methods A, B)

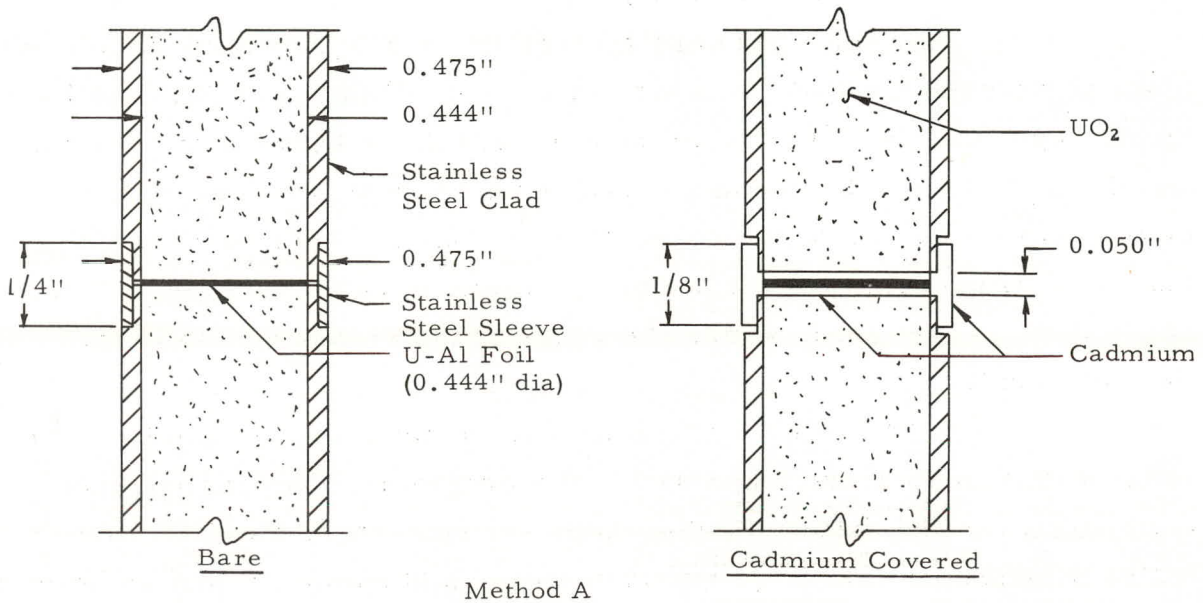

Method A

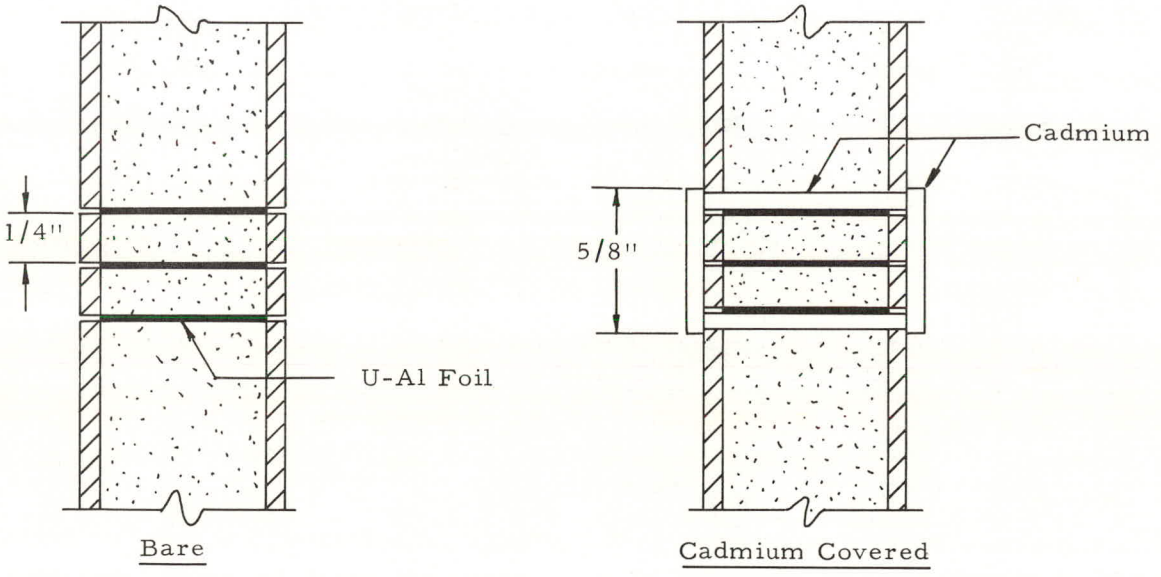

Method B

Figure 6-2. C_{25} Loading Arrangement (Methods C, D)

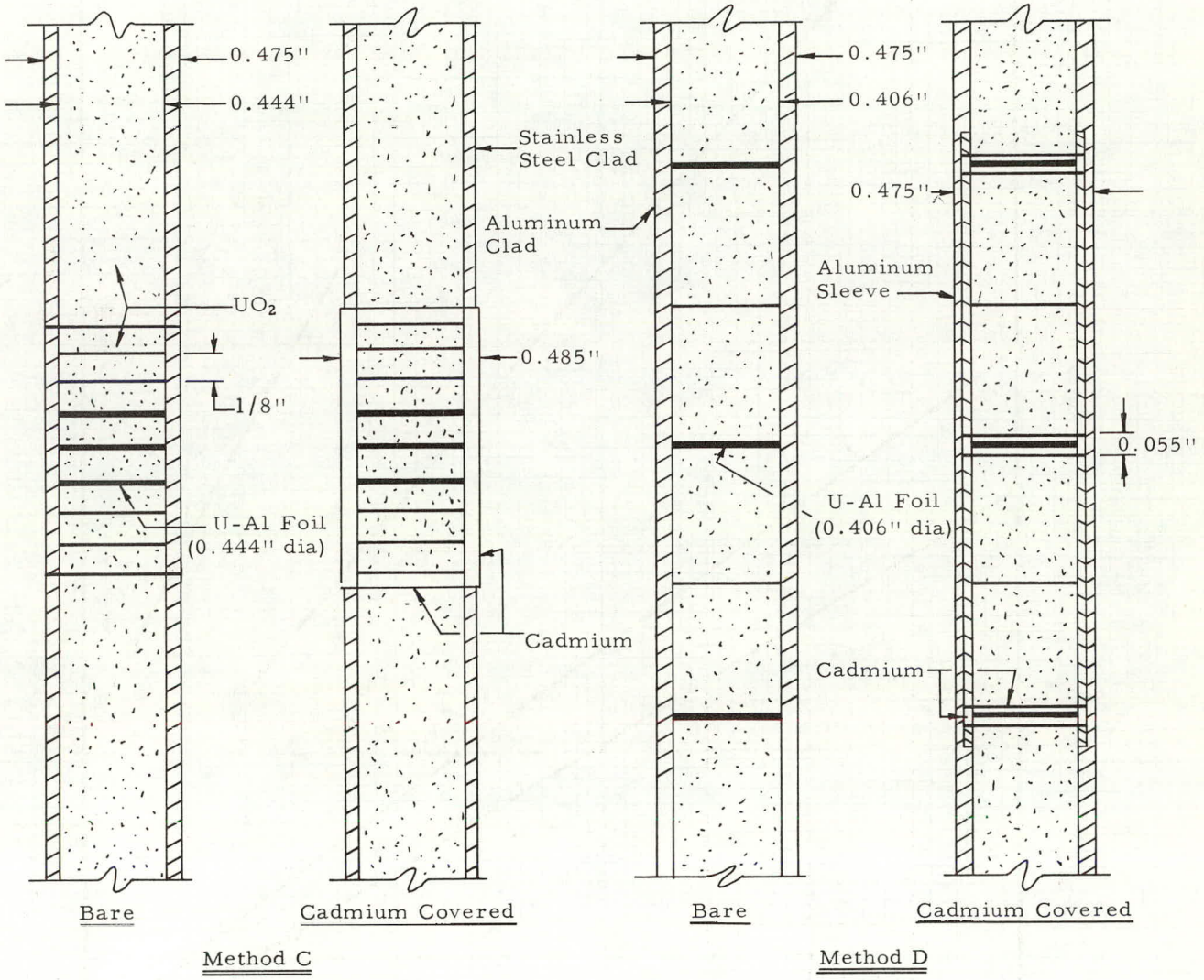

Figure 6-3. Cadmium Ratio of U^{235}

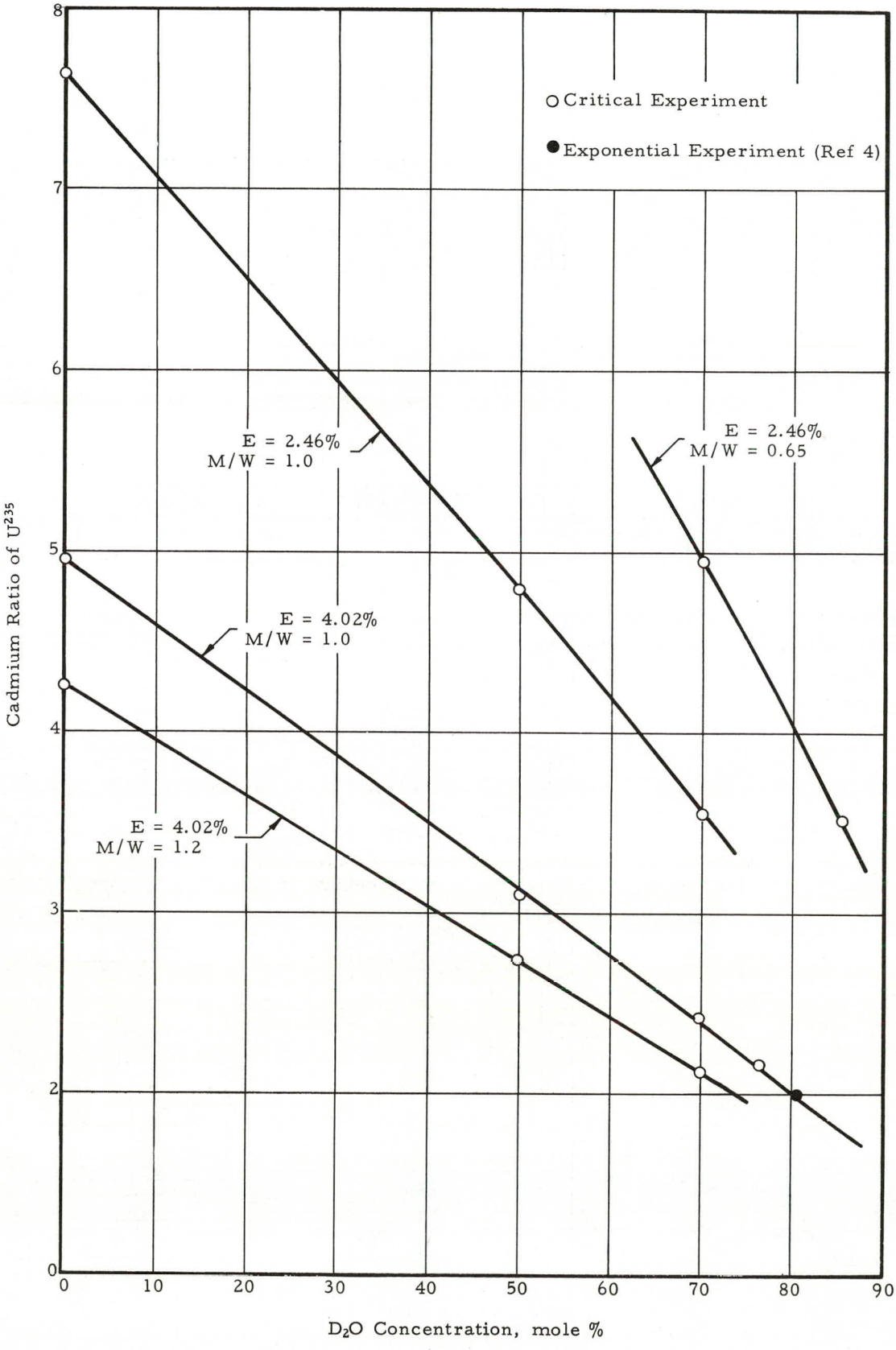

Figure 6-4. Effect of Neutron Thermalization

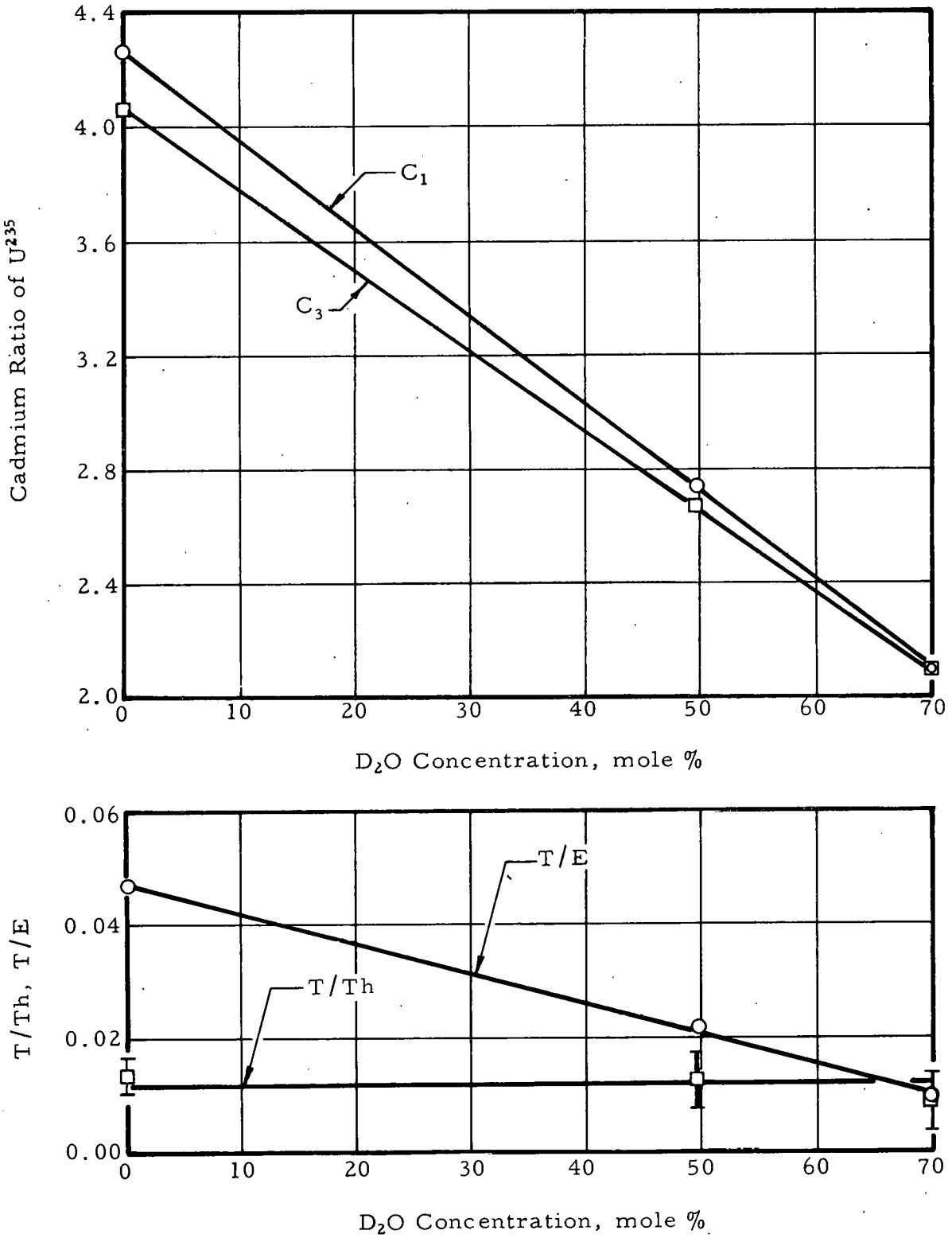

7. CADMIUM RATIO OF U^{238}

7.1. Techniques

7.1.1. Introduction

The U^{238} cadmium ratio C_{28} was measured in each of the major cores by the thermal activation technique, which is described in detail in Reference 22. This technique has three advantages over standard methods:

1. By comparing total U^{238} absorptions to absorptions in an intermediate foil responding primarily to thermal neutrons, $C_{28} - 1$ (or ρ_{28}) is measured directly. A direct measurement is particularly useful in epithermal lattices where C_{28} is very close to unity.

2. U^{238} absorptions are measured by activating the fuel itself, chemically removing fission product and other interfering activity, and counting U^{239}. In this manner, many of the errors inherent in the use of conventional depleted-uranium foil techniques are avoided.

3. The cadmium-covered U^{238} measurement is eliminated, so that the effects of cadmium perturbations are minimized.

The working equation, derived in the referenced report, is

$$\frac{C_{28}-1}{C_{28}} \equiv \frac{1}{1+\rho_{28}} = \left(\frac{A_X^B}{A_U^B}\right)_R \left(\frac{C_X - 1}{C_X}\right)_R \Phi K \qquad (7\text{-}1)$$

where A is the weight-normalized saturated activity, the superscript B refers to a bare irradiation, and the subscripts U and X refer to uranium and the intermediate material, usually dysprosium. The R-parameters are those measured in the critical experiment lattice. The calibration factor

$$\Phi = \left(\frac{A_U^{'B}}{A_X^{'B}}\right)_{\phi} \left(\frac{C_U - 1}{C_U}\right)_{\phi} \left(\frac{C_X}{C_X - 1}\right)_{\phi} \qquad (7\text{-}2)$$

is measured in a separate irradiation in a well-thermalized neutron flux denoted by ϕ. K is a small, calculated correction for the non-1/v behavior of dysprosium in the R- and ϕ-irradiations.

7.1.2. Lattice Irradiation

The geometry for the R-irradiations in the critical experiment lattices varied slightly, depending on the type of fuel rod. Irradiation samples of the 4.02% fuel were prepared by cutting standard swaged fuel rods into a number of short sections having accurately machined faces. As shown in Figure 7-1, the data slugs usually were 0.5-inch long with 0.25-inch long guard slugs at each end to facilitate alignment. In the first experiment (Core III), however, the data slugs were 2.5 inches long, and no guard slugs were used; in Cores I and IX the data and guard slugs were 1 inch and 0.5 inch long, respectively. The fuel slugs were accurately positioned in the lattice between cut and sealed ends of a standard fuel rod, and the joints were wrapped with two layers of 0.002-inch thick Mylar tape to preserve the alignment and to keep the joints watertight.

The loading arrangement for the pelletized 2.46% fuel is shown in Figure 7-2. In this case, the data slugs were 3/4-inch long UO_2 pellets centered in a standard fuel rod with intermediate foils on each side.

The intermediate foils were usually 0.007-inch thick Dy-Al foils ($\approx$ 4 wt% Dy) having the same diameter as the fuel, i.e., 0.444 inch for the 4.02% fuel and 0.406 inch for the 2.46% fuel. A few measurements were repeated with copper as the intermediate material to check the validity of the non-1/v correction for dysprosium. These foils were 0.004-inch thick metallic copper having the same diameter as the fuel. The intermediate foils were protected from fission recoil contamination by covering them on each side with 0.0005-inch thick aluminum foil.

The geometry for the cadmium-covered irradiation is also shown in Figures 7-1 and 7-2. The fuel slug and intermediate foils

were completely enclosed by a 0.020-inch wall cadmium sleeve covered at the ends with 0.020-inch thick cadmium discs having the same diameter as the ID of the sleeve. In some experiments, cadmium perturbations were studied by shortening the length of the fuel slugs and cadmium sleeves. Since the cadmium-covered irradiation is required only for the measurement of C_X, the cadmium-covered uranium activity was usually not measured. Bare and cadmium-covered runs were normalized by at least four gold monitor foils positioned in the core about 8 inches away from the fuel slug. The irradiations were performed at power levels between 500 and 1000 watts, for a period of 20 minutes, with all control blades withdrawn to avoid flux perturbations.

7.1.3. Chemical Processing and Counting

After reactor shutdown, the irradiated fuel slug was removed from the critical experiment lattice, and the UO_2 was dissolved in hot, concentrated nitric acid. Fission product and other interfering activity was removed by several stages of tributyl phosphate solvent extraction, and ammonium diuranate was then precipitated and centrifuged on superpure (99.999%) aluminum counting planchets.

Within 60 minutes of reactor shutdown, the U^{239} activity on the aluminum planchet was beta counted in end-window gas-flow proportional counters. Each planchet was counted at least five times for one minute in each of three counters, and count rates varied from 100,000 to a minimum of 10,000 counts/min. Background corrections, principally from Np^{239}, were measured by counting each planchet for 10 minutes after 900 minutes decay; the corrections never exceeded 1%. The effectiveness of these procedures was confirmed by obtaining the correct U^{239} half-life over a period of at least eight half-lives.

The Dy-Al (or Cu) intermediate foils were also beta counted in the same counters. Count rates were at least as high as for the uranium samples, except for cadmium-covered Dy-Al foils, where count rates were between 5,000 and 10,000 counts/min. Each foil was counted at least once on each side for one minute in each of the three counters.

7.1.4. Weight Normalization

Since the chemical separations were not quantitative, the relative uranium content on each planchet had to be weight-normalized. The usual procedure was to irradiate sets of samples on a wheel rotating in a relatively constant and fairly thermal neutron flux and then to beta count the resulting fission product activity. Weight normalizations were obtained by measuring the ratios of sample activities to those of a simultaneously irradiated reference uranium sample at equal decay times. A small correction (<1/2%) for the natural uranium background was measured by counting each sample prior to irradiation. The Dy-Al (or Cu) intermediate foils were weight-normalized by wheel irradiation followed by beta counting.

The validity of this procedure for weight normalization was investigated in some detail. The first requirement is that all of the atoms in the uranium and Dy-Al (or Cu) samples be exposed to the same integrated flux. This condition was achieved by making the samples sufficiently thin ($\approx$ 1 mg U/cm^2 and $\approx$ 2 mg Dy/cm^2) to minimize thermal self-shielding and flux depression effects and by using a fairly thermal neutron flux. The second requirement is that the counting procedure be identical to that used after the original irradiation in the critical experiment lattice to avoid errors due to variations in sample uniformity and thickness. Although beta counting was used exclusively, the U^{239} activity of the uranium samples was counted after the original irradiation and chemical processing, but the fission product activity was counted after the weight-normalization irradiation. The equivalence of the two procedures was verified in the following ways:

1. After one-week decay, the natural uranium activity in the 180-kev peak was gamma counted in a 400-channel scintillation spectrometer. The integral gamma counts from different uranium samples were found to be closely proportional to their fission product beta counts after the samples were reirradiated.

2. Several samples were fired for several hours in an oven at 900 C. The U_3O_8 residues were carefully weighted and agreed with the fission product beta count method of weight normalization to within 0.5%.

3. In one series of experiments, the uranium samples were both beta and gamma counted after the critical experiment irradiation and again after the weight-normalization irradiation. Although the weight-normalization factors obtained by beta and gamma counting differed by as much as 10%, the weight-normalized activities agreed to within 1% when the consistent weight-normalization factor was used.

7.1.5. Calibration

The calibration factor Φ was obtained from separate irradiations that were performed in a well-thermalized neutron flux to reduce the error in $(C_U - 1)/C_U$ and $C_X/(C_X - 1)$. Uranium samples were prepared by dissolving small portions of the fuel in hot concentrated nitric acid, pipetting on 0.5-inch diameter aluminum and cadmium planchets, and drying under an infrared heat lamp. In the most recent measurements in the thermal column of the University of Virginia (U-Va) Research Reactor, the deposit thickness was about 14 mg UO_2/cm^2, and in earlier work in the beam port of the Lynchburg Pool Reactor (LPR) a range of thickness from about 10 to 160 mg UO_2/cm^2 was studied. The Dy-Al and copper intermediate foils had the same composition and size as those described for the lattice irradiations.

After irradiation, the intermediate foils were beta counted, and the uranium samples were dissolved, chemically processed, and U^{239} beta counted following the procedure described in Section 7.1.3. The counting equipment used in Lynchburg was taken to the University of Virginia so that the U-Va calibrations could be performed under comparable conditions. Counting began about 45 minutes after reactor shutdown, and total counts accumulated from each sample in each run exceeded 100,000. Bare and cadmium-covered runs were normalized by four Dy-Al monitor foils. All samples were weight-normalized by reactivation and beta counting, as described in Section 7.1.4.

In the series of LPR calibrations, the effects of flux depression and self-shielding due to sample thickness were investigated by irradiating bare and cadmium-covered 4.02%-enriched UO_2 samples varying in thickness from about 10 to 160 mg UO_2/cm^2. Although both $A_U^{'B}$ and C_U varied with sample thickness, as shown in Figure 7-3, the thermal activity was essentially constant, i.e.,

$$A_U^{'B}\left(\frac{C_U - 1}{C_U}\right) = \left(A_U^{'B} - A_U^{'C}\right) = A_U^{'Th}$$

These results are consistent with a calculated thermal self-shielding and flux depression for 160 mg UO_2/cm^2 of less than 0.5% ($\Sigma_a t/2 \approx 0.005$). For the Dy-Al samples (2 mg Dy/cm^2), thermal self-shielding and flux depression are less than 0.5% ($\Sigma_a t/2 = 0.004$).

The calibration factors are summarized in Table 7-1, where the core numbers refer to the applicable critical experiment lattice. Only the first two columns are internormalized, but their close agreement supports the validity of the standard technique used in all cases. The unweighted average of the LPR and U-Va calibrations is used for Cores IV, X, XI, and XII. The calibration factor for Cores I and IX was measured quite early in the program, so its precision is somewhat poorer. The first calibration factor (Core III) was obtained before techniques were standardized and is subject to an appreciably larger uncertainty.

7.2. Results

The results of the measurements are summarized in Table 7-2. Details on the calculation of the non-1/v correction K are given in Reference 22, and the calibration factors were taken from Table 7-1. The values of $C_{28} - 1$ were increased by (1.0 ± 0.5) % to correct for neutron thermalization, as discussed in the next section. The ratio of epithermal-to-thermal absorptions ρ_{28} is obtained from the U^{238} cadmium ratio C_{28} using the relation $\rho_{28} = (C_{28} - 1)^{-1}$. The errors are based on the consistency of repeated runs, unweighted and propagated by standard statistical methods. In all cores except Core III, at least three bare runs (six uranium samples) and at least one cadmium-covered run were made.

As shown in Figure 7-4, the results appear to be internally consistent. The errors in the measurements on the latest cores (XIII through XVII) are 1 to 2% in $C_{28} - 1$ or ρ_{28}. The accuracy of the measurements on the first few cores did not reach this level because techniques were still being developed. Therefore, the results for 4.02% enrichment, M/W = 1.0 should not be weighted too strongly.

Table 7-1. Calibration Factors

Factor	Reactor and Cores			
	4.02% Fuel enrichment		2.46% Fuel enrichment	
	LPR IV, X, XI, XII	U-Va[a] IV, X, XI, XII	U-Va[a] XIII thru XVII	LSR I, IX
C_U	3.72[b]	51.72 ± 6.20	45.68 ± 4.27	65.2 ± 1.8
C_{Dy}	601 ± 3	2038 ± 14	2259 ± 201	> 1000
C_{Cu}	- -	1591 ± 131	1488 ± 67	- -
$(C_U - 1)/C_U$	0.731[b]	0.9807 ± 0.0023	0.9781 ± 0.0020	0.985 ± 0.001
$C_{Dy}/(C_{Dy} - 1)$	1.002 ± 0.001	1.0005 ± 0.0000	1.0004 ± 0.0000	1.001 ± 0.001
$C_{Cu}/(C_{Cu} - 1)$	- -	1.0006 ± 0.0001	1.0007 ± 0.0000	- -
$A'^{B}_{U} / A'^{B}_{Dy}, \times 10^{-2}$	5.248[b]	3.867 ± 0.039	2.826 ± 0.010	1.86 ± 0.10
$A'^{B}_{U} / A'^{B}_{Cu}, \times 10^{-2}$	- -	1.681 ± 0.020	1.287 ± 0.005	- -
$\Phi_{Dy}, \times 10^{-2}$[c]	3.870 ± 0.066	3.793 ± 0.039	2.765 ± 0.010	1.83 ± 0.10
$\Phi_{Cu}, \times 10^{-2}$	- -	1.649 ± 0.020	1.260 ± 0.005	- -

(a) Copper intermediate foils were used for a few check measurements at U-Va. Otherwise, Dy-Al intermediate foils were used.

(b) Depends on sample thickness. See Reference 22.

(c) For Core III, use $(2.2 \pm 0.1) \times 10^{-3}$. For Cores IV, X, XI, XII, use $(3.83 \pm 0.04) \times 10^{-2}$, the average obtained from LPR and U-Va data.

Table 7-2. Cadmium Ratio of U^{238}

Factor	Core number I	III	IV	IX	X	XI	XII	XIII	XIV	XV	XVI	XVII
Enrichment, %	4.02	4.02	4.02	4.02	4.02	4.02	4.02	2.46	2.46	2.46	2.46	2.46
M/W	1.006	1.006	1.006	1.006	1.195	1.195	1.195	1.001	1.001	1.001	0.651	0.651
D_2O, mole %	0.0	76.5	69.7	49.7	0.0	70.1	49.7	0.0	70.0	49.8	85.5	70.0
$(A^B_{Dy}/A^B_U)_R$	10.98 ±0.29	30.1 ±0.2	2.323 ±0.085	6.330 ±0.303	4.470 ±0.061	1.810 ±0.011	2.589 ±0.052	11.17 ±0.09	5.399 ±0.023	7.426 ±0.029	5.162 ±0.021	7.490 ±0.071
$(C_{Dy})_R$	16.16 ±0.57	6.34 ±0.02	6.560 ±0.120	9.128 ±0.250	12.81 ±0.27	5.773 ±0.072	8.130 ±0.019	25.28 ±1.17	11.49 ±0.04	15.80 ±0.30	11.34 ±0.11	16.28 ±1.60
$\left[(C_{Dy} - 1)/C_{Dy}\right]_R$	0.938 ±0.002	0.842 ±0.001	0.8476 ±0.0028	0.8904 ±0.0030	0.9219 ±0.0017	0.8268 ±0.0030	0.8770 ±0.0001	0.9604 ±0.0018	0.9130 ±0.0003	0.9367 ±0.0013	0.9119 ±0.0008	0.9386 ±0.0061
Φ_{Dy}, $\times 10^{-2}$	1.83 ±0.10	0.22 ±0.01	3.83 ±0.04	1.83 ±0.10	3.83 ±0.04	3.83 ±0.04	3.83 ±0.04	2.765 ±0.011	2.765 ±0.011	2.765 ±0.011	2.765 ±0.011	2.765 ±0.011
K	1.028 ±0.006	1.082 ±0.016	1.070 ±0.013	1.048 ±0.010	1.033 ±0.007	1.080 ±0.016	1.056 ±0.011	1.018 ±0.004	1.043 ±0.009	1.031 ±0.006	1.043 ±0.009	1.029 ±0.006
$C_{28} - 1$	0.243 ±0.018	0.065 ±0.003	0.089* ±0.004	0.123 ±0.009	0.197 ±0.004	0.067 ±0.001	0.102 ±0.003	0.439 ±0.006	0.168 ±0.002	0.250 ±0.003	0.159 ±0.002	0.253 ±0.004
ρ_{28}	4.12 ±0.31	15.4 ±0.7	11.2* ±0.5	8.13 ±0.06	5.08 ±0.10	14.9 ±0.2	9.80 ±0.29	2.28 ±0.03	5.95 ±0.07	4.00 ±0.05	6.29 ±0.08	3.95 ±0.06

* Measurement repeated in another program. $C_{28} - 1 = 0.087 \pm 0.003$, $\rho_{28} = 11.5 \pm 0.4$.

7.3. Discussion

7.3.1. Non-1/v Correction

The use of dysprosium as the intermediate foil material requires a small non-1/v correction K in Equation 7-1 for $C_{28} - 1$ and ρ_{28}. The validity of the calculation was checked in two lattices by repeating the measurements with copper as the intermediate foil material. Although copper is less advantageous than dysprosium because its cadmium ratio is much lower, it does have a 1/v cross section dependence that makes K_{Cu} unity.

The results of the measurements are summarized in Table 7-3. The values of $C_{28} - 1$ derived from the dysprosium data and the calculated K differ slightly from the values derived from the copper data and a K of unity. This difference is consistent with experimental errors. Therefore, the quoted error in K, given as 20% of K-1, appears reasonable, and its contribution to the total error in $C_{28} - 1$ is almost negligible.

7.3.2. Cadmium Perturbation

Although the measurement of $C_{28} - 1$ by the thermal activation technique does not require a cadmium-covered uranium irradiation in the critical experiment lattice, the cadmium-covered uranium activity was measured in some of the lattices to assess the importance of perturbations by the cadmium sleeve used in conventional U^{238} cadmium ratio measurements. These perturbations may originate from the displacement of moderator by the sleeve (Dancoff effect) and the depression of the source of fast neutrons in the neighborhood of the fuel rod.

The true cadmium ratio C_{28} is defined as

$$C_{28} = A_U^B / A_U^C \qquad (7\text{-}3)$$

where A_U^B and A_U^C are the unperturbed bare and cadmium-covered uranium saturated activities. If the cadmium sleeve in the cadmium-covered measurements perturbs A_U^C to produce

$$F = A_U^{'C} / A_U^C \qquad (7\text{-}4)$$

where $A_U^{'C}$ is the perturbed cadmium-covered activity, then the apparent cadmium ratio is

$$C_a = A_U^B / A_U^{'C} = \frac{1}{F} C_{28}. \qquad (7-5)$$

The difference between C_a, obtained from Equation 7-5, and C_{28} derived by the thermal activation method (Equation 7-1) can be attributed to the perturbation by the cadmium sleeve in the $A_U^{'B}$ measurement. This hypothesis was tested in one of the lattices (Core X) by measuring both C_a and C_{28} with cadmium sleeves of varying lengths. The geometry of Figure 7-1 was used, but the lengths of the fuel and guard slugs were reduced proportionally. The results are listed in Table 7-4 and compared in Figure 7-5.

The hypothesis that the difference between C_a and C_{28} is due to cadmium perturbations of the epithermal uranium activity is supported by the following observations:

1. C_a decreases as the quantity of cadmium is reduced, but C_{28} remains essentially constant in all three measurements of Table 7-4. Furthermore, C_a tends to converge to C_{28} as the quantity of cadmium goes toward zero.

2. Although the accuracy of F is limited to a few percent because of the uncertainty in C_a, values of F measured in other cores were always less than unity and were smallest when the moderator was light water.

Table 7-3. Comparison of Dy and Cu as Intermediate Foils

Factor	Core XIV	Core XV
$(A^B_{Dy}/A^B_U)_R$	5.399 ± 0.023	7.426 ± 0.029
$(A^B_{Cu}/A^B_U)_R$	20.68 ± 0.15	24.54 ± 0.14
$(C_{Dy})_R$	11.5 ± 0.04	15.8 ± 0.3
$(C_{Cu})_R$	2.16 ± 0.03	2.93 ± 0.03
$\left[(C_{Dy} - 1)/D_{Dy}\right]_R$	0.9130 ± 0.0003	0.9367 ± 0.0013
$\left[(C_{Cu} - 1)/C_{Cu}\right]_R$	0.5375 ± 0.0066	0.6586 ± 0.0031
Φ_{Dy}, $\times 10^{-2}$	2.765 ± 0.011	2.765 ± 0.011
Φ_{Cu}, $\times 10^{-2}$	1.260 ± 0.005	1.260 ± 0.005
K_{Dy}	1.043 ± 0.009	1.031 ± 0.006
K_{Cu}	1.000	1.000
$(C_{28} - 1)_{Dy}$	0.166 ± 0.002	0.247 ± 0.003
$(C_{28} - 1)_{Cu}$	0.163 ± 0.003	0.255 ± 0.003
Difference	+ 0.003	- 0.008

Table 7-4. Perturbation by Cadmium Sleeve in Core X

Length of cadmium, in.	C_a (Equation 7-5)	C_{28} (Equation 7-1)	F
2-3/4	1.275 ± 0.019	1.194 ± 0.004	0.937 ± 0.017
1-3/4	1.247 ± 0.019	1.196 ± 0.004	0.959 ± 0.017
5/8	1.228 ± 0.024	1.195 ± 0.004	0.973 ± 0.023

7.3.3. Effect of Cadmium on C_{Dy}

The perturbation of the intermediate foil activity by cadmium is minimized by using a material that is a strong thermal absorber, such as dysprosium. Then the dysprosium's cadmium ratio in the lattice C_X is very large, and the error in $(C_X - 1)/C_X$ of Equation 7-1 is small. Cadmium perturbations of the cadmium-covered dysprosium activity were considered during the experiments on Core X described in the preceding section. C_D decreased slightly as the length of the cadmium sleeve was reduced, but the maximum change in $(C_D - 1)/C_D$ was only 0.3% because C_D was so large.

Another possible source of error in C_D involves neutron thermalization. As is shown by the standard irradiation geometries of Figures 7-1 and 7-2, epithermal neutrons can be thermalized by scattering in the UO_2 between the cadmium covers and the Dy-Al intermediate foil. This effect, which increases the cadmium-covered activity and decreases the cadmium ratio, was observed in the U^{235} cadmium ratio measurements discussed in Section 6. The importance of this error was studied by repeating cadmium-covered dysprosium measurements in many of the lattices that had the Dy-Al intermediate foil completely enclosed by cadmium, i.e., there was no UO_2 between the cadmium and the Dy-Al foil. In all cases, C_D was slightly larger, as would be expected since this measurement should be free from thermalization error. However, the change in $(C_D - 1)/C_D$ was quite small—between 0.5 and 1.5% in all lattices.

Figure 7-1. C_{28} Loading Arrangement (4.02%-Enriched UO_2)

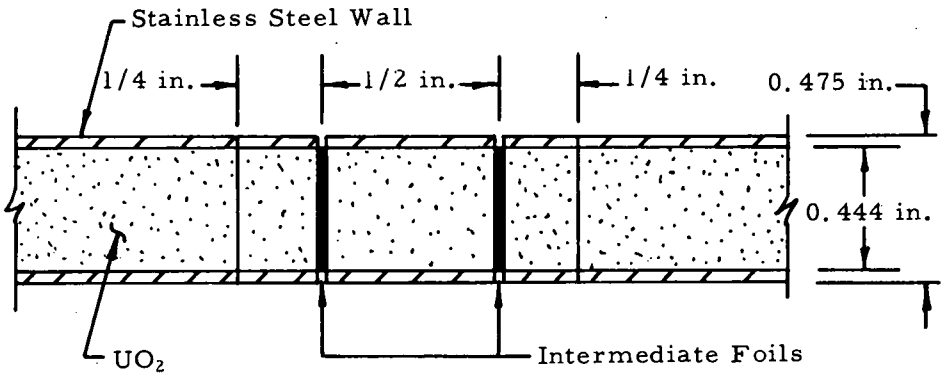

Bare Irradiation

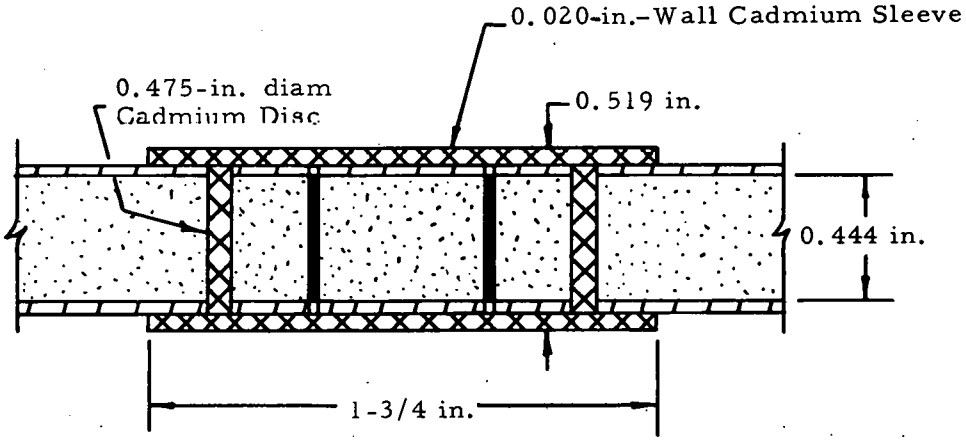

Cadmium-Covered Irradiation

Figure 7-2. C_{28} Loading Arrangement (2.46%-Enriched UO_2)

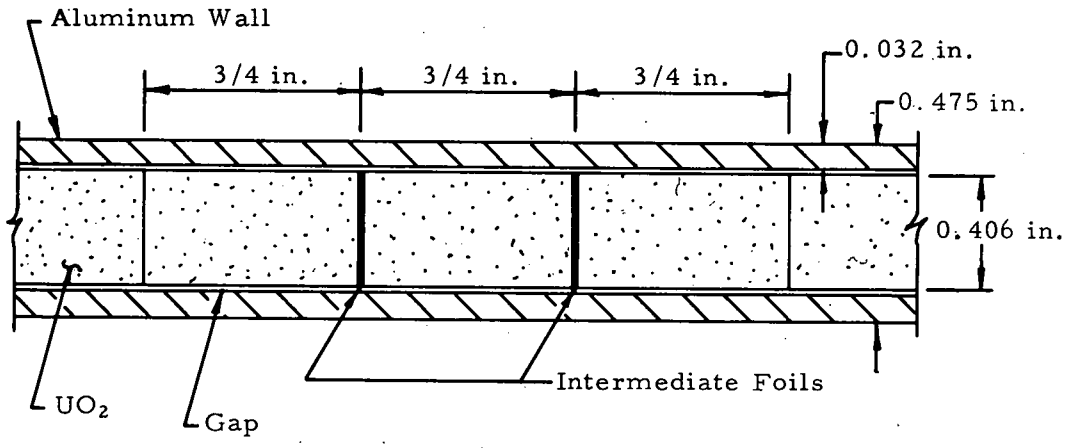

Bare Irradiation

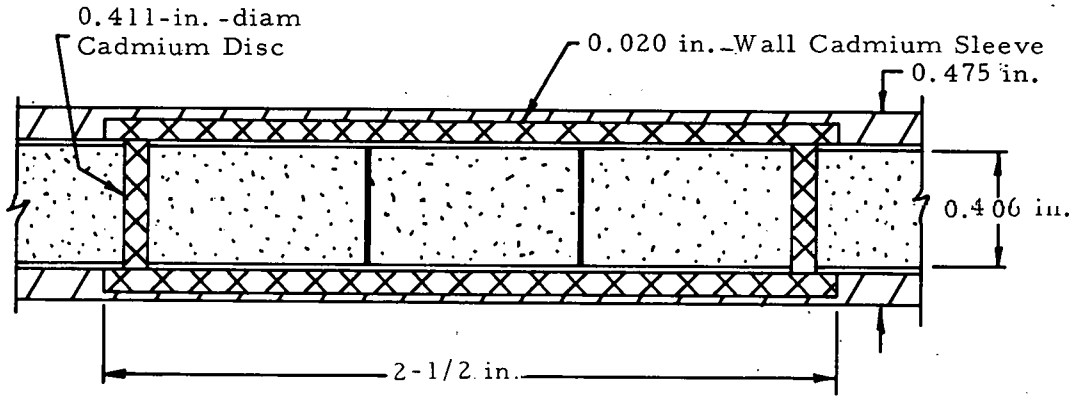

Cadmium-Covered Irradiation

Figure 7-3. Uranium Activity Vs Sample Thickness

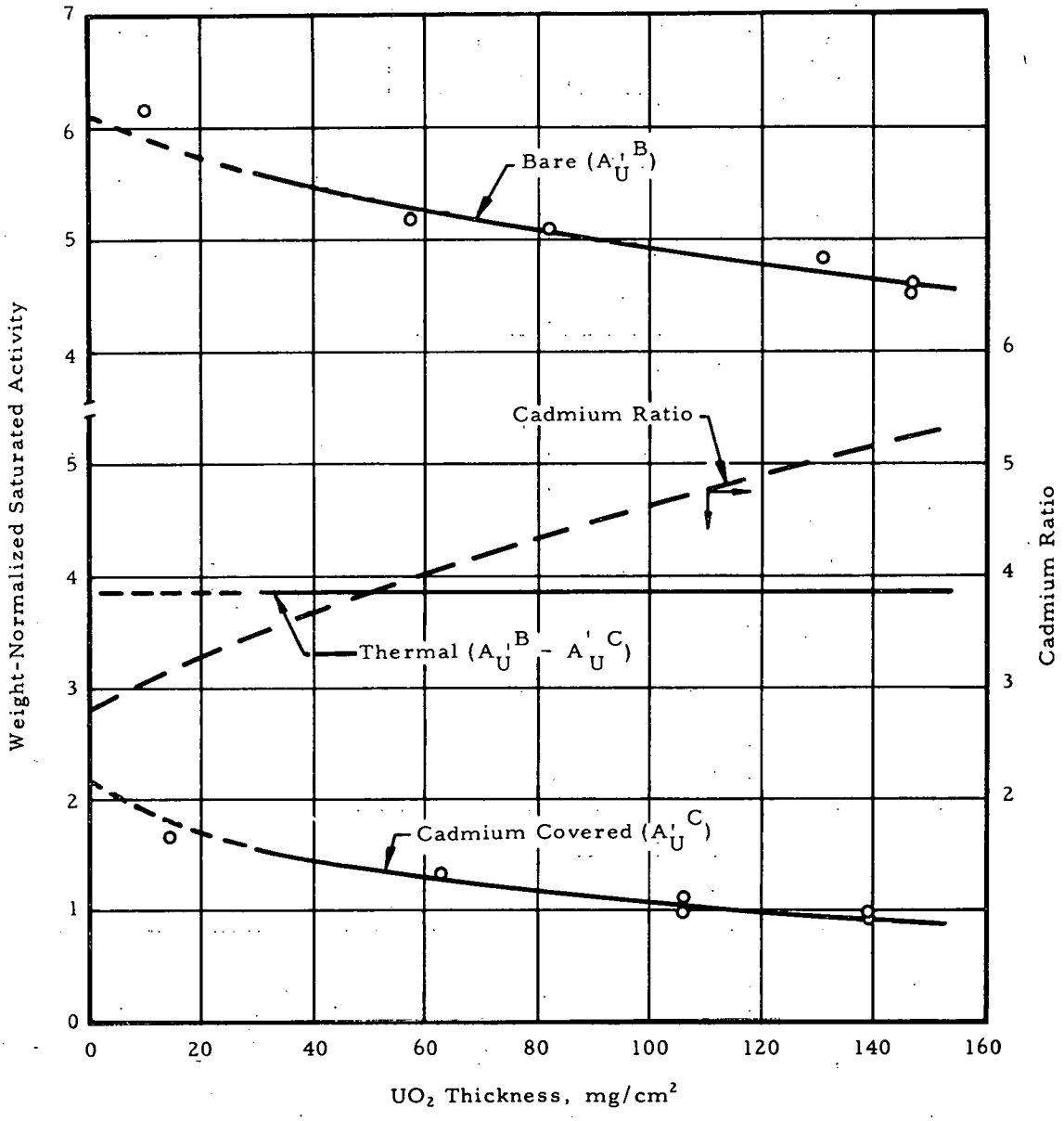

Figure 7-4. Cadmium Ratio of U^{238}

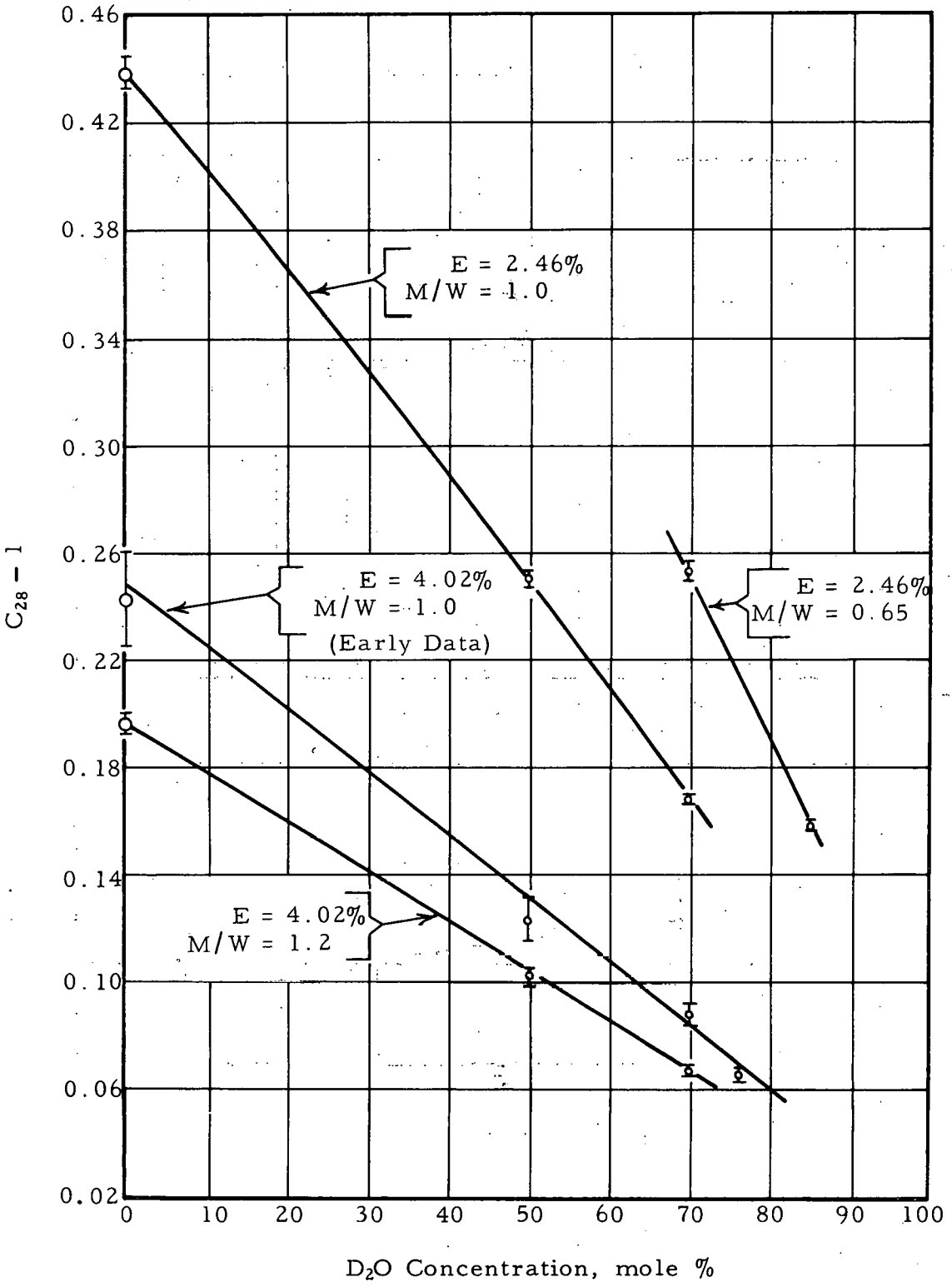

Figure 7-5. C_{28} Vs Length of Cadmium Sleeve

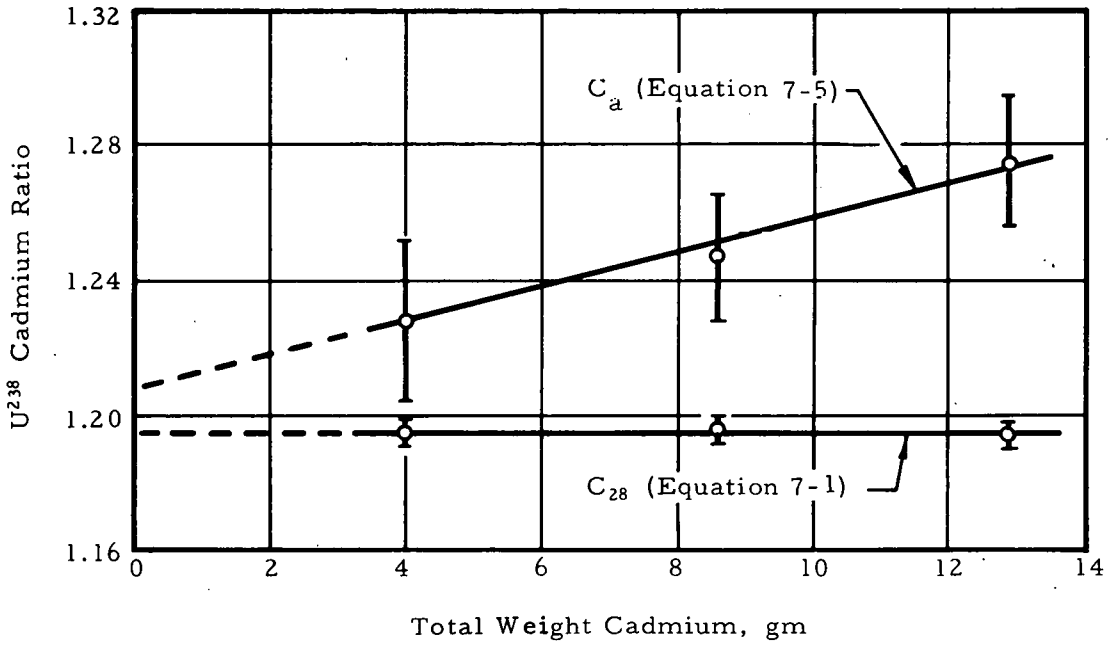

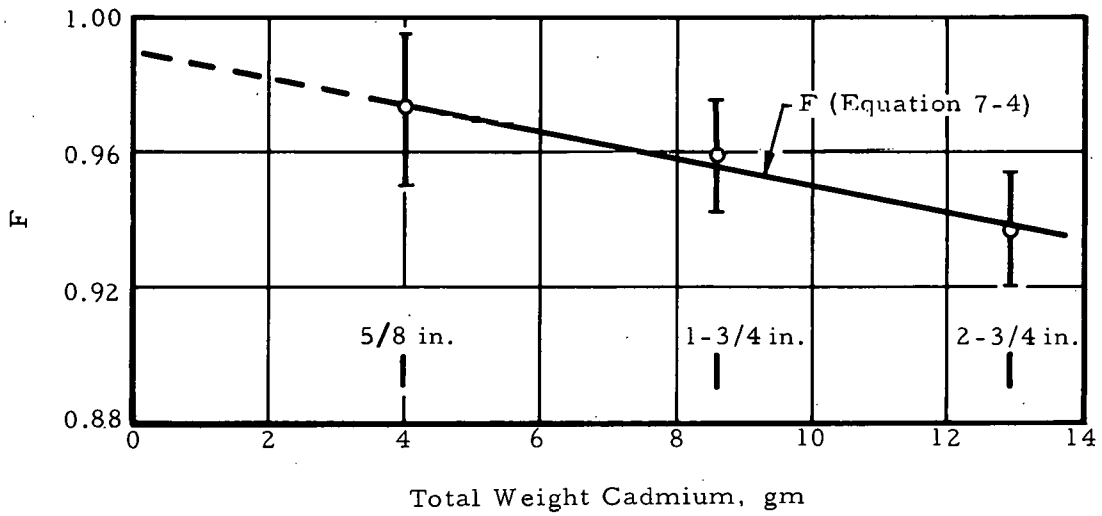

8. THEORETICAL ANALYSIS

8.1. Methods of Calculation

8.1.1. BPG Code

Two basic approaches to describing lattice criticality conditions were used. First, the BPG code, which was developed during the early stages of the SSCR Basic Physics Program, was used with measured buckling and disadvantage factors for predicting core criticality. The BPG code is a multigroup (39 energy groups) point reactor spectrum code set up for these studies with a 0.4-ev thermal cutoff. Various U^{238} resonance integrals (the source of which is described below) and resonance distributions (ψ sets) were applied to the BPG codes, and the results were analyzed. A detailed description of the BPG code is given in Appendix A.

8.1.2. Multiregion Codes

The second approach centered around the use of multigroup multiregion criticality codes as a check on the validity of the BPG point model using the measured bucklings. The P1MG code[23], and IBM 704 multigroup one-dimensional code, was initially picked for this comparison. The P1MG code was set up with the same 39-group cross section library used in the BPG calculation and employed the same measured disadvantage factors. Similarly, a single multiregion polygroup code (with four energy groups) was checked against both the BPG and the P1MG results in an effort to establish the importance of spectrum effects by using more or less detail in spectrum description. The results of the point reactor model compared with the results of the multiregion model are discussed below. A most significant aspect of using these methods was the comparison of the P1MG model with the simple four-group model. The difference in results was so small that it was decided that the four-group model would be used generally to check BPG results and

that the only P1MG cases calculated would be those necessary to establish the validity of the polygroup model over the desired parameter range. Therefore, the basic multiregion study was conducted with the four-group diffusion code backed up by P1MG results. It is important to note that all four-group coefficients used in the multiregion calculations were generated by the BPG code.

8.1.3. RIP and U^{238} Resonance Integral

The extreme sensitivity of the SSCR type lattices to variation in the resonance integral of U^{238} provoked a variety of approaches to predicting the correct values over the lattice parameter range. Actually, three sources for U^{238} resonance integrals were investigated. These methods are described as follows:

1. RIP Code

A theoretical analysis of the total resonance effect was formulated in the RIP code. This code was used to calculate a lattice resonance integral from resonance peak parameters, temperatures, and self-shielding corrections. The Bell[24] approximation of the self-shielding correction (Dancoff correction) was used in the RIP calculation. In addition, the code also calculated the resonance distribution function (ψ sets) necessary for both the BPG and the P1MG codes. The detailed formulation of this code is given in Appendix A.

2. Hellstrand Plus Bell Approximation

The second approach to resonance integral generation was the use of Hellstrand's[25] formula for RI_{28} in UO_2, which is given as:

$$RI_{28} = 4.15 + 26.6 \sqrt{\gamma S/M}_{ox}$$

where γ = self-shielding correction

S/M_{ox} = surface-to-mass ratio of oxide pellet

Again Bell's approximation of the Dancoff correction was employed.

3. Hellstrand Plus Sauer Approximation

The third and probably the best approach, so far as analytical comparison with experiment results is concerned, involved

the same Hellstrand formulation used in the second approach but included the latest more exacting Sauer[26] approximation of the Dancoff shielding correction. Just recently published, this approximation seemed to fit the experimental data better than any previous approximations.

The resonance integrals resulting from the three sources are shown in Figures 8-1 through 8-3 as a function of D_2O concentration, fuel enrichment, and metal-to-water ratio. The total resonance integral computed by RIP is approximately 2 barns higher than the values obtained from the Hellstrand formulation from U^{238}. This agreement is quite good in view of the constant density approximation employed by RIP. In addition, the high energy absorption contribution above 30 kev computed by RIP is higher than the 0.80 barns normally employed in comparing calculated and experimental single-pin resonance integrals. Although experimental cross sections are available in the high energy region, use of the 1/E spectrum in evaluating

$$\int_{\text{high energy}} \sigma_a(E) \frac{dE}{E}$$

as is done at lower energies is not valid for several reasons:

1. The fission spectrum neutrons influence the flux.
2. Inelastically scattered neutrons contribute directly to the flux.
3. The scattering cross section of many moderators is not constant in the high energy range.

The distribution of the resonance integral in the unresolved and resolved resonance regions, however, is believed to be quite accurate, particularly for U^{238}, for which the resonance parameters are well defined.

The associated resonance distributions (ψ sets) for all cases were generated by the RIP program. The distribution in each core was normalized to the total resonance integral generated for the particular lattice conditions regardless of source.

8.2. Comparative Results

8.2.1. Lattice Criticality

Table 8-1 is a tabulation of the various core configurations investigated and the resulting criticality conditions calculated by the several approaches described above. In all cases the experimental lattice was critical ($k_{eff} = 1.000$). Each lattice is described concerning enrichment, D_2O concentration, metal-to-water ratio, and boron concentration if required to maintain a critical condition. Four calculated reactivity conditions were considered and are defined by analytical model conditions as follows:

k_{eff} #1
a. BPG point reactor model.
b. Measured bucklings and disadvantage factors.
c. U^{238} resonance integral generated by RIP.
d. Self-shielding correction by Bell's approximation.
e. Resonance distribution (ψ set) generated by RIP.

k_{eff} #2
a. BPG point reactor model.
b. Measured bucklings and disadvantage factors.
c. U^{238} resonance integral generated from Hellstrand's equation.
d. Self-shielding correction by Bell's approximation.
e. Resonance distribution (ψ set) generated by RIP.

k_{eff} #3
a. BPG point reactor model.
b. Measured bucklings and disadvantage factors.
c. U^{238} resonance integral generated from Hellstrand's equation.
d. Self-shielding correction by Sauer's approximation.
e. Resonance distribution (ψ set) generated by RIP.

k_{eff} #4
a. Four-group multiregion reactor model.
b. Measured disadvantage factors.
c. U^{238} resonance integral generated from Hellstrand's equation.

d. Self-shielding correction by Sauer's approximation.

e. Resonance distribution (ψ set) generated by RIP.

f. Values in parentheses were calculated by the P1MG code and are shown for comparison with four-group results. The P1MG model conditions are the same as those for k_{eff} #4.

As previously noted, the SSCR lattice is sensitive to the resonance integral used for the criticality calculation. By comparing the four reactivity values given in Table 8-1, this variation is evident. The values listed for k_{eff} #1 are generally lower than the remaining three columns, which is clearly indicative of the higher resonance integrals (Figures 8-1 through 8-3) generated by the RIP program. A comparison of k_{eff} #2 with k_{eff} #3 indicates the effects of the two basic self-shielding corrections (Bell and Sauer) applied to the Hellstrand equation. Both of these approaches give generally a better comparison with the critical lattice conditions than the initial method. Of these models the results in the k_{eff} #3 column represent the best fit for the point reactor model. Of most value, in terms of establishing an analytical design model for future core work, are the results listed under k_{eff} #4. It is clear that the methods employed in the multiregion calculation gave reasonable answers over the entire parameter range (maximum criticality error of only 2.1% in excess reactivity at the highest D_2O concentration) without the aid of measured bucklings. Excellent comparison between the four-group and the P1MG results adds even more credence to the basic model. Figures 8-4 through 8-7 illustrate the comparison of the four-group and P1MG thermal flux profiles. Thermal flux shapes in the fuel region show good agreement. Some deviation is noted in the reflector at the higher D_2O concentrations.

Table 8-1. Criticality Comparison
(All Experiments Critical Under Prescribed Conditions)

Core no.	M/W	Fuel Enrich., wt% U^{235}	D_2O, mole %	Boron, gm B/ℓ	k_{eff} #1	#2	#3	#4*
I	1.006	4.02	- -	- -	0.980	1.004	0.986	1.001 (0.998)
II	1.006	4.02	- -	3.390	1.002	1.025	1.008	1.009
III	1.006	4.02	76.50	- -	0.958	1.012	1.001	0.995 (0.992)
IV	1.006	4.02	69.70	- -	0.964	1.012	1.001	1.006
V	1.006	4.02	69.70	0.422	0.966	1.014	1.003	1.003
VI	1.006	4.02	49.63	1.790	0.988	1.021	1.012	1.003
IX	1.006	4.02	49.66	- -	0.959	0.992	0.985	1.004
X	1.195	4.02	- -	- -	0.975	0.999	0.993	1.005 (1.001)
XI	1.195	4.02	70.10	- -	0.956	1.005	0.995	1.001 (0.996)
XII	1.195	4.02	49.68	- -	0.959	0.997	0.989	0.999
XIII	1.001	2.46	- -	- -	1.010	1.029	1.014	1.015
XIV	1.001	2.46	70.09	- -	0.980	1.026	1.017	1.021
XV	1.001	2.46	49.76	- -	0.973	1.006	1.000	1.018
XVI	0.651	2.46	85.50	- -	0.990	1.028	1.016	1.021
XVII	0.651	2.46	70.00	- -	0.982	1.012	1.002	1.016

*Values in parentheses are taken from PlMG results.

8.2.2. Cadmium Ratios

Cadmium ratios for U^{238} and U^{235} were measured in most of the experimental lattices. As an additional check on the analytical model resulting from the theoretical program, a comparison was made between the experimental and the analytical values. The results of this comparison are tabulated in Table 8-2. All measured and calculated cadmium ratios and lattice descriptions for each core are shown.

The U^{238} comparison shows a 2.7% maximum error, but the majority of the calculated values match the experimental values with less than a 1% difference. However, the agreement in the cadmium ratio minus one or in ρ_{28} is less satisfactory.

The U^{235} ratios were considered to be somewhat more sensitive to the epithermal cutoff used in the calculational model. Therefore, these cadmium ratios are listed for both a 0.4-ev and a 0.625-ev cutoff value since the measured ratio probably falls between these analytical energy bounds. The U^{235} cadmium ratio is defined as the ratio of total U^{235} fissions to the U^{235} fissions produced by neutrons above the cadmium cutoff. In general the U^{235} cadmium ratios match the experimental values fairly well if the epithermal cutoff is raised (0.4 ev to 0.625 ev) with the D_2O concentration. The better match at zero D_2O is made with the 0.4-ev cutoff, and the better match at the higher D_2O concentration (76.50%) results from the use of the higher cutoff. No basic analysis was done to establish the real effects of the cadmium on the effective epithermal cutoff measured. Generally the comparison should be taken as a good match over the range of lattice parameter studies and the analytical restraints imposed.

The relative match between measured and calculated cadmium ratios for both U^{238} and U^{235} is illustrated by the ratio of measured-to-calculated values tabulated for each lattice.

Table 8-2. Cadmium Ratio Comparison

Core description					U^{238} cadmium ratio			U^{235} cadmium ratio		
Core no.	M/W	Fuel enrich., wt% U^{235}	D_2O, mole %	Boron, gm B/ℓ	Measured	Calculated	Measured/ Calculated	Measured	0.4 ev/0.625 ev Calculated	Measured/ Calculated
I	1.006	4.02	- -	- -	1.243	1.210	1.027	4.95	4.95/5.76	1.00/0.86
III	1.006	4.02	76.50	- -	1.065	1.063	1.002	2.17	1.97/2.13	1.10/1.02
IV	1.006	4.02	69.70	- -	1.087	1.077	1.009	2.43	2.35/2.58	1.03/0.94
V	1.006	4.02	69.70	0.422	- -	1.074	- -	2.32	2.34/2.65	0.99/0.88
VI	1.006	4.02	49.53	1.790	- -	1.103	- -	2.87	2.54/2.77	1.13/1.04
IX	1.006	4.02	49.66	- -	1.123	1.117	1.005	3.09	2.87/3.15	1.08/0.98
X	1.195	4.02	- -	- -	1.197	1.175	1.019	4.26	- -	- -
XI	1.195	4.02	70.10	- -	1.067	1.061	1.006	2.12	- -	- -
XII	1.195	4.02	49.68	- -	1.102	1.096	1.005	2.74	2.52/2.75	1.09/1.00
XIII	1.001	2.46	- -	- -	1.439	1.435	1.003	7.63	- -	- -
XIV	1.001	2.46	70.09	- -	1.168	1.183	0.987	3.55	- -	- -
XV	1.001	2.46	49.76	- -	1.250	1.261	0.991	4.79	- -	- -
XVI	0.651	2.46	85.50	- -	1.159	1.170	0.991	3.51	- -	- -
XVII	0.651	2.46	70.00	- -	1.253	1.257	0.997	4.95	- -	- -

8.3. Conclusions

The sensitivity of the calculational model to the resonance integral of U^{238} has been demonstrated, and a resonable approach for matching both the reactivity and the neutron characteristics of a D_2O-H_2O modulated core has evolved. Generally, the multiregion, few-group diffusion model provides an adequate means for predicting both lattice criticality and reasonable flux distribution (spatially and energywise) for a large variation in lattice parameters.

Two highly useful computer (BPG and RIP) codes have been written and put into operation for the SSCR concept and other lattices employing heavy or light water moderation. The basic purposes for initiating the theoretical phase of the SSCR Basic Physics Program have been successfully fulfilled.

Figure 8-1. U^{238} Resonance Integral Vs Mole % D_2O Cores I, III, IV, V - 4.0% Enrichment, 1.006 M/W

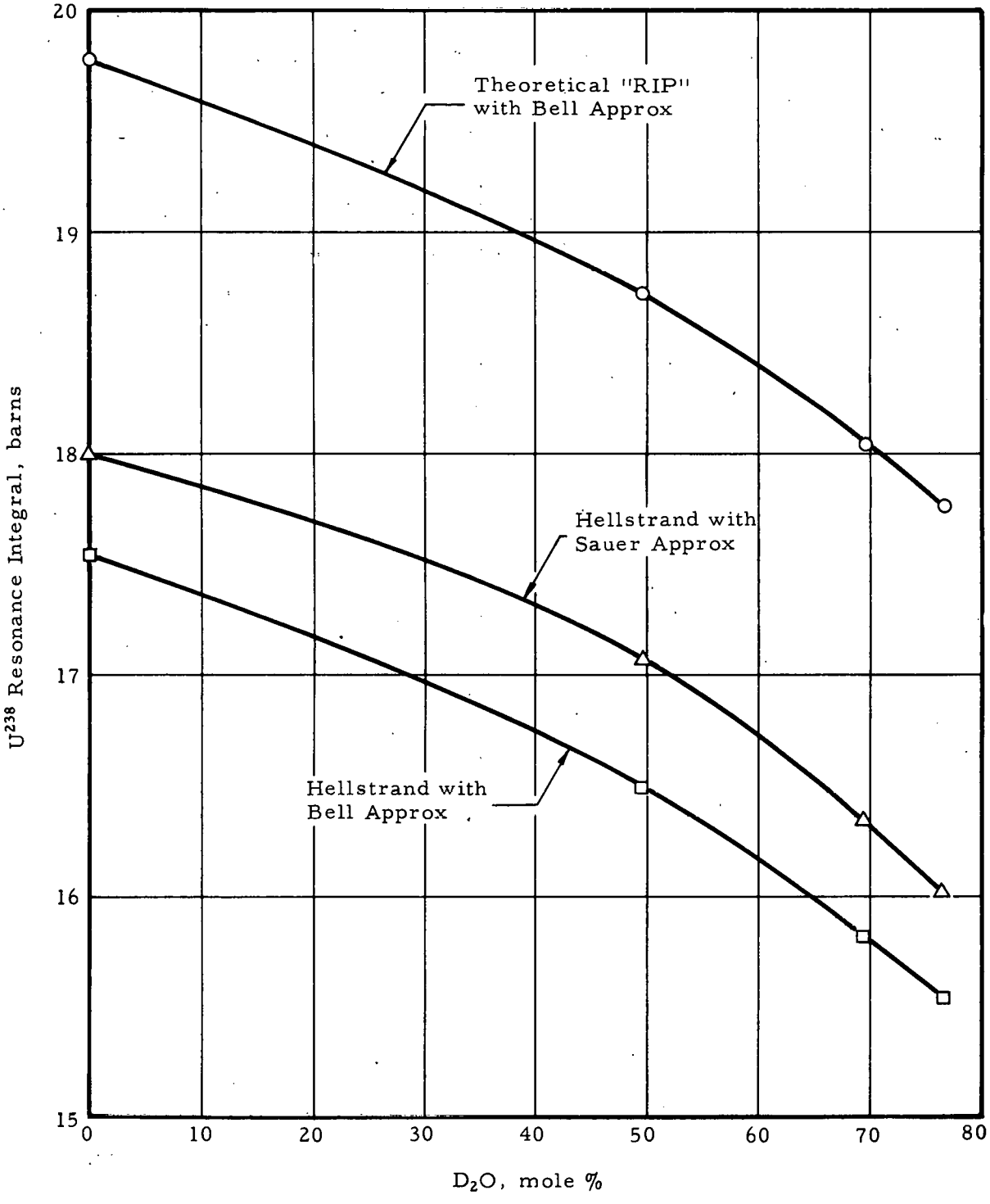

Figure 8-2. U^{238} Resonance Integral Vs Mole % D_2O
Cores X, XI, XII - 4.0% Enrichment,
1.195 M/W

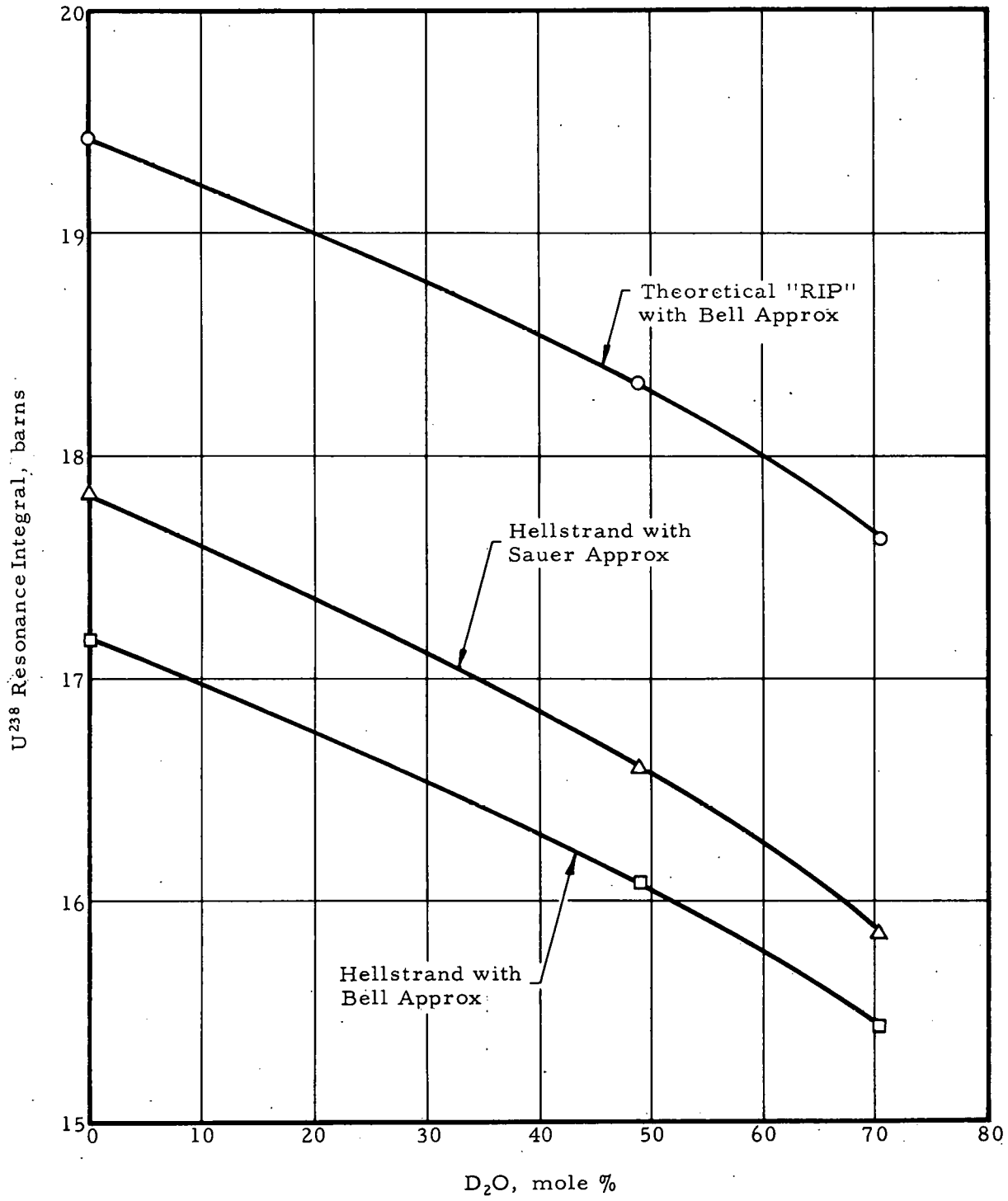

Figure 8-3. U^{238} Resonance Integral Vs Mole % D_2O
Cores XIII, XIV, XV - 2.5% Enrichment,
1.001 M/W

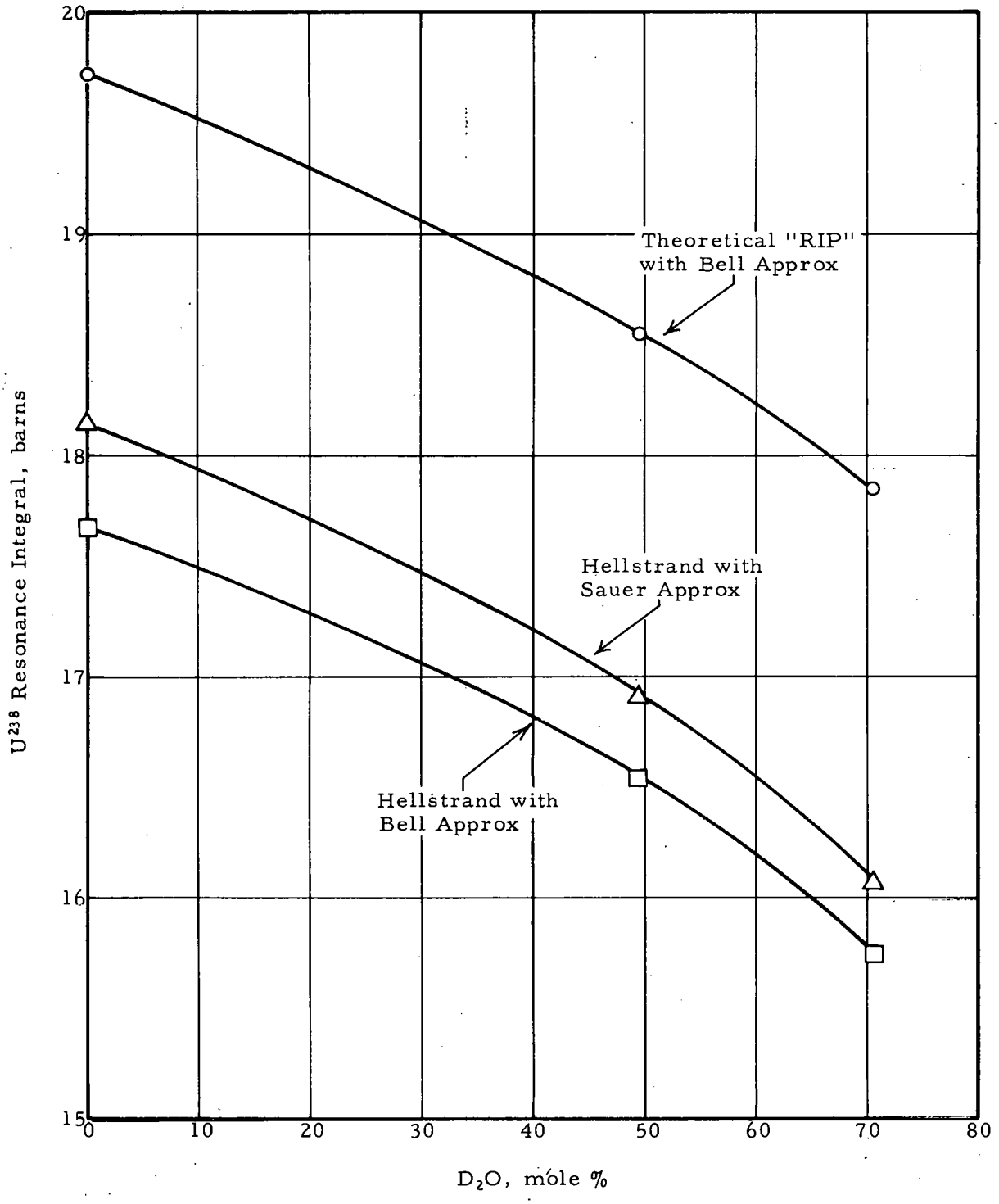

Figure 8-4. Relative Thermal Flux Profile - Core I (0.0% D_2O)

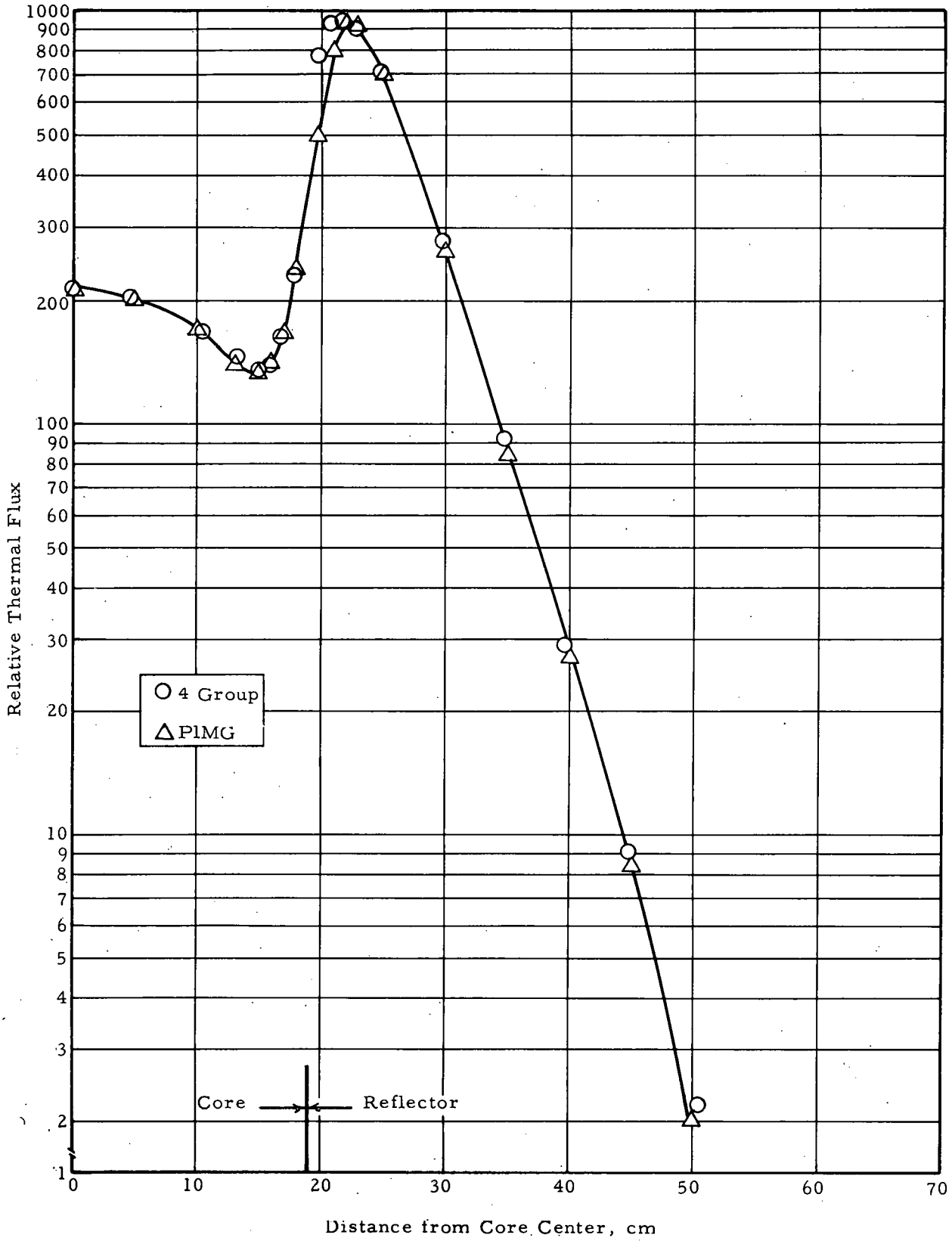

Figure 8-5. Relative Thermal Flux Profile
Core III (76.5% D_2O)

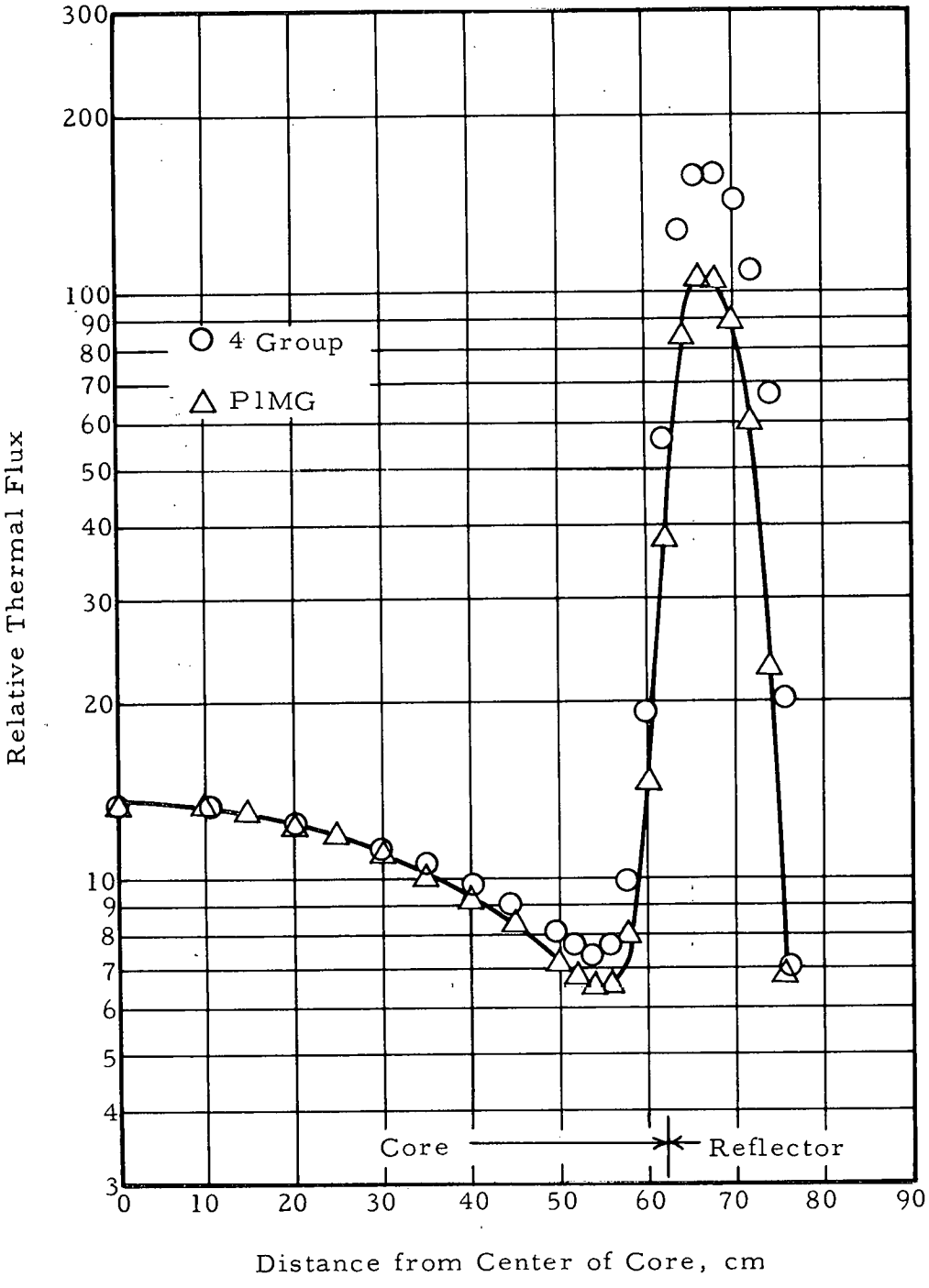

Figure 8-6. Relative Thermal Flux Profile - Core X
(0.0% D_2O)

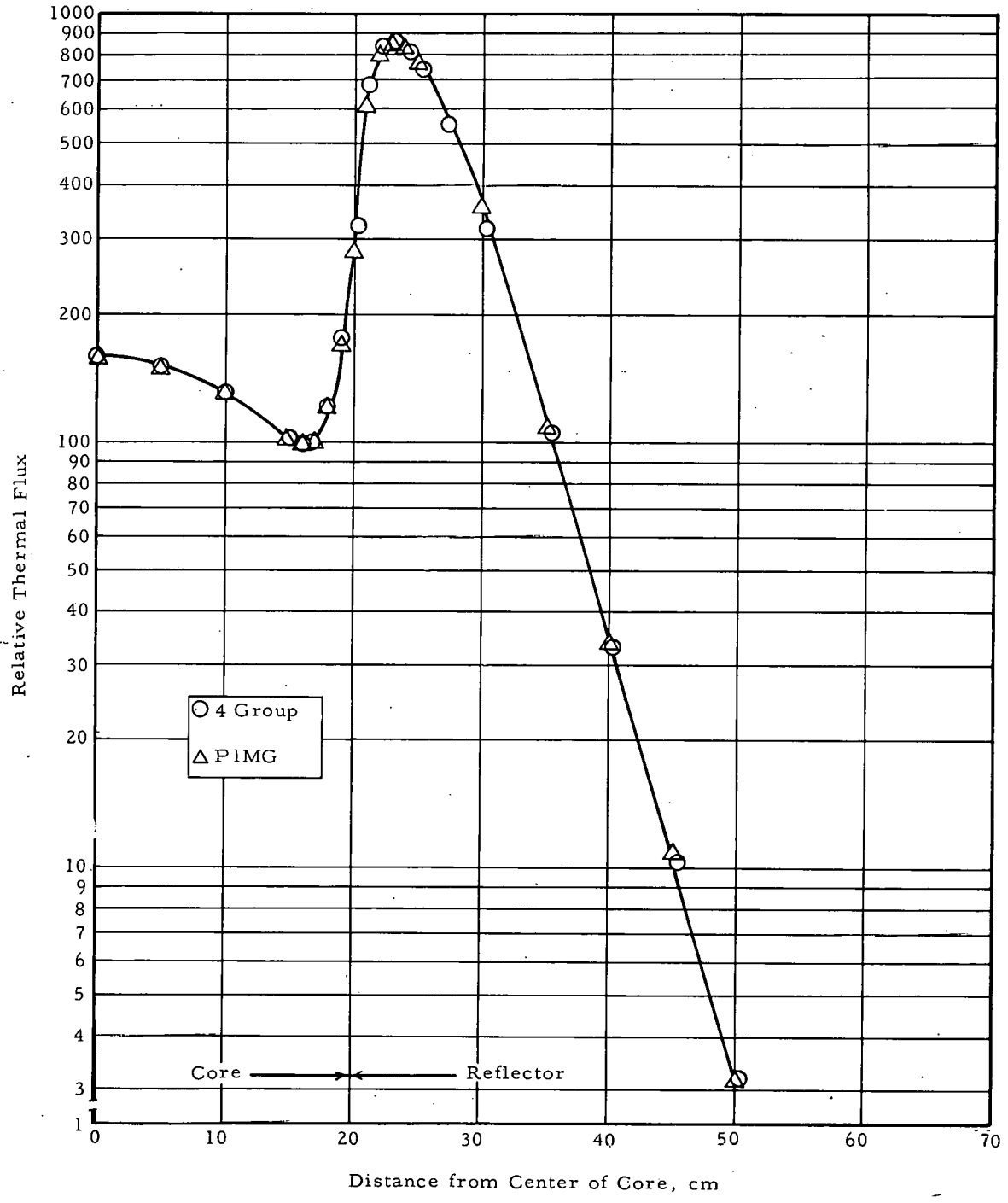

Figure 8-7. Relative Thermal Flux Profile
Core XI (70.1% D_2O)

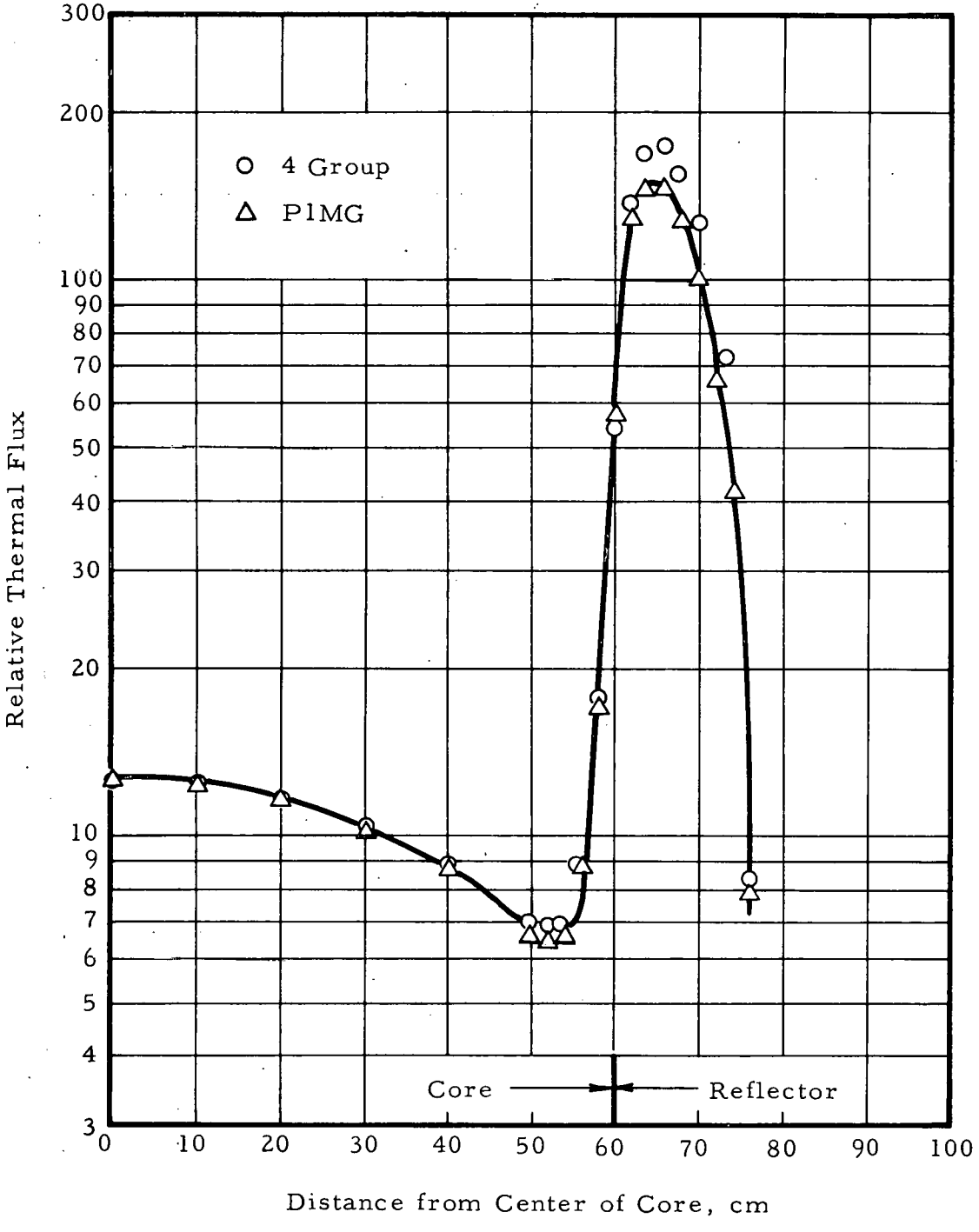

APPENDIX A
Computer Codes

THIS PAGE
WAS INTENTIONALLY
LEFT BLANK

APPENDIX A
Computer Codes

1. The RIP Program

1.1. Introduction

RIP is a general purpose resonance integral program, which analytically describes near-thermal, resonance, and high energy absorptions for use in multigroup spectrum and criticality codes. The program package contains subroutines for averaging cross sections over an arbitrary group structure, for calculating the resonance integral for a set of resolved peaks, and for calculating L-factors for input to MUFT, PIMG, and P3MG programs. The method has been programmed for use on the Philco 2000 computer.

For a particular resonance absorber, the RIP program treats absorption in four distinct energy ranges:

1. From the thermal cutoff to the energy of the first resolved resonance peak, the absorption cross section is treated as 1/v. The average cross section for groups lying in this range is computed for a 1/E flux spectrum.

2. In the resolved resonance region, Wigner's approximation for the resonance escape probability is used to obtain the effective resonance integral for a narrow, isolated resonance peak. For any specified absorber, widely separated peaks and a constant lethargy-dependent collision density between the peaks are assumed. Doppler-broadening correction factors are obtained numerically from a 1056-entry table compiled from the work of Dresner, Nordheim, and Nather. For heterogeneous (lump) calculations, a modified form of Rothenstein's correction for use of the rational approximation to the escape probability (P_o) is applied. Both the narrow resonance and narrow resonance-infinite absorber approximations are available in either homogeneous or

heterogeneous resonance integral problems. Interference between potential and resonance scattering in the absorber is neglected. The total resonance integral for a group is the sum of the resonance integrals for the resolved peaks lying within the group bounds.

3. For a given energy within a group in the unresolved resonance region, the Doppler-broadening function is averaged over the statistical distribution of neutron widths as given by Porter and Thomas An integration over energy between the group bounds using the narrow resonance approximation is then performed to yield the effective resonance integral for the group. Averaging of the Doppler-broadening function and integration over the group are performed numerically using a 10-point Laguerre-Gauss quadrature formula and a four-point Newton-Cotes formula, respectively.

4. In the region above the unresolved resonances, designated the high energy region, smooth absorption cross sections are assumed to be available. The resonance integral for groups in this region is the infinitely dilute value obtained by integrating the cross section over the group.

The limits for these four regions are arbitrary. All four regions are included to permit computation of a complete resonance absorption distribution function, a ψ-set, for input to BPG, a one-dimensional, multigroup code, which solves the transport equation in the P_l or B_1 approximation. This ψ-set describes the smooth absorption cross section in the 1/v and high energy regions and the fractional resonance absorption for each group in the resolved and unresolved regions.

In the MUFT and PIMG codes a homogeneous, un-Doppler broadened treatment of resonance absorption is available. To correct this approach for practical application of the codes, provision is made for modifying this treatment with the use of L-factors, which essentially divide out the code-generated resonance integral and allow the insertion of the correct region-, element-, group-, and peak-dependent resonance integral. Assuming one pseudo-resonance peak in each group in which resonance absorption occurs, RIP computes the group-, element-, and region-dependent L-factor yielding the correct effective resonance

integral in MUFT and PIMG calculations. The pseudo-resonance peak is chosen to permit using a single library tape to apply these codes to a particular design problem. Changes in temperature, geometry, element composition, and concentration are added by inserting the appropriate L-factors on cards.

In addition to the ψ-set and L-factor calculations, RIP contains subroutines that allow the averaging of up to 400 cross section data points over an arbitrary multigroup structure and the calculation of the effective resonance integral for up to 100 separately designated resonance peaks in the manner discussed in the description of the second energy region.

1.2. The Resonance Absorption Distribution Function

The resonance absorption distribution function, referred to as the ψ-set, serves two purposes in the transport spectral codes at Babcock & Wilcox:

1. It describes the smooth absorption cross section of resonance absorbers in the region below the resolved resonances and above the unresolved resonances.
2. It is a measure of the fractional effective resonance integral in groups lying in the resolved and unresolved resonance regions.

In the process of generating a ψ-set for a specified temperature, geometry, and element composition, RIP traverses the four regions of absorption treating each region as described below.

1.2.1. The 1/v Region

In the 1/v region a smooth absorption cross section is provided for all groups up to and including the group containing the first resolved resonance. The absorption cross section in this range is assumed to be 1/v extending up from the value at 0.0253 ev, i.e.,

$$\sigma_a(E) = \frac{\sigma_a(E^*)\sqrt{E^*}}{\sqrt{E}}, \quad E^* = 0.0253 \text{ ev} \qquad \text{(A-1)}$$

Referring to Figure A-1, the average cross section in the group whose limits are E_i and E_{i+1} for a 1/E spectrum is then given by

$$\bar{\sigma}_a = \frac{\int_{E_i}^{E_{i+1}} \sigma_a(E) \frac{dE}{E}}{\int_{E_i}^{E_{i+1}} \frac{dE}{E}} \tag{A-2}$$

$$= \frac{2\sigma_a(E^*)\sqrt{E}^*}{\ell n \frac{E_{i+1}}{E_i}} \left(\frac{1}{\sqrt{E}_i} - \frac{1}{\sqrt{E}_{i+1}} \right) \tag{A-3}$$

For the group containing the first resolved peak, the average group absorption cross section is given by

$$\bar{\sigma}_a = \frac{2\sigma_a(E^*)\sqrt{E}^*}{\ell n \frac{E_{i+1}}{E_i}} \left(\frac{1}{\sqrt{E}_i} - \frac{1}{\sqrt{E}_1^r} \right) \tag{A-4}$$

where

E_1^r = energy of first resolved resonance at maximum cross section

In the 1/v region the value of the ψ-set is identical to the average group cross section value with the exception of the group containing the first resolved resonance. In this group the average group cross section is reported for input as a smooth absorption cross section and the ψ-set is computed as in the resolved resonance region.

1.2.2. The Resolved Resonance Region

With the assumption that the resonances in the fuel lump or mixture are narrow and widely separated, the effective resonance integral for homogeneous or heterogeneous systems in the narrow resonance (NR) or narrow resonance-infinite absorber approximations (NRIA) may be summarized as follows:[27]

$$I^{NR} = \int \frac{\sigma_a^F(u)}{1 + \frac{1}{\sigma_p^{(i)}}\left[\sigma_a^F(u) + \sigma_{Sr}^F(u)\right]}\,du \qquad \text{(A-5)}$$

where i = 1 for homogeneous and 3 for heterogeneous

$$I^{NRIA} = \int \frac{\sigma_a^F(u)}{1 + \frac{\sigma_a^F(u)}{\sigma_p^{(i)}(u)}}\,du \qquad \text{(A-6)}$$

where i = 2 for homogeneous and 4 for heterogeneous

and

$$\sigma_p^{(1)} = \sigma_p^F + \frac{1}{N_F}\sum_{j \pm F} N_j \sigma_s^j \qquad \text{(A-7)}$$

$$\sigma_p^{(2)} = \frac{1}{N_F}\sum_{j \pm F} N_j \sigma_s^j \qquad \text{(A-8)}$$

$$\sigma_p^{(3)} = \sigma_p^F + \frac{1}{N_F}\sum_{j \pm F} N_j \sigma_s^j + \frac{1}{N_F \bar{S}} \qquad \text{(A-9)}$$

$$\sigma_p^{(4)} = \frac{1}{N_F}\sum_{j \pm F} N_j \sigma_s^j + \frac{1}{N_F \bar{S}} \qquad \text{(A-10)}$$

where

σ_p^F = potential scattering cross section of the fuel

σ_s^j = scattering cross section of moderating materials in the lump or mixture ($j \neq F$)

$\bar{S}$ = effective chord length in the lump

In arriving at Equations A-5 and A-6 for the heterogeneous resonance integral, the following Wigner's rational approximation to the escape probability in the absorbing lump was employed:[28]

$$P_o = \frac{1}{1 + \bar{S}\Sigma_t(u)} \qquad \text{(A-11)}$$

This approximation tends to the correct limits for small and large values of $\overline{S}\Sigma_t(u)$; for intermediate values, the approximation is inaccurate. The correction which is applied to the resonance integral for this error is summarized in Equations A-41 and A-43. Interference between resonance and potential scattering has been neglected since its effect on the resonance integral is quite small.[29]

The resonance cross sections appearing in Equations A-5 and A-6 are given by the single level Breit-Wigner formula.[30]

$$\sigma_a(E_r) = \frac{\Pi}{k^2} g_J \frac{\Gamma_n \Gamma_r}{(E_r - E_o)^2 + \left(\frac{\Gamma}{2}\right)^2} \tag{A-12}$$

$$\sigma_{sr}(E_r) = \frac{\Pi}{k^2} g_J \frac{\Gamma_n^2}{(E_r - E_o)^2 + \left(\frac{\Gamma}{2}\right)^2} \tag{A-13}$$

where

k = wave number of the neutron in the neutron-nucleus center-of-mass coordinate system

E_o = position of the resonance level

g_J = statistical spin factor = $\frac{2j+1}{2(2I+1)}$

J = spin quantum number of the compound nucleus formed by the target nucleus and the neutron

I = spin quantum number of the target nucleus

Γ_n, Γ_γ, Γ = neutron, radiative, and total widths of the level, respectively

E_r = kinetic energy associated with the relative velocity between neutron and nucleus

The potential scattering cross section of the absorber σ_p^F is energy independent in the resonance energy region. In Equations A-36 and A-37 we introduce the total resonance cross section when $E_r = E_o$, denoted by σ_o:

$$\sigma_o = \frac{4\Pi}{k^2} g_J \frac{\Gamma_n}{\Gamma} = \frac{2.6037 \times 10^6}{E_o(\text{ev})} \frac{\Gamma_n}{\Gamma} g_J \text{ (barns)} \tag{A-14}$$

Equations A-12 and A-13 may then be written:

$$\sigma_a(E_r) = \frac{\frac{\sigma_o \Gamma_\gamma}{\Gamma}}{1 + \left(\frac{E_r - E_o}{\frac{\Gamma}{2}}\right)^2} \tag{A-15}$$

$$\sigma_{sr}(E_r) = \frac{\frac{\sigma_o \Gamma_n}{\Gamma}}{1 + \left(\frac{E_r - E_o}{\frac{\Gamma}{2}}\right)^2} \tag{A-16}$$

If the target nuclei were stationary (T in degrees Kelvin), E_r would simply become E, the neutron energy. The target nuclei, however, are actually in thermal motion, and this motion creates the "Doppler effect" in resonance absorption phenomena. With

M = mass of absorber nucleus

m = neutron mass

$\overline{V}$ = velocity of the target nucleus

$\overline{v}$ = velocity of the neutron

$$A = \frac{M}{m}$$

the relative energy, E_r, associated with the velocity, $\overline{v} - \overline{V}$, in the center-of-mass coordinate system is given by

$$E_r = \frac{1}{2} M_o \, |\overline{v} - \overline{V}|^2$$

where M_o = neutron reduced mass = $\frac{A}{A+1} m$

Referring to Figure A-2, we see that

$$V_r^2 = v^2 + V^2 - 2Vv \cos \Theta$$

In most practical situations $V << v$; hence, we may take

$$\text{Cos } \Theta \approx 1, \frac{V}{v} \approx 0$$

and write the relative energy as

$$E_r = \frac{1}{2} M_o v^2 - M_o V v + \frac{1}{2} M_o V^2$$

$$= \frac{1}{2} M_o v^2 - M_o V v \left(1 - \frac{1}{2} \frac{V}{v}\right)$$

$$\approx \frac{1}{2} M_o v^2 - M_o V v = E - (2M_o E)^{1/2} V \qquad \text{(A-17)}$$

If the speeds of the capturing nuclei are described by a Maxwellian distribution,

$$P(V)\,dV = \left(\frac{M}{2\Pi kT}\right)^{1/2} e^{-MV^2/2kT}\,dV \qquad \text{(A-18)}$$

The probability that the relative energy will have a given value E_r when the neutron energy is E can be obtained by inserting into the right side of Equation A-18 the expression for V given by Equation A-17. With

$$V = \frac{E - E_r}{(2M_o E)^{1/2}} \text{ and } dV = -\frac{dE_r}{(2M_o E)^{1/2}}$$

we obtain

$$P(E_r)\,dE_r = \left(\frac{4\Pi M_o E k T}{M}\right)^{1/2} \exp\left\{-\frac{(E_r - E)^2}{\frac{4M_o E k T}{M}}\right\} \qquad \text{(A-19)}$$

Since the resonances are narrow, we may take $E \approx E_o$, defining

$$\Delta = \left(\frac{4M_o E_o k T}{M}\right)^{1/2} \qquad \text{(A-20)}$$

as the "Doppler width" of the resonances. We may then write Equation A-19 as

$$P(E_r)\,dE_r = \frac{\Pi^{-1/2}}{\Delta} \exp\left\{-\frac{(E_r - E)}{\Delta^2}\right\} dE_r \qquad \text{(A-21)}$$

The effective cross section for any neutron-nucleus interaction is given by

$$\sigma(E) = \int_{-\infty}^{\infty} \sigma(E_r)\, P(E_r)\, dE_r \qquad \text{(A-22)}$$

Consider, for example, the absorption cross section given in Equation A-15. The effective (Doppler broadened) cross section is obtained from Equation A-22 as follows:

$$\sigma_a(E) = \frac{\sigma_o \Gamma}{\Pi^{1/2} \Gamma} \int_{-\infty}^{\infty} \frac{e^{\frac{-(E_r - E)^2}{\Delta^2}}}{1 + \frac{(E_r - E_o)^2}{\left(\frac{\Gamma}{2}\right)^2}} \frac{dE_r}{\Delta} \qquad \text{(A-23)}$$

We define

$$y = \frac{E_r - E_o}{\frac{\Gamma}{2}}$$

$$\Theta = \frac{\Gamma}{\Delta} = \frac{\text{Natural width}}{\text{Doppler width}}$$

$$x = \frac{E - E_o}{\frac{\Gamma}{2}}$$

so that

$$E_r - E = \frac{\Gamma}{2}(y - x)$$

$$\frac{dE_r}{\Delta} = \frac{\Theta}{2} dy$$

Equation A-23 then becomes

$$\sigma_a(E) = \frac{\sigma_o \Gamma_\gamma}{\Gamma} \frac{\Theta}{2\sqrt{\Pi}} \int_{-\infty}^{\infty} \frac{e^{-1/4\Theta^2 (y-x)^2}}{1 + y^2} dy = \frac{\sigma_o \Gamma_\gamma}{\Gamma} \psi(\Theta, x) \qquad \text{(A-24)}$$

In the above development we have neglected the energy variation of σ_o and Γ since the resonances are narrow. The function $\psi(\Theta, x)$ is called the Doppler-broadened line shape or Voigt profile. The transformation from the center-of-mass coordinate system back to the laboratory system affects only Δ, which is now given by

$$\Delta = \left(\frac{4kTE_o}{A}\right)^{1/2} \qquad \text{(A-25)}$$

Note that the un-Doppler broadened cross section is given by

$$\sigma_a(E) = \frac{\sigma_o \Gamma_\gamma}{\Gamma}\left(\frac{1}{1+x^2}\right)$$

The evaluation of the resonance integrals can now proceed in a straightforward manner. With

$$\sigma_a^F = \frac{\sigma_o \Gamma_\gamma}{\Gamma}\,\psi(\Theta, x)$$

$$\sigma_{sr}^F = \frac{\sigma_o \Gamma_n}{\Gamma}\,\psi(\Theta, x)$$

$$x = \frac{E - E_o}{\frac{\Gamma}{2}},\quad dx = \frac{2}{\Gamma}\,dE,\quad \frac{dE}{E} = \frac{dE}{E_o}$$

The NR approximation given by Equation A-5 may now be written

$$I^{NR} = \int_{peak} \frac{\frac{\sigma_o \Gamma_\gamma}{\Gamma}\psi(\Theta, x)}{1 + \frac{\sigma_o}{\sigma_p^{(i)}}\psi(\Theta, x)}\,dx$$

$$= \frac{\sigma_p^{(i)} \Gamma_\gamma}{E_o} \int_{-\infty}^{\infty} \frac{\psi(\Theta, x)}{\beta + \psi(\Theta, x)}\,dx$$

$$= \frac{\sigma_p^{(i)} \Gamma_\gamma}{E_o}\,J(\Theta, \beta) \qquad \text{(A-26)}$$

Since we are dealing with narrow, widely separated resonances, the integration over the peak may be extended from $-\infty$ to ∞. Similarly, the narrow resonance-infinite absorber approximation is given by

$$I^{NRIA} = \int_{-\infty}^{\infty} \frac{\frac{\sigma_o \Gamma_\gamma}{\Gamma}\psi(\Theta, x)}{1 + \frac{\sigma_o \Gamma_\gamma}{\Gamma}\psi(\Theta, x)}\,\frac{dE}{E} \qquad \text{(A-27)}$$

$$\sigma_p^{(i)}$$

With

$$\tau = \frac{\sigma_p^{(i)} \Gamma_\gamma}{\sigma_o \Gamma}$$

Equation A-27 becomes

$$I^{NRIA} = \frac{\sigma_p^{(i)} \Gamma}{E_o} J(\Theta, \tau) \tag{A-28}$$

where

$$J(\Theta,\tau) = \int_{-\infty}^{\infty} \frac{\psi(\Theta, x)}{\tau + \psi(\Theta, x)} dx \tag{A-29}$$

The function $J(\Theta,\tau)$ is called the "Doppler broadening function" and has been studied in considerable detail by Nordheim[31]. A compilation of the $J(\Theta,\tau)$ values used in RIP appears in Appendix B. The properties of the function which are used by RIP for Θ and $\beta(\tau)$ values outside the range of the tables are the following:

1. For $\Theta > 1$

$$J(\Theta, \beta) \approx \frac{\frac{\Pi}{2}}{\sqrt{\beta(1+\beta)}} \tag{A-30}$$

which corresponds to the case T = 0 °K.

2. For large β

$$J(\Theta, \beta) \approx \frac{\Pi}{2\beta}$$

which corresponds to the infinitely dilute case yielding

$$I_\infty = \frac{\Pi}{2} \frac{\sigma_o \Gamma_\gamma}{E_o} \tag{A-31}$$

3. For $\Theta = 0$

$$J(0, \beta) = \frac{\Pi}{2\beta} \tag{A-32}$$

Values of $J(\Theta,\beta)$ are listed in the tables in terms of the variables Θ and $K(\Theta)$, where

$$K(\Theta) = \frac{\ell n\beta + 5\ \ell n\ 10}{\ell n\ 2} \tag{A-33}$$

Interpolation on the Θ variable is accomplished with a five-point Newton's divided difference interpolation formula; i.e., given values of Θ and $K(\Theta)$, we interpolate for $J\left(\Theta, K_i(\Theta)\right)$ and $J\left(\Theta, K_{i+1}(\Theta)\right)$ where $K_i \leq K \leq K_{i+1}$. Then, assuming that $J\left(\Theta, K(\Theta)\right) = C_1 e^{-C_2 K(\Theta)}$, we arrive at the following value for the Doppler function:[32]

$$J\left(\Theta, K(\Theta)\right) = J\left(\Theta, K_i(\Theta)\right) \exp\left\{\frac{K_i(\Theta) - K(\Theta)}{K_i(\Theta) - K_{i+1}(\Theta)}\ \ell n\ \frac{J(0), K_{i+1}(\Theta)}{J\left(\Theta, K_i(\Theta)\right)}\right\} \tag{A-34}$$

In RIP, the resonance integrals given by Equations A-26 and A-27 are corrected for use of the rational approximation to the escape probability. This is accomplished using a modified form of the correction factor reported by Rothenstein on page 167 of Reference 29. The final equations programmed for RIP then assume the following form:

1. Infinitely dilute resonance integral

$$I_\infty = \frac{\Pi}{2}\frac{\sigma_o \Gamma_\gamma}{E_o} \tag{A-35}$$

$$\sigma_o = \frac{4\Pi}{K^2}\frac{\Gamma_n}{\Gamma} g_J$$

2. Homogeneous - NR approximation

$$I = \frac{\sigma_p^{(1)}\Gamma_\gamma}{E_o}\ J(\Theta,\beta) \tag{A-36}$$

$$\Theta = \left(\frac{A\Gamma^2}{4KTE_o}\right)^{1/2} = \left(\frac{A\Gamma^2}{3.44656 \times 10^{-4} \times E_o(ev) \times T(^\circ K)}\right)^{1/2} \tag{A-37}$$

$$\beta = \frac{\sigma_p^{(1)}}{\sigma_o}$$

$$\sigma_p^{(1)} = \sigma_p^{(F)} + \frac{1}{N_F} \sum_{j \neq F} N_j \sigma_s^j$$

3. Homogeneous - NRIA approximation

$$I = \frac{\sigma_p^{(2)} \Gamma_\gamma}{E_o} J(\Theta, \tau) \tag{A-38}$$

$$\tau = \frac{\sigma_p^{(2)} \Gamma}{\sigma_o \Gamma_\gamma}$$

$$\sigma_p^{(2)} = \frac{1}{N_F} \sum_{j \neq F} N_j \sigma_s^j \tag{A-39}$$

4. Heterogeneous - NR approximation

$$I = \frac{\sigma_p^{(3)} \Gamma_\gamma}{E_o} J(\Theta, \beta^*) + \Delta I_G^{(1)} \tag{A-40}$$

$$\beta^* = \frac{\sigma_p^{(3)}}{\sigma_o}, \quad \sigma_p^{(3)} = \sigma_p^F + \frac{1}{N_F} \sum_{j \neq F} N_j \sigma_s^j + \frac{1}{N_F \bar{S}}$$

where

N_F = number density of resonance absorber in the lump

N_j = number density of moderating elements in the lump

$\bar{S} = 4V/\gamma S$ = effective chord length

$$\Delta I_G^{(1)} = \frac{I_1}{2(K+1)^2 \left\{ 1 + \sqrt{\frac{K+3}{\gamma}} \Big/ \sqrt{K+1} \right\}^2} \tag{A-41}$$

$$I_1 = \frac{I_\infty}{(1+\delta)^{1/2}}, \quad K = \frac{N_F \bar{S} \sigma_p^F}{1 + \bar{S} \sum_{j \neq F} N_j \sigma_s^j}$$

$$\delta = \frac{N_F \bar{S} \sigma_o}{1 + \bar{S} \sum_{j \neq F} N_j \sigma_s^j + N_F \sigma_p^F \bar{S}}$$

5. Heterogeneous - NRIA approximation

$$I = \frac{\sigma_p^{(4)}\Gamma}{E_o} J(\Theta,\tau^*) + \Delta I_G^{(2)} \qquad \text{(A-42)}$$

$$\tau^* = \frac{\sigma_p^{(4)}\Gamma}{\sigma_o \Gamma_\gamma}$$

$$\sigma_p^{(4)} = \frac{1}{N_F} \sum_{j \neq F} N_j \sigma_s^j + \frac{1}{N_F \bar{S}}$$

$$\Delta I_G^{(2)} = \frac{I_2}{\left\{ \left(\frac{\Gamma}{\Gamma_\gamma} \right)^{1/2} + \left(K + \frac{3}{\gamma} \right)^{1/2} \right\}^2} \qquad \text{(A-43)}$$

$$I_2 = \frac{I_\infty}{(1+\Delta)^{1/2}}$$

$$\Delta = \frac{N_F \bar{S} \sigma_o}{1 + \bar{S} \sum_{j \neq F} N_j \sigma_s^{(j)}}$$

In the heterogeneous equations, $\Delta I_G^{(1)}$ and $\Delta I_G^{(2)}$ represent the correction terms for use of the rational approximation for the escape probability P_o.

RIP uses the foregoing equations to compute the effective resonance integral for up to 100 separately designated peaks. The computation may be performed independent of a multigroup structure using the "Resolved Resonance Subroutine". For the ψ-set the computation is performed for each peak in a particular group, and the sum of the individual resonance integrals is taken as the resonance integral for the group, i.e.,

$$R_j = \sum_i R_{ij}$$

where R_j = group resonance integral

R_{ij} = resonance integral of peak with index i in group j

RIP may also be used for computing a fission rather than an absorption resonance integral Quantities retained for print-out and for use in the ψ-set calculation are:

1. I_{∞}^{i}
2. $J^{i}(\Theta, \beta)$
3. $\Delta I_{G,i}$
4. R_{j}^{i}
5. $\sum_{i} R_{ij}$

1.2.3. The Unresolved Resonance Region

In the unresolved resonance region the resonance peaks are assumed to be distributed with an average spacing D. Thus, a range ΔE in the unresolved region would contain $\Delta E/D$ resonance peaks. The radiative level width, Γ_{γ}, is assumed to be constant for the unresolved resonances, but the neutron level widths are assumed to be statistically distributed in a chi-squared distribution of one degree of freedom. This distribution is given by Porter and Thomas[33] as

$$(y)\, dy = \frac{1}{\sqrt{2\Pi}} \frac{e^{-y/2}}{\sqrt{y}} dy$$

where

$$y = \Gamma_{n}^{o} / \langle \Gamma_{n}^{o} \rangle$$

Γ_{n}^{o} = reduced neutron level width = $\Gamma_{n} / \sqrt{E}$

The resonance integral for a peak in the unresolved resonance range is given by the narrow resonance approximation as

$$I = \frac{\sigma_{p}^{(i)} \Gamma_{\gamma}}{E_{o}} J(\Theta, \beta), \quad \beta = \frac{\sigma_{p}^{(i)}}{\sigma_{o}}$$

The contribution, ΔI^*, to the total resonance integral, I^*, in a small range E around E_o is then

$$\Delta I^* = \frac{\sigma_p^{(i)} \Gamma_\gamma}{E_o} < J(\Theta, \beta) > \frac{\Delta E}{D}$$

where the brackets denote an average to be taken with respect to the statistical distribution of reduced neutron level widths. The dependence of Θ and β on y is easily shown to be

$$\Theta(y) = \left(\frac{A}{KT}\right)^{1/2} \left(y < \Gamma_n^o > + \frac{\Gamma_\gamma}{\sqrt{E}} \right) \tag{A-44}$$

$$\beta(y) = \frac{\sigma_p^{(i)}}{2.6037 \times 10^6 \times g_J} \left(E + \frac{\Gamma_\gamma \sqrt{E}}{y < \Gamma_n^o >} \right) \tag{A-45}$$

At a given energy, therefore, the Doppler broadening function is averaged as follows

$$\overline{J}(E) = \frac{1}{\sqrt{2\Pi}} \int_o^\infty \frac{e^{-y/2}}{\sqrt{y}} J\Big(\Theta(y),\ \beta(y)\Big)\, dy = \frac{1}{\sqrt{\Pi}} \int_o^\infty \frac{e^{-X}}{\sqrt{X}} J\Big(\Theta(X), \beta(X)\Big)\, dy \tag{A-46}$$

where

$$X = \frac{y}{2}$$

The total resonance integral for a range E_i to E_{i+1} in the unresolved range is then given by

$$I(E_i, E_{i+1}) = \frac{\sigma_p^{(i)} \Gamma_\gamma}{D} \int_{E_i}^{E_{i+1}} \frac{dE}{E} \frac{1}{\sqrt{\Pi}} \int_o^\infty \frac{e^{-y}}{\sqrt{X}} J\Big(\Theta(X),\ \beta(X)\Big)\, dX \tag{A-47}$$

$$= \frac{\sigma_p^{(i)}}{D} \Gamma_\gamma \int_{E_i}^{E_{i+1}} \overline{J}(E) \frac{dE}{E} \tag{A-48}$$

RIP performs the averaging of the Doppler broadening function with the aid of a 10-point Laguerre-Gauss quadrature. Equation A-46 is then replaced by

$$\bar{J}(E) = \frac{1}{\sqrt{\Pi}} \sum_{\ell=1}^{10} H_\ell f(X_\ell) \qquad \text{(A-49)}$$

where $f(X_\ell) = J\Big(\Theta(X_\ell), \beta(X_\ell)\Big)$

X_ℓ, H_ℓ = abscissas and weights for the Laguerre-Gauss quadrature, respectively

The integration over energy in the interval E_i to E_{i+1} is performed using a four-point Newton-Cotes integration procedure to yield

$$\int_{E_i}^{E_{i+1}} \bar{J}(E) \frac{dE}{E} = \frac{3}{8} h \, (f_0 + 3f_1 + 3f_2 + f_3) \qquad \text{(A-50)}$$

where $h = \dfrac{E_{i+1} - E_i}{3}$

$f_n = \left[\dfrac{\bar{J}(E)}{E}\right] E = E_i + nh$ where $n = 0, 1, 2, 3$

RIP first examines the width of the energy integration interval to determine the values of E to be used in the Newton-Cotes integration. Then, the function $\bar{J}(E)$ is computed from Equation A-49 for each E required.

Referring to Figure A-3, we see that the total unresolved resonance integral for the multigroup structure illustrated is given by

$$I = \frac{\sigma_p^{(i)} \Gamma_\gamma}{D} \left\{ \int_{E_B}^{E} \bar{J}(E) \frac{dE}{E} + \sum_{i=2}^{n-1} \left[\int_{E_i}^{E_{i+1}} \bar{J}(E) \frac{dE}{E} \right] + \int_{E_n}^{E_c} \bar{J}(E) \frac{dE}{E} \right\} \qquad \text{(A-51)}$$

where

E_1 = upper bound of group containing E_B

E_B = cutoff between resolved and unresolved resonance region

E_n = lower bound of group containing E_c

E_c = cutoff between unresolved and high energy regions

When E_B is not coincident with a group bound, both an unresolved and a resolved resonance contribution are computed for the group containing this cutoff. The ψ-set is then computed for the sum of these contributions.

If E_c lies within a group, an average group cross section is computed (see Section 1.2.4) for input to MUFT, PIMG, BPG, etc., as a smooth absorption cross section, the unresolved contribution is computed, and ψ for this group is formed as in the preceding groups.

1.2.4. The High Energy Region

In the high energy region, smooth absorption cross sections are assumed to be available either in the form of point data or as actual group cross sections. If point data is supplied, RIP averages the data over the multigroup structure assuming a 1/E flux spectrum. This averaging is performed by a subroutine which may be considered separate from the main program and used as a cross section averaging package. The high energy region begins at E_c, the cutoff of the unresolved resonance region, and extends to E_D, the upper bound of the first (highest energy) group.

Between data points the cross section is assumed to be given by

$$\ell n\, \sigma(E) = A + B\, \ell n\, E \tag{A-52}$$

The first task in the averaging procedure is to obtain the cross sections at the upper and lower bounds of the group by interpolation. Referring to Figure A-4 we may then write:

$$\ell n\, \sigma(E_i^n) = A + B\, \ell n\, E_i^n \tag{A-53}$$

$$\ell n\, \sigma(E_i^{n+1}) = A + B\, \ell n\, E_i^{n+1} \tag{A-54}$$

Solving for A and B and inserting into Equation A-52 yields

$$\ell n\, \sigma(E_i) = \ell n(\sigma_i^{n+1}) \left[\frac{\ell n\left(E_i/E_i^n\right)}{\ell n\left(E_i^{n+1}/E_i^n\right)}\right] + \ell n\, \sigma(E_i^n) \left[\frac{\ell n\left(E_i^{n+1}/E_i\right)}{\ell n\left(E_i^{n+1}/E_i^n\right)}\right] \tag{A-55}$$

Consider the typical group shown in Figure A-5 with the average cross section given by

$$\bar{\sigma}_i = \frac{\int_{E_i}^{E_{i+1}} \sigma(E)\, \frac{dE}{E}}{\int_{E_i}^{E_{i+1}} \frac{dE}{E}} \tag{A-56}$$

It is easily shown that the average group cross section is

$$\bar{\sigma}_i = \left\{ \left[\sigma(E_1) - \sigma(E_i)\right] \frac{\ell n(E_1/E_i)}{\ell n\left[\sigma(E_1)/\sigma(E_i)\right]} + \sum_{j=1}^{n-1} \left[\sigma(E_{j+1}) - \sigma(E_j)\right] \frac{\ell n(E_{j+1}/E_j)}{\ell n\left[\sigma(E_{j+1})/\sigma(E_j)\right]} \right.$$

$$\left. + \sigma(E_{j+1}) - \sigma(E_n) \frac{\ell n(E_{i+1}/E_n)}{\ell n\left[\sigma(E_{j+1})/\sigma(E_j)\right]} \right\} \frac{1}{\ell n\left(\frac{E_{i+1}}{E_i}\right)} \qquad \text{(A-57)}$$

In the group containing E_c, we let $E_i = E_c$ in the first term of Equation A-57. The group bound at E_D (normally at 10 mev) must correspond to the last data point. There must also be a data point at E_c. If average group cross sections are supplied, the above averaging procedure is bypassed, and the ψ values for groups in the high energy region are computed from the input cross sections as explained in Section 1.3.

For a simple cross section averaging application of the subroutine, the group boundaries, point data, and beginning (E_c) and end (E_D) of the point data range must be supplied. E_D must correspond to the upper bound of the highest energy group.

1.3. ψ-Set Normalization

In the multigroup transport codes at Babcock & Wilcox, the resonance integral for a particular group in the resolved or unresolved resonance region is given by:

$$I_j = \psi_j R^* \Delta u_j \qquad \text{(A-58)}$$

where ψ_j = ψ value for group j

R^* = experimental or calculated total resonance integral (excluding 1/v contribution) to which ψ is normalized

Δu_j = lethargy width of group j

The normalization of ψ forces the calculated total resonance integral in the unresolved range to agree with an experimental value assuming that the high energy resonance integral, given by

$$I = \sum_{j=\ell+1}^{1} \bar{\sigma}_a^j \Delta u_j \tag{A-59}$$

where group $\ell + 1$ is the group containing E_c, is identical in the calculated and experimental total resonance integrals. For any group containing a resolved or unresolved resonance contribution, therefore, the ψ value is given by

$$\psi_j = \left(\frac{R^* - \sum_{j=\ell+1}^{1} \bar{\sigma}_a^j \Delta u_j}{\sum_{j=m}^{\ell+1} R_j} \right) \left(\frac{R_j}{\Delta u_j} \right) \frac{1}{R^*} \tag{A-60}$$

where

m = group containing E_r, energy of the first resolved peak

R_j = resonance integral (resolved and unresolved) in group j

If normalization to the calculated resonance integral is specified (this option is available by inserting zero for R^* on Figure A-6), the ψ value is simply

$$\psi_j = \left(\frac{R_j}{\Delta u_j} \right) \frac{1}{R^*} \tag{A-61}$$

In the high energy region, the smooth absorption cross section is also given in terms of a ψ value by defining

$$\psi_j = \frac{\bar{\sigma}_a^j}{R^*} \quad \text{where } j = 1, \ldots, \ell \tag{A-62}$$

It is easily seen that

$$\sum_{j=m}^{1} \psi_j \Delta u_j = 1$$

In the 1/v region, the ψ value is defined as

$$\psi_j = \bar{\sigma}_a^j \quad \text{where thermal cutoff} \leq j \leq m \tag{A-63}$$

1.4. The PIMG L-Factor Option

The resonance in the MUFT-4, PIMG, and P3MG codes uses the NR approximation in the homogeneous resonance integral described by Wigner. In addition, the un-Doppler broadened, Breit-Wigner single level equations are used to describe the resonance cross sections. These codes, however, provide for modifying this treatment by inserting a multiplying factor (i.e., an L-factor) in the exponent for p, the resonance escape probability, which is region, element, group, and peak dependent and is entered in the program on cards. The MUFT treatment restricts the number of peaks (and L-factors) to eight per group.

The expression for the resonance escape probability in the MUFT-4 approximation is given by:

$$P_m = \exp\left\{ -\sum_k L_{j,i}^{m,k} (\pi/2) \frac{M_i^{m,k}}{\bar{\xi}_j^m} \frac{1}{\sqrt{A_j^m \left[A_j^m + (r_a)_j^{m,k} \right]}} \right\} \qquad \text{(A-64)}$$

where m, k, j, i = group, peak, region, and element indices, respectively

$$M_i^{m,k} = \frac{\sigma_o \Gamma_\gamma}{E_o} = \frac{2}{\Pi} I_\infty^k$$

$$(r_a)_i^{m,k} = \frac{\sigma_o \Gamma_a}{\Gamma}$$

$$A_j^m = \frac{1}{N_F} \sum_i N_i (\sigma_s)_i^{m-1} \qquad \text{(summation includes absorber)}$$

$$L_{j,i}^{m,k} = \text{L-factor}$$

The qualities $M_i^{m,k}$ and $(r_a)_i^{m,k}$ are resonance parameters on the library tape. The resonance escape probability in the Babcock & Wilcox codes is given by

$$P_m = \exp\left\{ -\frac{1}{A_j^{m+1} \bar{\xi}_j^m} \psi_j R^* \Delta u_j \right\} \qquad \text{(A-65)}$$

where $A_j^{m+1} = \frac{1}{N_F} \sum_i N_i (\sigma_s)_i^m$

To generate a library tape that need not be changed for changes in temperature, geometry, and element composition and, in addition, to provide for more than eight peaks per group, the following procedure was adopted:

1. We assume that each group containing a resonance absorption contribution contains one psuedoresonance peak per group. This peak has the property $(r_a)_i^{m,k} = 0$ and $M_i^{m,k} = \sum_k M_i^{m,k}$, i.e., the infinitely dilute resonance integral of the pseudopeak is equal to the sum of the infinitely dilute values of the actual peaks in the group. This definition for $M_i^{m,k}$ applies only in the groups for which resonance absorption is due wholly to resolved peaks. We let $M_i^{m,k} = 10$ for any group containing an unresolved contribution.

2. With $(r_a)_i^{m,k} = 0$, Equation A-64 becomes

$$P_m = \exp\left\{ - L_{j,i}^{m,k} \left(\frac{\Pi}{2}\right) \frac{M_i^{m,k}}{\overline{\xi}_j^m A_j^m} \right\} \tag{A-66}$$

RIP computes the quantity

$$(RI)_{PIMG} = \frac{(\Pi/2) M_i^{m,k}}{\overline{\xi}_j^m A_j^m} \tag{A-67}$$

where all elements in the region are treated as moderating elements in the computation of $\overline{\xi}_j^m A_j^m$.

3. The quantity

$$(RI)_{BPG} = \frac{\psi_j R^* \Delta u_j}{\overline{\xi}_j^m A_j^{m+1}} \tag{A-68}$$

is then computed to give the BPG expression corresponding to Equation A-67.

4. The L-factor is then given by

$$L_{j,i}^{m,k} = \frac{(RI)_{BPG}}{(RI)_{PIMG}} \tag{A-69}$$

Homogeneous number densities are required, of course, for the PIMG calculation, and this calculation is available only when a ψ-set calculation is specified on the control card. Note that, if the problem under study consists of lumped absorbers so that the resonance integral is computed from the heterogeneous equations and L-factors are desired, heterogeneous number densities for the absorber and scattering elements in the lump must be specified as well as the homogeneous density of the absorber and scattering elements in the region.

2. The BPG-II Program

2.1. Introduction

The BPG code computes the spectrum and spectrum dependent properties of reactors and is particularly applicable to reactors with mixtures of H_2O and D_2O as moderator. Since slowing down with hydrogen moderator may be treated rigorously and since the Fermi age equation accurately treats heavy moderators such as carbon, the important innovations in this code deal with the transition from light to heavy scatterer and particularly with the treatment of moderation by deuterium.

The applicability of the Greuling-Goertzel equations and of an improved expansion of the scattering kernel to the analysis of the slowing down problem has been pointed out by several investigators.[34] In the BPG code, these equations in the B_1 expansion approximation have been formulated to obtain a multigroup, bare-reactor criticality calculation. The resulting neutron balance can in turn be used to obtain effective coefficients for few-group, many-region calculations in several spatial dimensions. For example, the four-group coefficients can be fed directly into the four-group code for one-dimensional calculations or into PFQ for two-dimensional calculations. The code formulation of BPG is similar to that of MUFT. BPG uses the consistent expansions of the scattering integral, and the Greuling-Goertzel equations are available in normal input for all elements up to mass 27.

2.2. The B_1 and P_1 Approximations with Anistropic Scattering

The BPG program utilizes either the B_1 or P_1 approximations to the neutron transport equation with the "extended" Greuling-Goertzel, Greuling-Goertzel, and Fermi age slowing-down approximations available for the light, intermediate, and heavy mass scatterers, respectively.

The fundamental equation solved in the BPG program is the one-dimensional, energy-dependent, neutron-transport equation in the form:

$$\mu \frac{d}{dX} \Phi(\mu, u, y) + \Sigma^T(u, X)\, \Phi(\mu, u, X) = 2\Pi \int_{u'} \int_{-1}^{1} d\mu\, du'\, \Sigma^o(\mu_o, u', X)$$

$$\times \Phi(\mu', u', X) + \frac{V}{2} f(u) \int_o^\infty du' \int_{-1}^{1} d\mu'\, \Sigma^F(u', X)$$

$$\times \Phi(\mu', u', X) + \frac{1}{2} \int_o^\infty du' \int_{-1}^{1} d\mu'\, \Sigma^I(u', \mu', X)\, \Phi(\mu', u', X) \qquad \text{(A-70)}$$

In the fission and inelastic scattering integrals, emission is assumed to be spherically symmetric in the laboratory system. The first order approximations to the solution of Equation A-70 yield the following:[35]

$$\Sigma^T(u)\, \phi_o(u) = \psi_o(u) G_o^o - \frac{dq_o}{du}(u) + iB\psi_1(u) + S + I \qquad \text{(A-71)}$$

$$\Sigma^T(u)\, h\psi_1(u) = \psi_1(u)\, G_1^o - \frac{dq_1}{du}(u) + i\frac{B}{3}\psi_o(u) \qquad \text{(A-72)}$$

$$q_o(u) + \lambda_o \frac{dq_o}{du}(u) = -G_o^1 \psi_o(u) \left(1 - \frac{d\lambda_o}{du}\right) \qquad \text{(A-73)}$$

$$q_i(u) + \lambda_1 \frac{dq_1}{du}(u) = -G_o^1 \psi_1(u) \left(1 - \frac{d\lambda_1}{du}\right) \qquad \text{(A-74)}$$

where ψ_o, ψ_1, and q_o, q_1 are the unknown fluxes and slowing down densities, respectively.

$$G_i^n(u) = \sum_{k=o}^{\infty} T_{ik}^n\, B_k^c(u) \qquad \text{(A-75)}$$

$$\lambda_i = -\frac{G_i^2}{G_i^1} \qquad \text{(A-76)}$$

The $B_k^c(u)$ are the Legendre coefficients of $\Sigma_s^c(\mu_c, u)$, the differential scattering cross section evaluated in the center-of-mass coordinate system, i.e.,

$$B_k^c(u) = 2\Pi \int_{-1}^{1} \Sigma^s(\mu_c, u)\, P_k(\mu_c)\, d\mu_c \qquad \text{(A-77)}$$

The T_{ik}^{n} are given by Reference 35:

$$T_{ik}^{n} = \frac{2k+1}{2(n!)} \int_{-1}^{1} P_i \left[\mu_o(\mu_c)\right] P_k(\mu_c) \left[-U(\mu_c)\right]^n d\mu_c \qquad \text{(A-78)}$$

In Equation A-72 the B_1 approximation is obtained when

$$h(u) = \frac{1}{3}\left[\frac{B}{\Sigma^T}\right]^2 \frac{\beta}{1-\beta} \qquad \text{(A-79)}$$

$$\beta = \frac{\Sigma^T(u)}{B} \tan^{-1}\left[\frac{B}{\Sigma^T(u)}\right]$$

For the P_1 approximation, $h(u) = 1$. Equations A-71 through A-74 comprise a system of differential equations in the dependent variable, u, the lethargy. They are solved on the computer using the multigroup approximation. In place of the point fluxes $\psi(u)$, a group flux ϕ_j is introduced. We take

$$\phi_j = \int_{u_{j-1}}^{u_j} \phi(u)\, du, \qquad \text{(A-80)}$$

$$J_j = -i \int_{u_{j-1}}^{u_j} \psi_1(u)\, du, \qquad \text{(A-81)}$$

$$S_j = \int_{u_{j-1}}^{u_j} S(u)\, du, \qquad \text{(A-82)}$$

$$I_j = \int_{u_{j-1}}^{u_j} I(u)\, du, \qquad \text{(A-83)}$$

$$\Sigma_j = \frac{1}{\Delta u_j} \int_{u_{j-1}}^{u_j} \Sigma(u)\, du, \qquad \text{(A-84)}$$

(where $u_j = u_j - u_{j-1}$, the above equation holds for A, S, I, F, and T)

$$q(u_j) = q_o(u_j), \qquad \text{(A-85)}$$

$$p(u_j) = -iq_1(u_j), \qquad \text{(A-86)}$$

$$h_j(B) = h(B, \Sigma_j^T), \tag{A-87}$$

$$\mu_j = \frac{1}{\Delta u_j} \int_{u_{j-1}}^{u_j} \frac{G_1^o(u)}{\Sigma^S(u)}\, du, \tag{A-88}$$

$$\xi_j = -\frac{1}{\Delta u_j} \int_{u_{j-1}}^{u_j} \frac{G_o^1}{\Sigma^S(u)}\, du, \tag{A-89}$$

$$\eta_j = -\frac{1}{\Delta u_j} \int_{u_{j-1}}^{u_j} \frac{G_1^1}{\Sigma^S(u)}\, du, \tag{A-90}$$

$$\Gamma_j = \frac{1}{\Delta u_j} \int_{u_{j-1}}^{u_j} \lambda_o(u)\, du, \text{ and} \tag{A-91}$$

$$Z_j = \frac{1}{\Delta u_j} \int_{u_{j-1}}^{u_j} \lambda_1(u)\, du. \tag{A-92}$$

These equations show that ϕ_j, J_j, S_j, and I_j are group quantities, which are integrated over a lethargy interval. On the other hand, q and p remain as quantities defined at a specific lethargy value. The remainder of the quantities are averages over a lethargy interval except that h_j is a function of the average value Σ_j^T.

We next integrate Equations A-70 through A-74 over the interval (u_{j-1}, u_j) and use approximations which involve replacing an unknown quantity by an average value. In most cases, the group quantity can be assumed to be positive (or negative) throughout the interval. Then using the mean value theorem of calculus, one gets, for example,

$$\int_{u_{j-1}}^{u_j} \Sigma^T(u)\, \phi(u) du = \Sigma^T(u^*) \int_{u_{j-1}}^{u_j} \phi(u)\, du,$$

where

$$u_{j-1} \leq u \leq u_j = \Sigma^T(u^*)\, \phi_j \approx \Sigma_j^T\, \phi_j$$

The approximation is seen to consist of using the average Σ_j^T in place of Σ^T at the unknown value u^*. In similar fashion, the other terms are approximated to give the system of multigroup equations:

$$(a)\quad BJ_j + (\Sigma_j^A + \Sigma_j^I)\,\phi_j + q(u_j) = q(u_{j-1}) + S_j + I_j,$$

$$(b)\quad \left[h_j\Sigma_j^T - \Sigma_j^S\,\mu_j\right] J_j - \frac{B}{3}\phi_j + p(u_j) = p(u_{j-1}),$$

$$(c)\quad -\xi_j\Sigma_j^S\left\{1 - \frac{1}{\Delta u_j}\left[\lambda_o(u_j) - \lambda_o(u_{j-1})\right]\right\}\phi_j + \left(\frac{\Delta u_j}{2} + \Gamma_j\right)q(u_j)$$

$$= \left(\Gamma_j - \frac{\Delta u_j}{2}\right)q(u_{j-1}),\ \text{and}$$

$$(d)\quad -\eta_j\Sigma_j^S\left\{1 - \frac{1}{\Delta u_j}\left[\lambda_1(u_j) - \lambda_1(u_{j-1})\right]\right\}J_j + \left(\frac{\Delta u_j}{2} + Z_j\right)p(u_j)$$

$$= \left(Z_j - \frac{\Delta u_j}{2}\right)p(u_{j-1}). \qquad \text{(A-93)}$$

The isotropic slowing-down density q(u) is described by two different models, which are:

1. The contribution due to elastic scattering of aluminum and elements lighter than aluminum may be represented by an equation of the form of Equation c in Group A-93 for each of such elements in the system. (Greuling-Goertzel slowing down model)

2. The contribution due to elastic scattering by elements heavier than aluminum is considered to be represented by the following expression, in which the contribution of all species heavier than aluminum are lumped as indicated by the subscript 'L.

$$q_F(u_j) = \frac{2}{\Delta u_j}\sum_L \xi_{Lj}N_L\Sigma_{Lj}^S\,\phi_j - q_F(u_{j-1}) \qquad \text{(A-94)}$$

(Fermi age model)

It is also possible to treat the lighter elements by this Fermi age model if the proper choice of input is chosen (as shown later).

The slowing-down densities for each element (by the model chosen for each element) are added to obtain the total isotropic slowing down density q(u).

The anisotropic slowing-down density has a contribution from only three elements: H, D, and B_e. This contribution is represented by Equation d of Group A-93, one such equation representing the anisotropic slowing-down density contributed by each of the elements of this type present in the system. The total of such contributions is represented by $p(u_j)$ in the second equation of the group. We now replace this symbol with $\sum_h p_h(u_j)$, where the subscript h refers to the elements H, D, and B_e.

Inelastic scattering slows neutrons down. Because this is treated in a discontinuous manner, the neutrons being slowed down inelastically are not included in the slowing-down density. Inelastic scattering into each lethargy group is represented by the term I_j in Equation a of Group A-93, which gives the neutrons inelastically scattered into the group from all lower lethargy groups In the same equation, the term $\Sigma_j^I \phi_j$ represents the neutrons removed from the group by inelastic scattering. Because the lethargy groups have finite width, not all the neutrons that undergo inelastic scattering are removed from the group. Therefore, this term must be corrected slightly, and this correction is incorporated in A_j. It is probable that an inelastically scattered neutron will lose enough energy to be removed from the group to a higher lethargy group. Thus, $\Sigma_j^I \phi_j$ now gives the number of neutrons inelastically scattered in a group, and $A_j \Sigma_j^I \phi_j$ now gives the number of neutrons removed from the group by inelastic scattering.

To simplify equations of Group A-93 we define

$$\Sigma_j^S \mu_j = \sum_k N_k M_{kj} \tag{A-95}$$

(a) $$\xi_{fj} \Sigma_{fj}^S \left\{ 1 - \frac{1}{\Delta u_j} \left[\lambda_{of}(u_j) - \lambda_{of}(u_{j-1}) \right] \right\} = N_f \Xi_{fj}^*$$

(b) $$\xi_{kj} \Sigma_{kj}^S = N_k \Xi_{kj} \tag{A-96}$$

$$\eta_{hj} \Sigma_{hj}^S \left\{ 1 - \frac{1}{\Delta u_j} \left[\lambda_{1h}(u_j) - \lambda_{1h}(u_{j-1}) \right] \right\} = N_h H_{hj} \tag{A-97}$$

where f implies the element aluminum or one of the elements lighter than aluminum, h refers to the elements H, D, or B_e, and N is the element number density.

The equations of Group A-93 are rewritten using the subscripts f and h to refer to the defined elements and an additional subscript k to refer to all elements. These are the BPG equations:

$$\text{(a)}\quad B J_j + (\Sigma_j^A + A_j \Sigma_j^I)\,\phi_j + \sum_f q_f(u_j) + q_F(u_j)$$

$$= S_j + I_j + \sum_f q_f(u_{j-1}) + q_F(u_{j-1}),$$

$$\text{(b)}\quad \left[h_j \Sigma_j^T - \sum_k N_k M_{kj}\right] J_j - \frac{B}{3}\phi_j + \sum_h p_h(u_j) = \sum_h p_h(u_{j-1}),$$

$$\text{(c)}\quad \left[\frac{\Delta u_j}{2} + \Gamma_{fj}\right] q_f(u_j) - N_f \Xi^*_{fj}\,\phi_j = \left[\Gamma_{fj} - \frac{\Delta u_j}{2}\right] q_f(u_{j-1}),$$

$$\text{(d)}\quad q_F(u_j) = \frac{2}{\Delta u_j} \sum_L N_L \Xi_{Lj}\,\phi_j - q_F(u_{j-1}),\ \text{and}$$

$$\text{(e)}\quad \left[\frac{\Delta u_j}{2} + Z_{hj}\right] p_h(u_j) - N_h H_{hj} J_j = \left[Z_{hj} - \frac{\Delta u_j}{2}\right] p_h(u_{j-1}), \qquad \text{(A-98)}$$

Equation c is used for each f element and Equation e is used for each h element. This system of equations is solved for the unknowns $J_j o_j$, $q_f(u_j)$, and $p_h(u_j)$ in the epithermal range. The following equations are added for the thermal range to complete the spectrum:

$$B J_{th} + \Sigma_{th}^A\,\phi_{th} = \sum_f q_f(u_{th}) + q_F(u_{th})$$

$$\left[\Sigma_{th}^T - \mu_{th}\,\Sigma_{th}^S - \frac{4}{5}(1 - \mu_{th})\,\Sigma_{th}^A\right] J_{th} - \frac{B}{3}\,\phi_{th} = \sum_h p_h(u_{th}) \qquad \text{(A-99)}$$

where μ_{th} is the thermal cutoff lethargy (upper lethargy bound of this last epithermal group).

2.3. Resonance Absorption in the Th^{232} and U^{238}

To allow for various degrees of self-shielding by Th^{232} and U^{238}, the program normalizes the absorption cross sections of these two materials so that their resonance integrals are made to agree with values specified in the problem input. This is accomplished by having normalized distribution functions $\psi_{02,i}$ and $\psi_{28,i}$, which are normalized in the sense that

$$\sum_{j=1}^{m} \psi_j \, \Delta u_j = 1$$

where m is the group containing the last resonance peak.

Three energy regions are considered by the code:

1. The high energy region where the absorption cross section varies slowly and energy groups j = 1 to j = ℓ - 1 are included.

2. The low energy region, between the lowest resonance energy and thermal energy, is assumed to have a cross section proportional to 1/v. Groups m + 1 through the last (including thermal) are in this region.

3. The resonance region includes both the resolved and unresolved resonances. It is assumed that self-shielding and Dancoff mutual shielding of the resonances occur uniformly in this region. Groups j = ℓ to j = m are included in this region. ℓ is chosen as a boundary between the unresolved resonance region and the high energy region, and m includes the lowest energy resolved resonance.

The resonance integral values R_{02} and R_{28} are then used to construct the group cross sections. These values are:

1. In the lethargy interval j = 1 to j = ℓ - 1,

$$\sigma_{ij}^{A} = R_i \psi_{ij} \text{ where } i = 02 \text{ or } 28. \qquad \text{(A-100)}$$

2. In the lethargy interval j = m + 1 to thermal,

$$\sigma_{ij}^{A} = \psi_{ij}. \qquad \text{(A-101)}$$

3. In the lethargy interval $j = \ell$ to $j = m$, it is necessary to modify Equation a of Group A-98 when either of the elements Th^{232} or U^{238} are present in the system. In this equation the absorption term is indicated by $\Sigma_j^A \phi_j$. The modification consists of separating the absorption into two components—smooth capture and resonance capture, so that

$$\text{Total absorption} = \Sigma_j^A \phi_j + (1 - P_j)\, q(u_{j-1}),$$

in which the term for smooth capture, $\Sigma_j^A \phi_j$, may contain contributions from Th^{232} and U^{238} as well as contributions of the other elements of the system. In this equation, P_j is the resonance escape probability and is given by the expression

$$P_j = P_{O2,j}\, P_{28,j}$$

where $P_{O2,j}$ or $P_{28,j}$ is taken as 1 if the element is not present in the system. This is defined by

$$P_{ij} = \exp\left[- \frac{1}{\sum_k N_k \Xi_{kj}} (N_i R_i \psi_{ij} \Delta u_j) \right] \qquad \text{(A-102)}$$

where

N_i = number density

ψ_{ij} = normalized distribution function obtained from RIP

Rewriting Equation a of Group A-98 to include this expression for absorption, we obtain

$$BJ_j + (\Sigma_j^A + A_j \Sigma_j^I)\, \phi_j + \sum_f q_f(u_j) + q_F(u_j) = S_j + I_j + P_j \left[\sum_f q_f(u_{j-1}) + q_F(u_{j-1}) \right]$$

This equation is substituted for Equation a of Group A-98 only in the groups in the interval including the Dancoff boundary, denoted by "ℓ", and the last resonance peak, denoted by "m", as indicated above.

2.4. Two-Group and Polygroup Parameters

The program computes a number of quantities related to the spectrum in addition to the spectrum itself. Some of these are related to the spectrum as a whole such as age, resonance escape probability, and cadmium ratios. Others are related to portions of the epithermal spectrum. These are called polygroup quantities.

The latter class includes polygroup coefficients. These are the coefficients to be used in the multiregion, several-group diffusion calculations, characterized by the following equations:

$$D_1 \Delta^2 \phi_1 - W_1 \phi_1 + \frac{1}{k_{eff}} \left[f_1 \phi_1 + f_2 \phi = + \ldots + f_N \phi_N \right] = 0$$

$$D_2 \Delta^2 \phi_2 - W_2 \phi_2 + \beta_1 \phi_1 = 0$$

$$D_N \Delta^2 \phi_N - W_N \phi_N + \beta_{N-1} \phi_{N-1} = 0$$

In defining the lethargy (or energy) boundaries of each of the groups of this polygroup representation, it is necessary to make a correspondence between each of these groups and the appropriate BPG multigroups. It is possible to compute coefficients for up to six such polygroups.

Figure A-1. Absorption Regions Examined by RIP

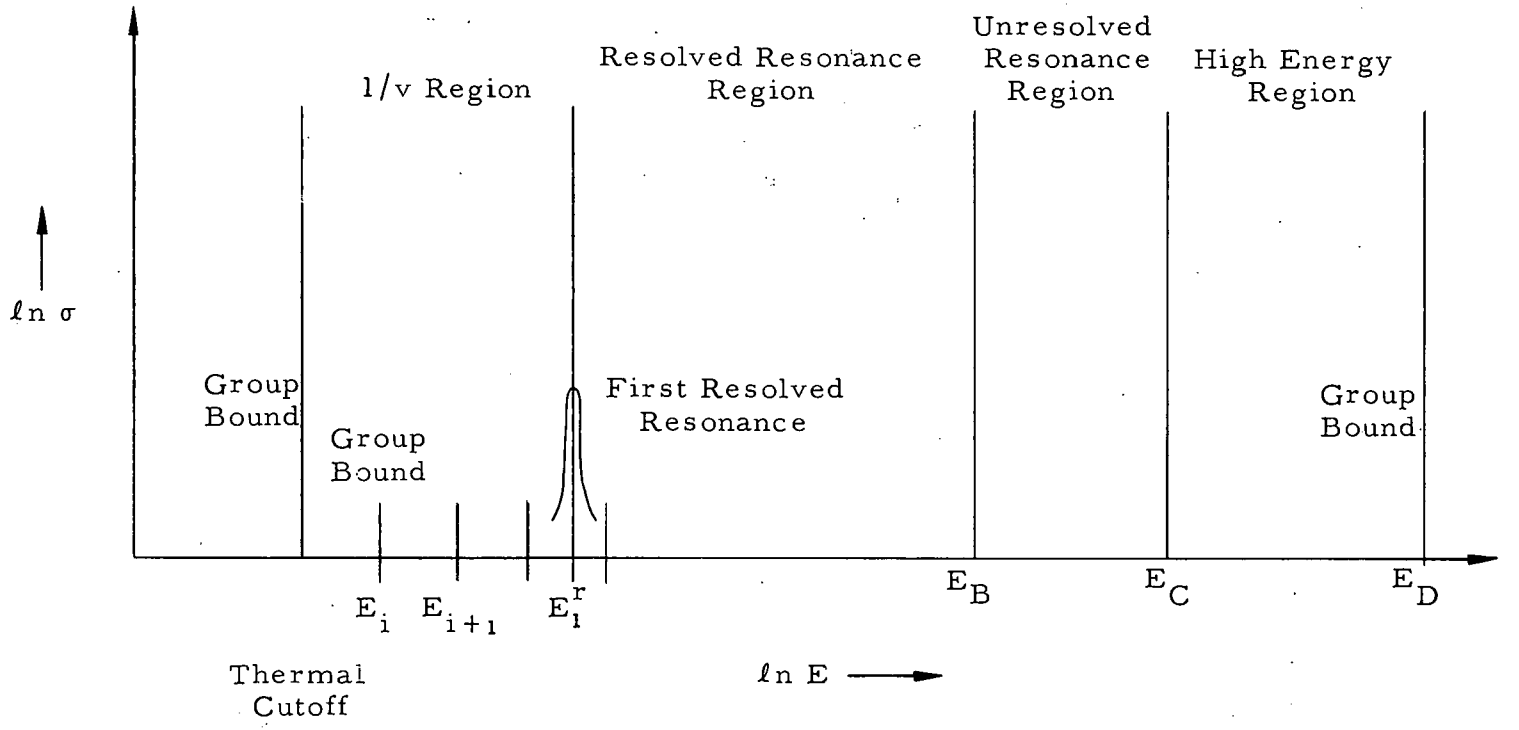

Figure A-2. Velocity Vectors

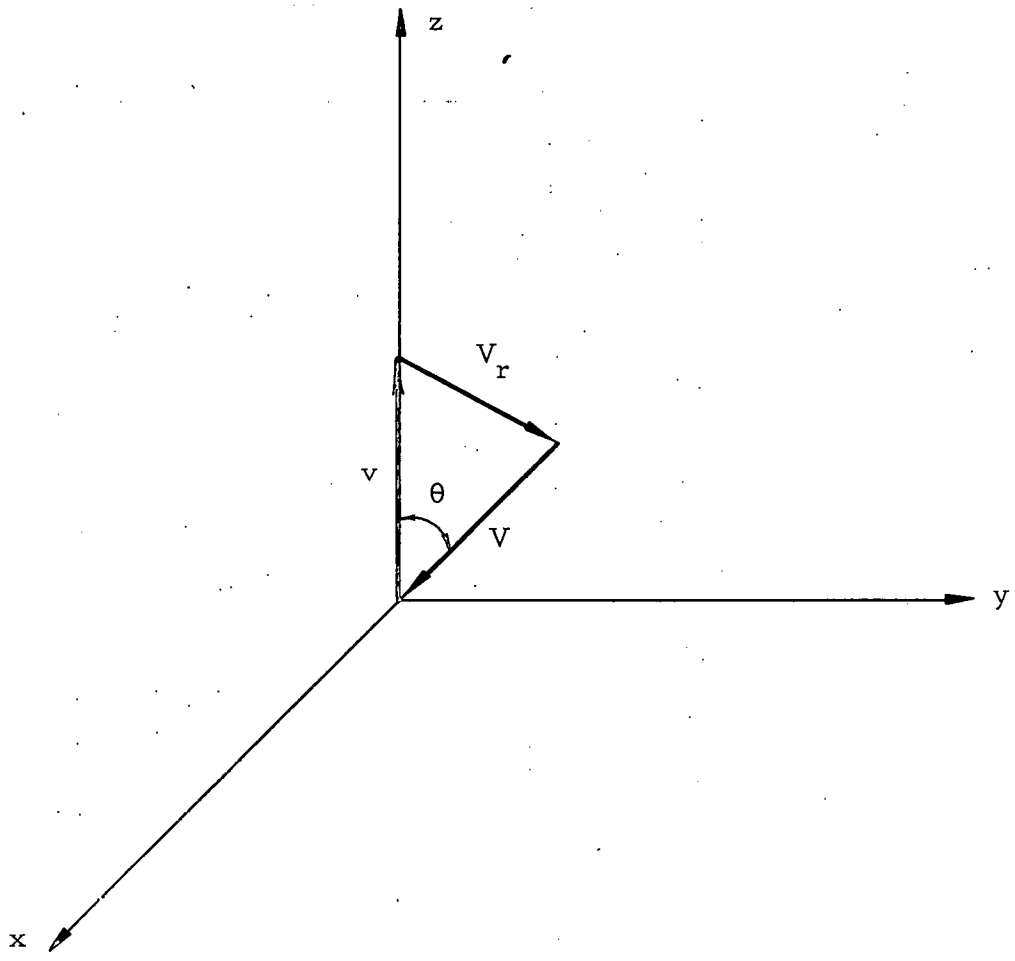

Figure A-3. Multigroup Structure in the Unresolved Region

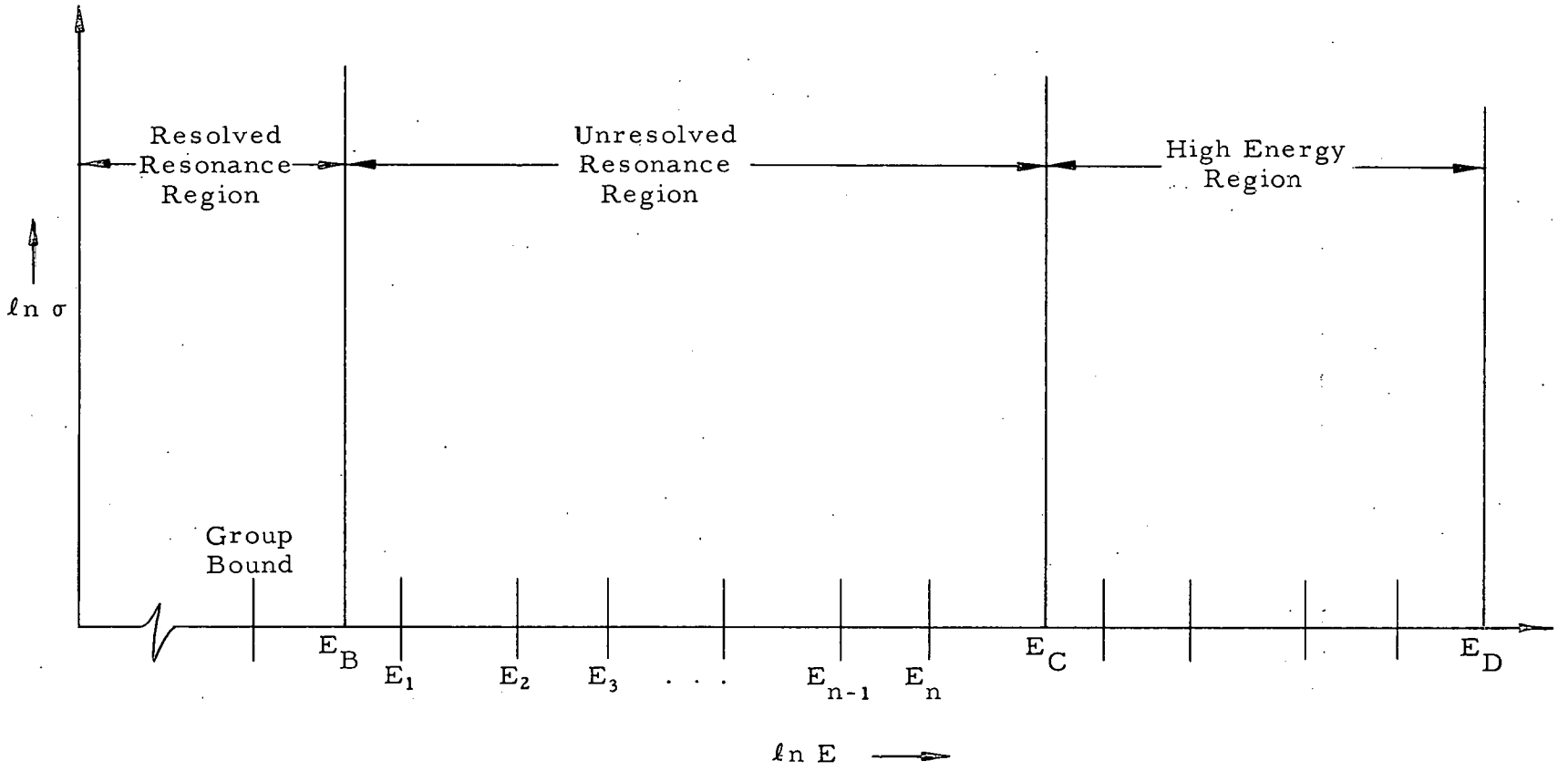

Figure A-4. Multigroup Structure in the High Energy Region

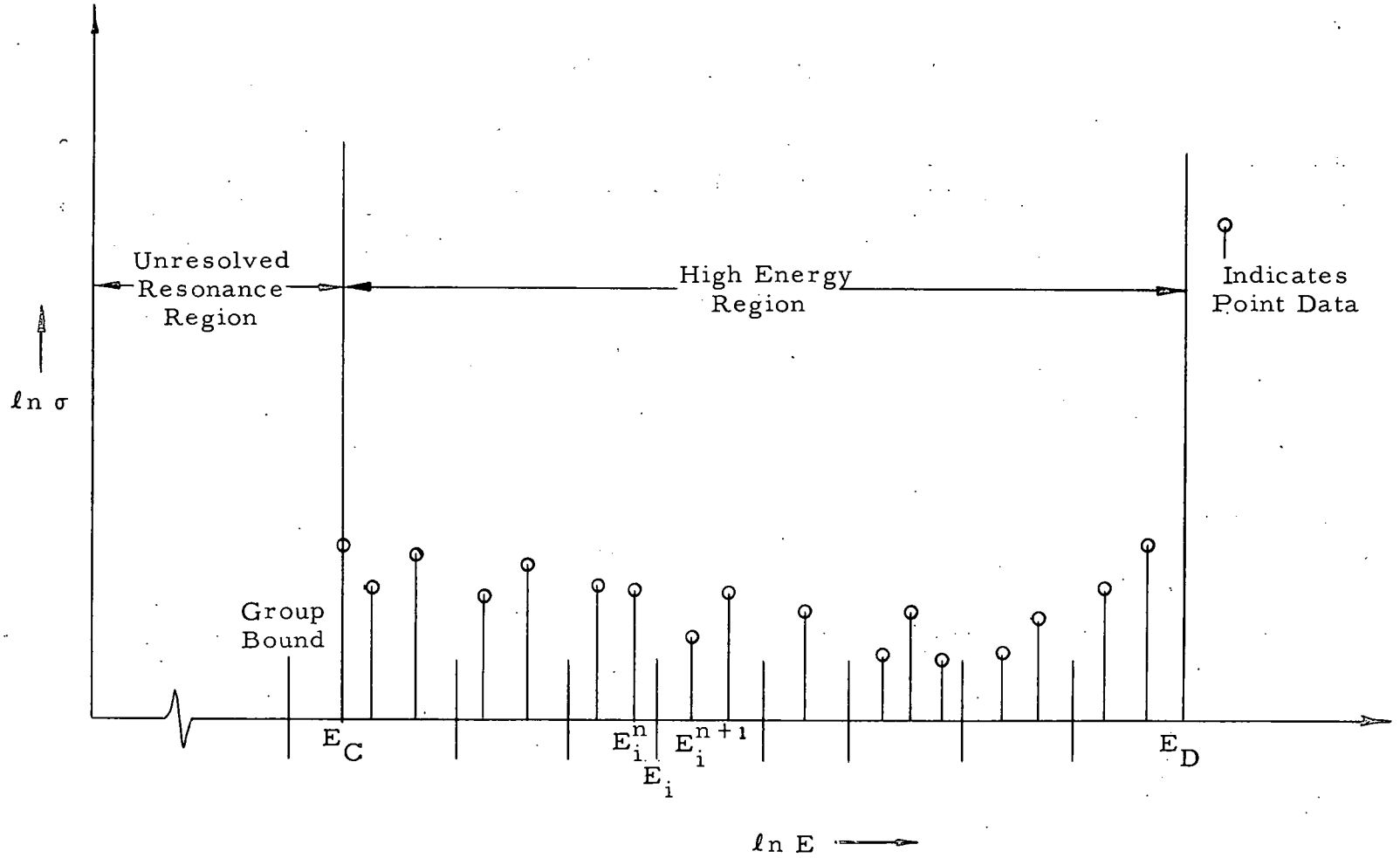

Figure A-5. Detail of Multigroup in High Energy Region

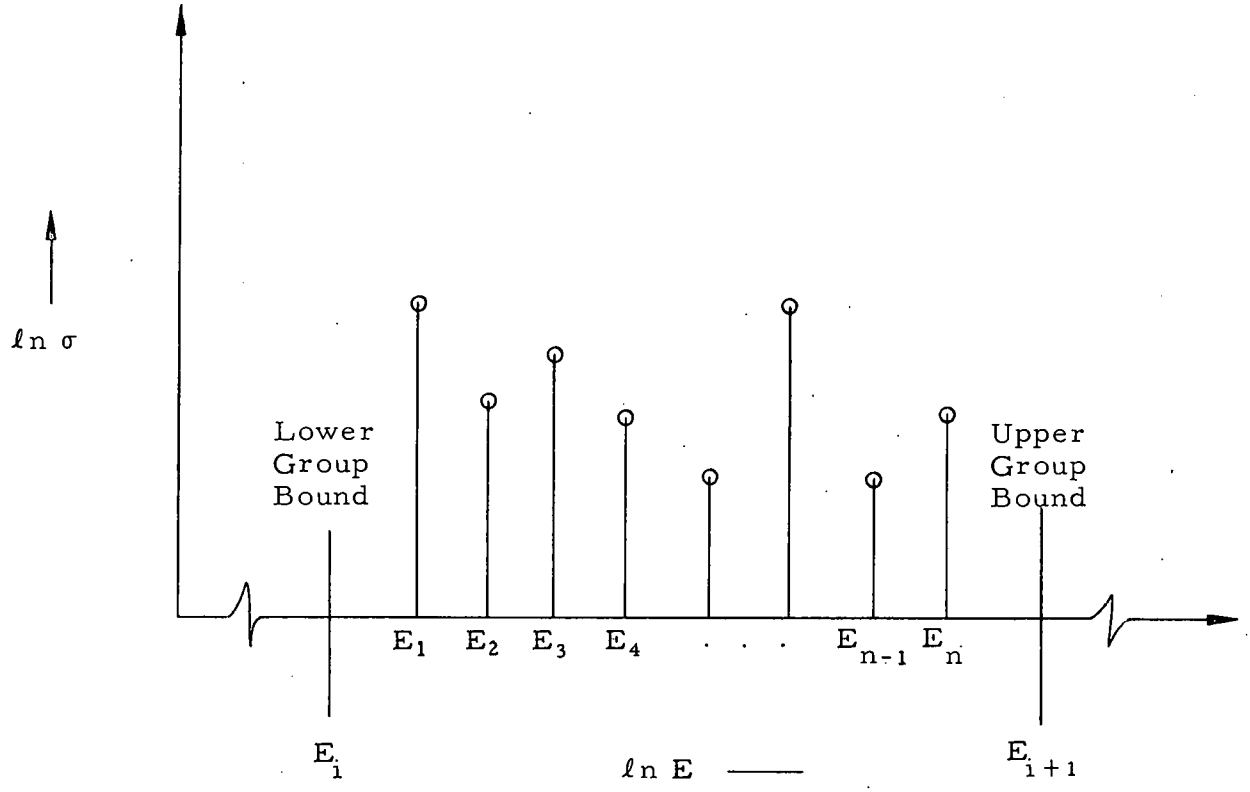

Figure A-6. Input Form

THE RIP PROGRAM
INPUT FORM NO. 1

DATE: _____

PREPARED BY: _____

Page ____ of ____ Pages

0 1 0 0 0 1

X-Sec. Av. ? 0
Res. Peak? 1
ψ-Set Calc. ? 2

PIMG L-Factors ?
Yes 0 / No 1
Homogeneous ? 1
Heterogeneous ? 2

U-238 ? 0
Th-232 ? 1
Other ? 2

Standard Bounds
Yes 0 / No 1

Absorption RI? 0
Fission RI? 1

Read 29 Data ? Yes 0 / No 1
Read 05 Data ? Yes 0 / No 1
Read 30 Data ? Yes 0 / No 1
Read 06 Data ? Yes 0 / No 1
Read 31 Data ? Yes 0 / No 1

Case Identification

0 2 0 0 0 1

Thermal Cutoff | Temperature (°K) | Total RI | Dancoff Factor | Eff. Chord Length

0 5 0 0 0 1

Absorber Mass, M | Potential Scattering X-Section, $\sigma_p^{(F)}$ | Statistical Spin Factor, g | Average Spacing, D

0 5 0 0 0 2

Average Gamma NO $\langle \Gamma_n^\circ \rangle$ | Average Gamma Sub F/A, $\langle \Gamma_{a/f} \rangle$ | Absorber X-Section at 0.0253 ev, $\sigma_{a/f}(E^*)$

0 6 0 0 0 1

High Energy Region Limit, E_d | Unresolved Region Limit, E_c | Resolved Region Limit, E_b | 1/v Region Limit, E_a

Notes: 1/v region limit = energy of first resolved peak.
High energy region limit = highest energy group bound.

APPENDIX B

Tables of the Doppler Broadening Function $J[\theta, K(\theta)]$

	θ				
K(θ)	0.0	0.005	0.01	0.015	0.02
0.0	0.1571E06*	0.9874E03	0.5210E03	0.5100E03	0.5040E03
1.0	0.7854E05	0.9296E03	0.4937E03	0.4370E03	0.4130E03
2.0	0.3927E05	0.8679E03	0.4648E03	0.3750E03	0.3370E03
3.0	0.1963E05	0.8014E03	0.4339E03	0.3400E03	0.2930E03
4.0	0.9817E04	0.7290E03	0.4007E03	0.2803E03	0.2386E03
4.5	0.6942E04	0.6900E03	0.3830E03	0.2691E03	0.2229E03
5.0	0.4909E04	0.6451E03	0.3645E03	0.2574E03	0.2086E03
5.5	0.3471E04	0.5770E03	0.3449E03	0.2451E03	0.1951E03
6.0	0.2454E04	0.5162E03	0.3225E03	0.2322E03	0.1821E03
6.5	0.1735E04	0.4590E03	0.2885E03	0.2186E03	0.1692E03
7.0	0.1227E04	0.4030E03	0.2581E03	0.1960E03	0.1563E03
7.5	0.8678E03	0.3477E03	0.2295E03	0.1754E03	0.1431E03
8.0	0.6136E03	0.2939E03	0.2015E03	0.1562E03	0.1296E03
8.5	0.4339E03	0.2425E03	0.1739E03	0.1375E03	0.1158E03
9.0	0.3068E03	0.1954E03	0.1470E03	0.1190E03	0.1018E03
9.5	0.2169E03	0.1539E03	0.1213E03	0.1010E03	0.8771E02
10.0	0.1534E03	0.1186E03	0.9771E02	0.8366E02	0.7399E02
10.5	0.1085E03	0.8964E02	0.7693E02	0.6769E02	0.6099E02
11.0	0.7670E02	0.6671E02	0.5928E02	0.5350E02	0.4909E02
11.5	0.5423E02	0.4901E02	0.4482E02	0.4137E02	0.3861E02
12.0	0.3835E02	0.3565E02	0.3336E02	0.3137E02	0.2973E02
12.5	0.2712E02	0.2574E02	0.2451E02	0.2341E02	0.2246E02
13.0	0.1917E02	0.1847E02	0.1783E02	0.1723E02	0.1671E02
13.5	0.1356E02	0.1320E02	0.1287E02	0.1255E02	0.1227E02
14.0	0.9587E01	0.9408E01	0.9236E01	0.9071E01	0.8922E01
14.5	0.6779E01	0.6689E01	0.6601E01	0.6517E01	0.6439E01
15.0	0.4794E01	0.4748E01	0.4704E01	0.4661E01	0.4620E01
15.5	0.3390E01	0.3367E01	0.3345E01	0.3322E01	0.3302E01
16.0	0.2397E01	0.2385E01	0.2374E01	0.2363E01	0.2352E01
16.5	0.1694E01	0.1689E01	0.1683E01	0.1678E01	0.1673E01
17.0	0.1198E01	0.1196E01	0.1193E01	0.1190E01	0.1187E01
17.5	0.8474E00	0.8460E00	0.8446E00	0.8431E00	0.8419E00
18.0	0.5992E00	0.5985E00	0.5978E00	0.5971E00	0.5964E00
18.5	0.4237E00	0.4233E00	0.4230E00	0.4226E00	0.4223E00
19.0	0.2996E00	0.2994E00	0.2992E00	0.2991E00	0.2989E00
19.5	0.2119E00	0.2118E00	0.2117E00	0.2116E00	0.2115E00
20.0	0.1498E00	0.1498E00	0.1497E00	0.1497E00	0.1496E00
21.0	0.7490E-01	0.7489E-01	0.7488E-01	0.7487E-01	0.7486E-01
22.0	0.3745E-01	0.3745E-01	0.3745E-01	0.3744E-01	0.3743E-01
23.0	0.1873E-01	0.1872E-01	0.1872E-01	0.1872E-01	0.1872E-01
24.0	0.9363E-02	0.9362E-02	0.9362E-02	0.9362E-02	0.9362E-02
25.0	0.4681E-02	0.4681E-02	0.4681E-02	0.4681E-02	0.4680E-02
26.0	0.2341E-02	0.2341E-02	0.2341E-02	0.2341E-02	0.2340E-02
27.0	0.1170E-02	0.1170E-02	0.1170E-02	0.1170E-02	0.1170E-02
28.0	0.5852E-03	0.5852E-03	0.5852E-03	0.5852E-03	0.5851E-03
29.0	0.2926E-03	0.2926E-03	0.2926E-03	0.2926E-03	0.2925E-03
30.0	0.1463E-03	0.1463E-03	0.1463E-03	0.1463E-03	0.1463E-03
31.0	0.7315E-04	0.7315E-04	0.7315E-04	0.7315E-04	0.7314E-04

*No sign following E implies a positive exponent

	θ				
K(θ)	0.03	0.04	0.05	0.10	0.15
0.0	0.5000E03	0.4990E03	0.4980E03	0.4979E03	0.4973E03
1.0	0.3850E03	0.3700E03	0.3610E03	0.3532E03	0.3522E03
2.0	0.2940E03	0.2750E03	0.2630E03	0.2514E03	0.2499E03
3.0	0.2380E03	0.2150E03	0.2010E03	0.1801E03	0.1782E03
4.0	0.1856E03	0.1613E03	0.1501E03	0.1307E03	0.1269E03
4.5	0.1704E03	0.1455E03	0.1335E03	0.1120E03	0.1077E03
5.0	0.1573E03	0.1324E03	0.1198E03	0.9667E02	0.9168E02
5.5	0.1459E03	0.1212E03	0.1083E03	0.8400E02	0.7836E02
6.0	0.1355E03	0.1116E03	0.9863E02	0.7355E02	0.6733E02
6.5	0.1257E03	0.1030E03	0.9022E02	0.6491E02	0.5819E02
7.0	0.1164E03	0.9508E02	0.8273E02	0.5772E02	0.5063E02
7.5	0.1073E03	0.8761E02	0.7588E02	0.5166E02	0.4436E02
8.0	0.9809E02	0.8036E02	0.6944E02	0.4647E02	0.3911E02
8.5	0.8881E02	0.7319E02	0.6323E02	0.4191E02	0.3468E02
9.0	0.7940E02	0.6600E02	0.5713E02	0.3781E02	0.3088E02
9.5	0.6988E02	0.5876E02	0.5107E02	0.3403E02	0.2754E02
10.0	0.6037E02	0.5150E02	0.4504E02	0.3045E02	0.2454E02
10.5	0.5107E02	0.4429E02	0.3907E02	0.2701E02	0.2179E02
11.0	0.4223E02	0.3730E02	0.3325E02	0.2367E02	0.1921E02
11.5	0.3411E02	0.3070E02	0.2770E02	0.2043E02	0.1676E02
12.0	0.2691E02	0.2468E02	0.2257E02	0.1731E02	0.1442E02
12.5	0.2078E02	0.1939E02	0.1797E02	0.1436E02	0.1219E02
13.0	0.1574E02	0.1491E02	0.1400E02	0.1165E02	0.1011E02
13.5	0.1174E02	0.1126E02	0.1070E02	0.9240E01	0.8199E01
14.0	0.8634E01	0.8370E01	0.8033E01	0.7173E01	0.6507E01
14.5	0.6286E01	0.6145E01	0.5946E01	0.5461E01	0.5056E01
15.0	0.4541E01	0.4467E01	0.4351E01	0.4088E01	0.3853E01
15.5	0.3261E01	0.3223E01	0.3155E01	0.3018E01	0.2887E01
16.0	0.2332E01	0.2312E01	0.2272E01	0.2204E01	0.2133E01
16.5	0.1662E01	0.1652E01	0.1628E01	0.1596E01	0.1558E01
17.0	0.1182E01	0.1177E01	0.1162E01	0.1148E01	0.1129E01
17.5	0.8393E00	0.8369E00	0.8276E00	0.8217E00	0.8122E00
18.0	0.5952E00	0.5940E00	0.5881E00	0.5862E00	0.5817E00
18.5	0.4217E00	0.4212E00	0.4173E00	0.4171E00	0.4150E00
19.0	0.2986E00	0.2984E00	0.2958E00	0.2963E00	0.2954E00
19.5	0.2114E00	0.2113E00	0.2095E00	0.2102E00	0.2098E00
20.0	0.1496E00	0.1495E00	0.1483E00	0.1490E00	0.1489E00
21.0	0.7482E-01	0.7480E-01	0.7478E-01	0.7468E-01	0.7460E-01
22.0	0.3742E-01	0.3741E-01	0.3740E-01	0.3739E-01	0.3737E-01
23.0	0.1872E-01	0.1871E-01	0.1871E-01	0.1871E-01	0.1870E-01
24.0	0.9361E-02	0.9360E-02	0.9359E-02	0.9358E-02	0.9357E-02
25.0	0.4680E-02	0.4680E-02	0.4680E-02	0.4680E-02	0.4680E-02
26.0	0.2340E-02	0.2340E-02	0.2340E-02	0.2340E-02	0.2340E-02
27.0	0.1170E-02	0.1170E-02	0.1170E-02	0.1170E-02	0.1170E-02
28.0	0.5851E-03	0.5851E-03	0.5851E-03	0.5851E-03	0.5851E-03
29.0	0.2925E-03	0.2925E-03	0.2925E-03	0.2925E-03	0.2926E-03
30.0	0.1463E-03	0.1463E-03	0.1463E-03	0.1463E-03	0.1463E-03
31.0	0.7314E-04	0.7314E-04	0.7314E-04	0.7314E-04	0.7314E-04

	θ					
K(θ)	0.20	0.25	0.30	0.35	0.40	0.45
0.0	0.4970E03	0.4969E03	0.4969E03	0.4968E03	0.4968E03	0.4968E03
1.0	0.3517E03	0.3515E03	0.3514E03	0.3513E03	0.3513E03	0.3513E03
2.0	0.2491E03	0.2488E03	0.2487E03	0.2486E03	0.2485E03	0.2485E03
3.0	0.1767E03	0.1762E03	0.1761E03	0.1760E03	0.1759E03	0.1758E03
4.0	0.1257E03	0.1251E03	0.1248E03	0.1246E03	0.1245E03	0.1245E03
4.5	0.1062E03	0.1055E03	0.1052E03	0.1050E03	0.1048E03	0.1048E03
5.0	0.8993E02	0.8914E02	0.8872E02	0.8847E02	0.8831E02	0.8820E02
5.5	0.7634E02	0.7541E02	0.7491E02	0.7462E02	0.7443E02	0.7430E02
6.0	0.6501E02	0.6393E02	0.6335E02	0.6301E02	0.6278E02	0.6263E02
6.5	0.5559E02	0.5436E02	0.5369E02	0.5328E02	0.5302E02	0.5284E02
7.0	0.4777E02	0.4638E02	0.4562E02	0.4515E02	0.4485E02	0.4464E02
7.5	0.4128E02	0.3975E02	0.3889E02	0.3836E02	0.3801E02	0.3777E02
8.0	0.3589E02	0.3423E02	0.3328E02	0.3269E02	0.3230E02	0.3203E02
8.5	0.3139E02	0.2964E02	0.2861E02	0.2796E02	0.2753E02	0.2722E02
9.0	0.2759E02	0.2579E02	0.2471E02	0.2401E02	0.2354E02	0.2321E02
9.5	0.2435E02	0.2255E02	0.2144E02	0.2071E02	0.2021E02	0.1985E02
10.0	0.2153E02	0.1977E02	0.1867E02	0.1792E02	0.1741E02	0.1703E02
10.5	0.1903E02	0.1737E02	0.1629E02	0.1556E02	0.1504E02	0.1466E02
11.0	0.1676E02	0.1523E02	0.1423E02	0.1352E02	0.1301E02	0.1264E02
11.5	0.1466E02	0.1331E02	0.1239E02	0.1174E02	0.1126E02	0.1090E02
12.0	0.1268E02	0.1154E02	0.1074E02	0.1015E02	0.9718E01	0.9382E01
12.5	0.1083E02	0.9888E01	0.9217E01	0.8718E01	0.8337E01	0.8039E01
13.0	0.9082E01	0.8352E01	0.7815E01	0.7406E01	0.7087E01	0.6834E01
13.5	0.7470E01	0.6930E01	0.6521E01	0.6202E01	0.5948E01	0.5743E01
14.0	0.6015E01	0.5637E01	0.5342E01	0.5106E01	0.4914E01	0.4756E01
14.5	0.4740E01	0.4489E01	0.4287E01	0.4122E01	0.3985E01	0.3870E01
15.0	0.3659E01	0.3501E01	0.3371E01	0.3261E01	0.3169E01	0.3090E01
15.5	0.2773E01	0.2678E01	0.2598E01	0.2529E01	0.2470E01	0.2418E01
16.0	0.2068E01	0.2013E01	0.1966E01	0.1925E01	0.1889E01	0.1857E01
16.5	0.1522E01	0.1492E01	0.1465E01	0.1441E01	0.1420E01	0.1402E01
17.0	0.1109E01	0.1092E01	0.1078E01	0.1065E01	0.1053E01	0.1042E01
17.5	0.8017E00	0.7927E00	0.7849E00	0.7778E00	0.7713E00	0.7655E00
18.0	0.5760E00	0.5712E00	0.5671E00	0.5633E00	0.5599E00	0.5567E00
18.5	0.4120E00	0.4095E00	0.4073E00	0.4054E00	0.4036E00	0.4019E00
19.0	0.2937E00	0.2924E00	0.2913E00	0.2903E00	0.2894E00	0.2885E00
19.5	0.2089E00	0.2082E00	0.2077E00	0.2071E00	0.2067E00	0.2062E00
20.0	0.1483E00	0.1480E00	0.1477E00	0.1474E00	0.1472E00	0.1470E00
21.0	0.7452E-01	0.7444E-01	0.7437E-01	0.7430E-01	0.7424E-01	0.7419E-01
22.0	0.3735E-01	0.3734E-01	0.3732E-01	0.3730E-01	0.3728E-01	0.3727E-01
23.0	0.1870E-01	0.1870E-01	0.1869E-01	0.1869E-01	0.1868E-01	0.1868E-01
24.0	0.9356E-02	0.9356E-02	0.9355E-02	0.9354E-02	0.9352E-02	0.9352E-02
25.0	0.4679E-02	0.4679E-02	0.4679E-02	0.4679E-02	0.4679E-02	0.4679E-02
26.0	0.2340E-02	0.2340E-02	0.2340E-02	0.2340E-02	0.2340E-02	0.2340E-02
27.0	0.1170E-02	0.1170E-02	0.1170E-02	0.1770E-02	0.1170E-02	0.1170E-02
28.0	0.5851E-03	0.5851E-03	0.5851E-03	0.5851E-03	0.5851E-03	0.5851E-03
29.0	0.2926E-03	0.2926E-03	0.2926E-03	0.2926E-03	0.2926E-03	0.2926E-03
30.0	0.1463E-03	0.1463E-03	0.1463E-03	0.1463E-03	0.1463E-03	0.1463E-03
31.0	0.7314E-04	0.7315E-04	0.7315E-04	0.7315E-04	0.7315E-04	0.7315E-04

	θ					
K(θ)	0.50	0.60	0.70	0.80	0.90	1.00
0.0	0.4968E03	0.4968E03	0.4967E03	0.4967E03	0.4967E03	0.4967E03
1.0	0.3513E03	0.3513E03	0.3513E03	0.3513E03	0.3513E03	0.3513E03
2.0	0.2485E03	0.2484E03	0.2484E03	0.2484E03	0.2484E03	0.2484E03
3.0	0.1758E03	0.1757E03	0.1757E03	0.1757E03	0.1757E03	0.1757E03
4.0	0.1244E03	0.1243E03	0.1243E03	0.1243E03	0.1242E03	0.1242E03
4.5	0.1047E03	0.1046E03	0.1046E03	0.1045E03	0.1045E03	0.1045E03
5.0	0.8812E02	0.8802E02	0.8796E02	0.8792E02	0.8790E02	0.8788E02
5.5	0.7421E02	0.7410E02	0.7403E02	0.7398E02	0.7395E02	0.7392E02
6.0	0.6252E02	0.6238E02	0.6230E02	0.6225E02	0.6221E02	0.6218E02
6.5	0.5272E02	0.5257E02	0.5247E02	0.5241E02	0.5236E02	0.5232E02
7.0	0.4450E02	0.4430E02	0.4419E02	0.4412E02	0.4407E02	0.4403E02
7.5	0.3760E02	0.3740E02	0.3727E02	0.3718E02	0.3712E02	0.3707E02
8.0	0.3183E02	0.3158E02	0.3143E02	0.3133E02	0.3126E02	0.3121E02
8.5	0.2701E02	0.2675E02	0.2656E02	0.2644E02	0.2636E02	0.2630E02
9.0	0.2297E02	0.2265E02	0.2245E02	0.2232E02	0.2223E02	0.2217E02
9.5	0.1959E02	0.1926E02	0.1904E02	0.1889E02	0.1878E02	0.1871E02
10.0	0.1675E02	0.1638E02	0.1614E02	0.1598E02	0.1587E02	0.1579E02
10.5	0.1437E02	0.1399E02	0.1373E02	0.1356E02	0.1344E02	0.1335E02
11.0	0.1235E02	0.1194E02	0.1168E02	0.1151E02	0.1138E02	0.1129E02
11.5	0.1062E02	0.1021E02	0.9955E01	0.9777E01	0.9645E01	0.9549E01
12.0	0.9119E01	0.8739E01	0.8484E01	0.8304E01	0.8174E01	0.8077E01
12.5	0.7802E01	0.7433E01	0.7198E01	0.7029E01	0.6905E01	0.6811E01
13.0	0.6629E01	0.6322E01	0.6107E01	0.5950E01	0.5833E01	0.5744E01
13.5	0.5574E01	0.5286E01	0.5105E01	0.4972E01	0.4870E01	0.4792E01
14.0	0.4624E01	0.4419E01	0.4268E01	0.4154E01	0.4066E01	0.3997E01
14.5	0.3773E01	0.3587E01	0.3473E01	0.3385E01	0.3317E01	0.3262E01
15.0	0.3022E01	0.2911E01	0.2826E01	0.2759E01	0.2706E01	0.2663E01
15.5	0.2373E01	0.2277E01	0.2219E01	0.2173E01	0.2137E01	0.2106E01
16.0	0.1829E01	0.1781E01	0.1743E01	0.1712E01	0.1687E01	0.1666E01
16.5	0.1385E01	0.1345E01	0.1322E01	0.1302E01	0.1286E01	0.1273E01
17.0	0.1033E01	0.1016E01	0.1002E01	0.9904E00	0.9805E00	0.9722E00
17.5	0.7601E00	0.7467E00	0.7386E00	0.7318E00	0.7260E00	0.7211E00
18.0	0.5539E00	0.5488E00	0.5445E00	0.5408E00	0.5376E00	0.5348E00
18.5	0.4004E00	0.3964E00	0.3940E00	0.3919E00	0.3901E00	0.3886E00
19.0	0.2877E00	0.2863E00	0.2851E00	0.2840E00	0.2831E00	0.2823E00
19.5	0.2058E00	0.2047E00	0.2041E00	0.2035E00	0.2030E00	0.2025E00
20.0	0.1468E00	0.1464E00	0.1461E00	0.1458E00	0.1455E00	0.1453E00
21.0	0.7413E-01	0.7403E-01	0.7395E-01	0.7388E-01	0.7381E-01	0.7375E-01
22.0	0.3726E-01	0.3723E-01	0.3721E-01	0.3719E-01	0.3718E-01	0.3716E-01
23.0	0.1867E-01	0.1867E-01	0.1867E-01	0.1866E-01	0.1866E-01	0.1865E-01
24.0	0.9350E-02	0.9349E-02	0.9348E-02	0.9346E-02	0.9345E-02	0.9344E-02
25.0	0.4678E-02	0.4678E-02	0.4678E-02	0.4677E-02	0.4677E-02	0.4677E-02
26.0	0.2340E-02	0.2340E-02	0.2340E-02	0.2340E-02	0.2340E-02	0.2340E-02
27.0	0.1170E-02	0.1170E-02	0.1170E-02	0.1170E-02	0.1170E-02	0.1170E-02
28.0	0.5851E-03	0.5851E-03	0.5851E-03	0.5851E-03	0.5851E-03	0.5851E-03
29.0	0.2926E-03	0.2926E-03	0.2926E-03	0.2926E-03	0.2926E-03	0.2926E-03
30.0	0.1463E-03	0.1463E-03	0.1463E-03	0.1463E-03	0.1463E-03	0.1463E-03
31.0	0.7315E-04	0.7315E-04	0.7314E-04	0.7314E-04	0.7314E-04	0.7314E-04

REFERENCES

[1] Wehmeyer, D. B., et al, SSCR Basic Physics Program - Theoretical Analysis - Part I, The Babcock & Wilcox Company, BAW-1230(I), Lynchburg, Virginia, March, 1962.

[2] de Coulon, G. A. G., et al, SSCR Basic Physics Program - Theoretical Analysis - Part II, The Babcock & Wilcox Company, BAW-1230(II), Lynchburg, Virginia, March, 1962.

[3] Engelder, T. C., et al, SSCR Basic Physics Program - Critical Experiments on Lattices Moderated by D_2O-H_2O Mixtures, The Babcock & Wilcox Company, BAW-1231, Lynchburg, Virginia, December, 1961.

[4] Barrett, L. G. and Mortenson, J. H., SSCR Basic Physics Program - Exponential Experiments on Lattices Moderated by D_2O-H_2O Mixtures, The Babcock & Wilcox Company, BAW-1232, Lynchburg, Virginia, January, 1962.

[5] Barrett, L. G., Worsham, H. J., and Engelder, T. C., SSCR Basic Physics Program - Exponential Experiments at Elevated Temperatures on Lattices Moderated by D_2O-H_2O Mixtures, The Babcock & Wilcox Company, BAW-1233, Lynchburg, Virginia, March, 1962.

[6] Roberts, D. M. and Pettus, W. G., SSCR Basic Physics Program - Age Measurements in ThO_2-D_2O-H_2O Lattices, The Babcock & Wilcox Company, BAW-1234, Lynchburg, Virginia, September, 1961.

[7] Engelder, T. C., et al, SSCR Basic Physics Program - Measurement and Analysis of Perturbed Lattices of Slightly Enriched UO_2 Moderated by D_2O-H_2O Mixtures, The Babcock & Wilcox Company, BAW-1274, Lynchburg, Virginia, October, 1963.

[8] SSCR Basic Physics Program - Quarterly Technical Report No. 1, The Babcock & Wilcox Company, BAW-1213, Lynchburg, Virginia, October, 1960.

[9] SSCR Basic Physics Program - Quarterly Technical Report No. 2, The Babcock & Wilcox Company, BAW-1218, Lynchburg, Virginia, January, 1961.

[10] SSCR Basic Physics Program - Quarterly Technical Report No. 3, The Babcock & Wilcox Company, BAW-1220, Lynchburg, Virginia, July, 1961.

[11] SSCR Basic Physics Program - Quarterly Technical Report No. 4, The Babcock & Wilcox Company, BAW-1221, Lynchburg, Virginia, October, 1961.

[12] SSCR Basic Physics Program - Quarterly Technical Report No. 5, The Babcock & Wilcox Company, BAW-1240, Lynchburg, Virginia, January, 1962.

[13] SSCR Basic Physics Program - Quarterly Technical Report No. 6, The Babcock & Wilcox Company, BAW-1250, Lynchburg, Virginia, August, 1962.

[14] SSCR Basic Physics Program - Quarterly Technical Report No. 7, The Babcock & Wilcox Company, BAW-1259, Lynchburg, Virginia, September, 1962.

[15] SSCR Basic Physics Program - Quarterly Technical Report No. 8, The Babcock & Wilcox Company, BAW-1262, Lynchburg, Virginia, December, 1962.

[16] SSCR Basic Physics Program - Quarterly Technical Report No. 9, The Babcock & Wilcox Company, BAW-1266, Lynchburg, Virginia, May, 1963.

[17] SSCR Basic Physics Program - Quarterly Technical Report No. 10, The Babcock & Wilcox Company, BAW-1271, Lynchburg, Virginia, June, 1963.

[18] Clark, R. H. and Engelder, T. C., SSCR Basic Physics Program - Critical Experiment Hazard Evaluation, The Babcock & Wilcox Company, BAW-1211 (and Supplement No. 1), Lynchburg, Virginia, September, 1960.

[19] Engelder, T. C., Application for Amendment No. 5 to License No. CX-10 to Use 2-1/2%-Enriched UO_2 Fuel, The Babcock & Wilcox Company, BAW-1245 (and Supplement No. 1), Lynchburg, Virginia, March, 1962.

[20] Snidow, N. L., et al, Thorium Uranium Physics Experiments - Final Report, The Babcock & Wilcox Company, BAW-1191, Lynchburg, Virginia, May, 1960.

[21] Davison, P. W., et al, Microscopic Lattice Parameters in Single and Multi-Region Cores, WCAP-1434, June, 1961.

[22] Lewis, R. H., et al, Thermal Activation Method for ρ_{28} Measurements in Slightly Enriched UO_2 Lattices, The Babcock & Wilcox Company, BAW-1268, Lynchburg, Virginia, May, 1963.

[23] Bohl, H., et al, P1MG - A One Dimensional Multigroup P_1 Code for the IBM-704, WAPD-TM-135, July, 1959.

[24] Bell, G. I., "A Simple Treatment for Effective Resonance Absorption Cross Sections in Dense Lattices", Nucl Sci & Engr 5, pp 138-39 (1959).

[25] Hellstrand, E. and Lundgren, G., "The Resonance Integral for Uranium Metal and Oxide", Nucl Sci & Engr 12, No. 3 (March, 1962).

[26] Sauer, A., "Blackness in Cylindrical Fuel Lattices", Trans Am Nucl Soc 6, No. 1 (June, 1963).

[27] Meghreblian, R. V. and Holmes, D. K., Reactor Analysis, McGraw-Hill Book Co., Inc., New York, 1960, p 664.

[28] Weinberg, A. M. and Wigner, E. P., The Physical Theory of Neutron Chain Reactors, University of Chicago Press, 1958, p 290.

[29] Rothenstein, Wolfgang, "Collision Probabilities and Resonance Integrals for Lattices", NSE 1, pp 162-171 (1960).

[30] Blatt, J. M. and Weisskoff, V. F., Theoretical Nuclear Physics, John Wiley & Sons, New York, 1952, pp 391-394.

[31] Nordheim, L. W. and Adler, F. T., Tables for the Computation of Resonance Integrals, GA-277, 1958.

[32] Kuncir, G. F., A Program for the Calculation of Resonance Integrals, GA-2525, August, 1961, pp 57-59.

[33] Porter, C. E. and Thomas, R. G., "Fluctuations of Neutron Reaction Widths", Phys Rev 104, pp 483-491 (1956).

[34] Levine, M. M., et al, "The Slowing Down of Neutrons by Deuterium", Nuclear Science and Engineering 7, p 14 (1960).

[35] Roy, D. H. and Murray, R. L., "Introduction to Slowing Down Approximations in Neutron Transport Theory", North Carolina State College, Research Bulletin No. 2 (June 1962).

DISTRIBUTION

1. TID-4500, UC-80, 23rd Edition (619)

2. United States Atomic Energy Commission, New York Operations Office (5)

   Behmer, RE (3)
   Catalano, JJ
   Potter, HS

3. United States Atomic Energy Commission, Washington 25, D. C. (5)

   Hall, EE (2)
   Voigt, WR (3)

4. Brookhaven National Laboratory (2)

   Hellens, R
   Kouts, HJC

5. Norwegian Atomic Energy Commission

6. The Babcock & Wilcox Company (59)

   Ball, RM
   Barberton Library
   Barringer, HS
   Breazeale, WM
   CEL File (10)
   Central Files (10)
   Clark, RH
   Deuster, RW (3)
   Edlund, MC
   Engelder, TC (5)
   Fairburn, GT
   Gumprich, WC/Mumm, JF
   Hallam, JW
   Happell, JJ
   Harrison, RH/Moore, WT
   Hostetler, DR
   Landis, JW
   Lewis, RH
   Library, AED (2)
   Littrell, LW (2)
   Markert, W/Alliance Library
   Pettus, WG
   Plunkett, DA
   Roberts, DM
   Roy, DH
   Schomer, RT
   Schuler, TM, Jr.
   Snidow, NL
   Travis, CC/TRG
   Webb, RA/Project File
   Wehmeyer, DB
   Williams, DVP
   Woodhall, CB